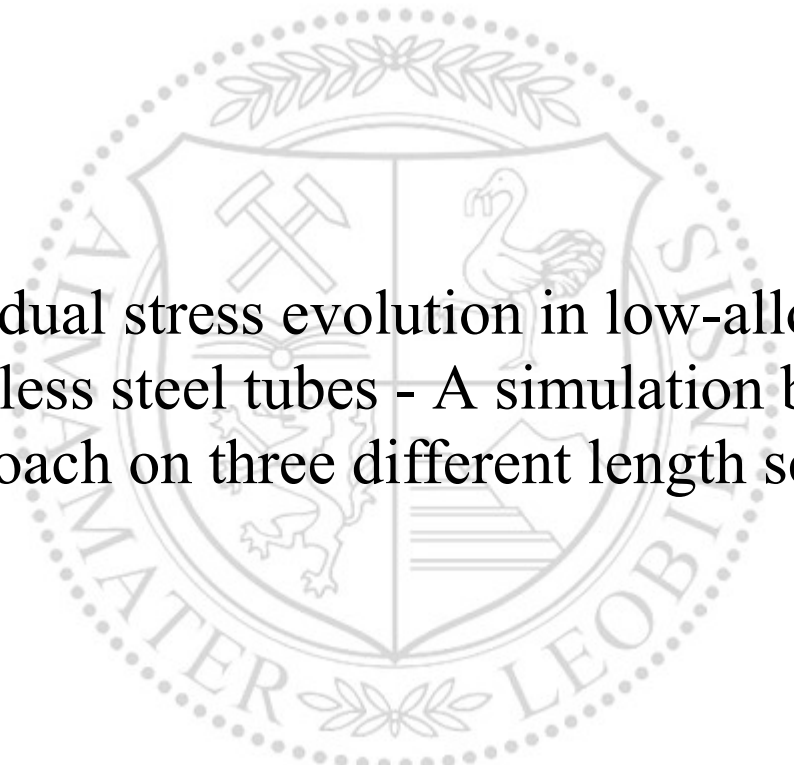




Chair of Mechanics

Doctoral Thesis



Residual stress evolution in low-alloyed  
seamless steel tubes - A simulation based  
approach on three different length scales

Dipl.-Ing. Silvia Leitner, BSc

April 2020

## EIDESSTATTLICHE ERKLÄRUNG

Ich erkläre an Eides statt, dass ich diese Arbeit selbständig verfasst, andere als die angegebenen Quellen und Hilfsmittel nicht benutzt, und mich auch sonst keiner unerlaubten Hilfsmittel bedient habe.

Ich erkläre, dass ich die Richtlinien des Senats der Montanuniversität Leoben zu "Gute wissenschaftliche Praxis" gelesen, verstanden und befolgt habe.

Weiters erkläre ich, dass die elektronische und gedruckte Version der eingereichten wissenschaftlichen Abschlussarbeit formal und inhaltlich identisch sind.

Datum 02.04.2020



---

Unterschrift Verfasser/in  
Silvia, Leitner

# Acknowledgements

The research presented in this thesis was conducted at the Materials Center Leoben Forschung GmbH and the Institut of Mechanics at the Montanuniversitaet Leoben in partnership with voestalpine Tubulars GmbH in the COMET research project A 2.32-03.

I gratefully acknowledge the financial support under the scope of the COMET program within the K2 Center "Integrated Computational Material, Process and Product Engineering (IC-MPPE)" (Project No 859480). This program is supported by the Austrian Federal Ministries for Climate Action, Environment, Energy, Mobility, Innovation and Technology (BMK) and for Digital and Economic Affairs (BMDW), represented by the Austrian research funding association (FFG), and the federal states of Styria, Upper Austria and Tyrol.

My particular thanks goes to Dr. Jürgen Klarner and Dr. Gerald Winter from voestalpine Tubulars GmbH for their very constructive support, their positive and quick feedback and the good communication and exchange of ideas in the last three years.

Prof. Thomas Antretter has supported me during this time with his valuable scientific advice and his positive attitude during our discussions, for which I want to express my sincere thanks.

I also want thank Dr. Werner Ecker for his straightforward and very constructive supervision and mentoring. In particular for his support in acquiring new competences and the freedom to conduct this research at my own pace and developing and pursuing my own ideas under his guidance.

Finally, I want to express my deepest gratitude to my friends and my family for their invaluable support and their endurance- especially to my husband, René, for your love and for believing in me.

# Summary

Residual stresses in a component can alter its mechanical performance and environmental resistance against corrosion or hydrogen embrittlement. To continuously reduce component weight and still increase the mechanical performance by the use of steels with higher yield strengths in corrosive environments, the residual stress formation during manufacturing must be monitored and understood. Due to steel's complex microstructure, residual stresses form on different characteristic length scales and not only macroscopic scale. Residual stresses can also form on smaller length scales and require thus a multi-scale investigation.

The residual stress formation in low-alloyed, seamless, sour gas resistant steel tubes on different length scales was investigated using a model based simulation approach. Starting from the macroscopic scale a model for calculating the temperature, phase and residual stress evolution as a function of radial position within the tube during cooling was created. The heat treatment model was validated with thermal measurements, the phase evolution model was verified with microhardness measurements over the tube's cross section and the residual stress evolution using high-energy x-ray diffraction measurements. In this thus validated macroscopic model, the cooling boundary conditions were varied in order to find potential low-residual stress cooling strategies for mostly martensite or mostly bainite microstructures.

The experimentally validated continuum model was employed to calculate the effects of local chemical enrichment and depletion in segregation lines on residual stresses, i.e. the mesoscopic stresses. The martensite transformation start temperature is delayed due to chemical enrichment of C, Mo and Cr and the concomitant changes in thermal expansion, volume expansion and elastic properties were derived from calculations and literature. The mesoscopic residual stresses are calculated by means of a submodel and as a function of composition.

On the microscopic scale the residual stresses around precipitates are investigated. This is owing to the recent trend of using precipitates as hydrogen traps and that some have been already proven to be beneficial in some cases. Thus a relative comparison of occurring precipitates



and inclusions was sought, for low alloyed steels. This was done using an analytic, thermo-elastic comparison of average matrix stress and average inclusion stress based on literature data. The inclusions are ranked by their residual stress formation potential.

For a single inclusion the crystallographic relations, interface properties and creep dissipation are considered to calculate the energetically favored shape and orientation of  $\text{Mo}_2\text{C}$  in bcc Fe. The anisotropic interface energies, calculated with first principle methods, suggest that the experimentally observed elongated shape of  $\text{Mo}_2\text{C}$  in bcc Fe is caused by interface energy minimization. The mechanical strain energy contribution for lattice formation was considered and is for realistic inclusion volumes smaller than the interface contribution. When matrix creep effects are neglected for simplified considerations, the elastic contribution would overweight the interface contribution.

With these developed methods, residual stress in a low- and micro-alloyed sour gas resistant steel tubes are calculated and their evolution is resolved on three different length scales. The macroscopic model allows a detailed understanding of how the cooling process and residual stress formation interact. Based on the developed models, low-residual stress cooling strategies are provided. It is beneficial to reduce surface temperature gradients as far as possible and use spray water cooling on both the inner and the outer surface. To account the steel's complex microstructure, the residual stresses caused by interdendritic segregation and precipitate formation are discussed. Stresses caused by the chemical inhomogeneities resulting from segregation, act over a wider characteristic length scale and are comparatively low compared to stresses due to thermal misfits of precipitates. Common precipitates in steel are ranked by their residual stress formation potential.

## Zusammenfassung

Die Eigenspannungsentwicklung in niedrig legierten, nahtlos gewalzten und Sauer gas beständigen Rohren wird auf verschiedenen Längenskalen mit Simulationsmethoden untersucht. Beginnend mit der makroskopischen Ebene wird ein Modell entwickelt, um die Temperatur, Phasen und Eigenspannungsgeschichte an verschiedenen, radialen Positionen während dem Kühlen eines Rohres zu berechnen. Das Modell zur Temperaturentwicklung wird mit Temperaturmessungen an der Anlage validiert, das Phasenevolutionsmodell kann mit Mikrohärtmessungen über den Rohrquerschnitt korreliert werden und die berechneten Eigenspannungen werden mit Eigenspannungsmessungen mittels Röntgenbeugungsmethoden verglichen.

Mit diesem experimentell validierten, makroskopischen Modell werden durch Variation der Kühlbedingungen Vorschläge zur Reduktion von Eigenspannungen für überwiegend martensitische oder überwiegend bainitische Gefügezusammensetzung im Rohr abgeleitet.

Das makroskopische Kontinuummodell wird weiter verwendet, um die Effekte lokaler Seigerung auf Eigenspannungen zu untersuchen. Seigerung von C, Mo und Cr verzögert die Umwandlung von Austenit zu Martensit und verändert die thermische Ausdehnung, den Volumssprung und elastische Eigenschaften der Tochterphasen.

Auf mikroskopischer Ebene werden Eigenspannungen um Inklusionen untersucht, im Hinblick auf den Trend, dass Inklusionen gezielt als Fallen für Wasserstoff in Stählen genutzt werden können. Ein relativer Vergleich von Inklusionen, die in niedrig- und mikrolegierten Stählen vorkommen, basierend auf deren thermo-elastischen Potential zur Eigenspannungsbildung wird präsentiert. Die vereinfachte thermo-elastische Eigenspannungsbetrachtung kann für eine genauere Untersuchung um Informationen über die Kristallographie und Kriechmechanismen bei erhöhten Bildungstemperaturen ergänzt werden.

Für eine einzelne  $\text{Mo}_2\text{C}$  Inklusion in Eisen werden die kristallographischen Beziehungen berücksichtigt um mit atomistischen Methoden die Grenzflächenenergien verschiedener  $\text{Mo}_2\text{C}/\text{Fe}$  Orientierungen zu berechnen. Diese Interfaceenergien zeigen, dass die experimentell beobachtete, nadelige Form der Carbide zu einer Energieminimierung führt. Wenn man den mechanischen Beitrag der Deformationsenergie mit Kriechen in der Matrix mitberücksichtigt, überwiegt dennoch der Interfacebeitrag. Bei einer vereinfachten, elastische Betrachtung der Deformationsenergie wird der mechanische Beitrag zur Gesamtenergie jedoch deutlich überschätzt.

Mit den entwickelten Methoden kann die Eigenspannungsentwick-

lung in niedrig und mikrolegierten, sauergasbeständigen Stahlrohren berechnet und auf drei Längenskalen erklärt werden. Mithilfe des makroskopischen Modells kann die Wechselwirkung zwischen den Kühlbedingungen und der Eigenspannungsentwicklung verstanden werden und daraus Strategien für Kühlbedingungen mit geringer Eigenspannungsentwicklung abgeleitet werden. Dazu ist es von Vorteil, die Temperaturgradienten an den gekühlten Oberflächen gering zu halten und wenn möglich auf beiden freien Oberflächen zu kühlen. Um die komplexe Mikrostruktur in Stahl zu berücksichtigen, wird die Spannungsentwicklung um Seigerungszone und Ausscheidungen untersucht. Dabei zeigt sich, dass Spannungen zufolge der chemischen Inhomogenität an Seigerungen zwar über größere Distanzen wirken, aber von geringerer Höhe sind als Spannungen um Ausscheidungen.

# Contents

<b>1</b>	<b>Introduction</b>	<b>1</b>
1.1	Motivation . . . . .	1
1.2	Residual stresses . . . . .	2
1.3	Manufacturing process . . . . .	5
1.4	Material . . . . .	7
1.4.1	Alloying concept . . . . .	7
1.4.2	Martensite and bainite . . . . .	8
1.4.3	Interaction with hydrogen . . . . .	9
1.5	State of the art . . . . .	12
1.6	Modeling . . . . .	13
1.6.1	Model types . . . . .	13
1.6.2	Phase transformation model . . . . .	15
1.7	Main findings . . . . .	20
<b>2</b>	<b>Publication 1</b>	
	<i>Residual stress and microstructure evolution in steel tubes for different cooling conditions</i>	
	<i>- Simulation and verification</i>	<b>30</b>
2.1	Abstract . . . . .	32
2.2	Introduction . . . . .	32
2.3	Methods . . . . .	33
2.3.1	Process description . . . . .	33
2.3.2	Model description . . . . .	33
2.4	Measurements . . . . .	38
2.5	Results . . . . .	38
2.6	Conclusions . . . . .	44
<b>3</b>	<b>Publication 2</b>	
	<i>Model-based residual stress design in multiphase seamless steel tubes</i>	<b>50</b>
3.1	Abstract . . . . .	52
3.2	Introduction . . . . .	52
3.3	Materials and methods . . . . .	54

3.3.1	Model description . . . . .	54
3.4	Results . . . . .	59
3.4.1	Strategy 1 . . . . .	59
3.4.2	Strategy 2 . . . . .	61
3.4.3	Strategy 3 . . . . .	63
3.5	Discussion and conclusion . . . . .	67
<b>4</b>	<b>Publication 3</b>	
	<i>Residual stress evolution in low-alloyed steels on three different length scales</i>	<b>73</b>
4.1	Abstract . . . . .	75
4.2	Introduction . . . . .	75
4.3	Methods and Modeling . . . . .	77
4.3.1	Phase transformation model . . . . .	80
4.3.2	Macroscopic model . . . . .	80
4.3.3	Mesosopic model . . . . .	81
4.3.4	Microscopic model . . . . .	84
4.4	Results . . . . .	86
4.5	Summary and conclusions . . . . .	90
<b>5</b>	<b>Publication 4</b>	
	<i>Numerical analysis of shape, orientation and interface properties of Mo<sub>2</sub>C precipitates in iron</i>	<b>97</b>
5.1	Abstract . . . . .	99
5.2	Introduction . . . . .	100
5.3	Computational Details and Methodology . . . . .	101
5.3.1	DFT simulations . . . . .	102
5.3.2	Energy contributions . . . . .	105
5.4	Results . . . . .	107
5.4.1	Thermo-elastic properties of bulk Fe and Mo <sub>2</sub> C . . . . .	107
5.4.2	Mo <sub>2</sub> C-Fe Interface . . . . .	109
5.4.3	Balance of interface and strain energy . . . . .	117
5.5	Conclusions . . . . .	121
5.6	Appendix . . . . .	122

# Chapter 1

## Introduction

### 1.1 Motivation

Residual stress formation can be a crucial point during manufacturing as it can alter a material's performance significantly. To understand how residual stresses form, is the first step to avoid them.

In this work residual stresses in an high strength low-alloyed steel are quantified, their formation mechanisms investigated and ways how to lower them are proposed during heat treatment and cooling. The mechanisms are investigated by means of simulation verified with measurements and tackle the stress evolution on three different length scales. On each scale residual stresses appear and decay with a characteristic length and in a material point stresses on all length scales are superimposed. Using finite element models on each scale, residual stress formation mechanisms are revealed and it can be determined, which system parameters have the greatest impact to lower them. This provides tools for manufacturing process for alloys with low residual stresses.

When discussing residual stresses in steels and presenting simulation results, there is always a need for additional experimental proof. But residual stresses of higher order are often not experimentally accessible. In the following section available residual stress measurement methods on different length scales are discussed as well as areas, where finite element simulation is vital to provide experimentally non-accessible information.

To understand the residual stress formation in steels, the metallurgical processes during cooling must be understood. This includes the understanding why certain elements are alloyed and how they affect phase transformations and resulting properties - as well as how the transformation from austenite to martensite and bainite proceeds and which specific features the product phases have.

The final seamless steel tubes are exposed to combined mechanical and environmental loading, which is a specific challenge. The combination of

high local stresses (whether due to application or residual stresses) and corrosive media can accelerate component failure. Especially environments that promote hydrogen uptake are crucial for high strength steels, since with increasing strength they become more susceptible to hydrogen induced failures. This must be avoided either by a reduction of stresses due to bigger cross sections with lower strength steels or, to save material and still maintain component integrity, by developing new high strength steels with reduced residual stresses.

The following introduction gives a brief overview of how residual stresses can be determined, and the use of simulation to provide additional information will be motivated. Then the manufacturing process of seamless steel tubes is presented, to show when the residual stresses form along the production line. To understand residual stress formation mechanisms in low alloyed steels, the role of phase transformation and alloying elements and how they affect interaction with hydrogen and sour gas is discussed.

Finally the working and modeling approach is presented to demonstrate for a selected steel grade how residual stresses form on the macro- to meso- and micro-scale using experimentally validated finite element models.

## 1.2 Residual stresses

Residual stresses are self-equilibrated stresses which exist without external loading [1]. The internal stress level is superimposed with external stresses during loading, and thus decrease the materials' load bearing capacity.

In combined loading with corrosive environments and mechanical loading, residual stresses can enhance corrosion and hydrogen related damage. As the investigated seamless steel tubes are used in corrosive environments with sour gas ( $H_2S$ ), hydrogen can be absorbed due to the surface corrosion process [2] and favor hydrogen induced cracking (HIC) mechanisms as well as sulfide stress cracking (SSC) [3].

Bouchard [4] investigated how the scale of residual stress drives the growth of structurally significant cracks for steel welds. He pointed out, when the length of a plastic defect approaches the length of the residual stress scale, the stresses on that scale provide no further driving force. Thus the significance of the residual stress contribution to drive structurally significant cracks is ranked macro > meso > micro. Bouchard and Withers also grouped the residual stresses into three characteristic scales  $\lambda$  over which they self-equilibrate: Type I residual stresses where  $\lambda$  is of the component size, type II stresses there  $3g \leq \lambda \leq 10g$  and type III residual stresses with  $\lambda \leq g$  where  $g$  denotes the grain size of the material.

In the investigated steel, the mechanisms of higher order cannot strictly be correlated with grain size, and thus the residual stresses are grouped into three categories with respect to their characteristic length scale: (i)

macroscopic on the component scale (ii) mesoscopic stresses around segregation lines with  $1g \leq \lambda \leq 3g$  and (iii) microscopic residual stresses around precipitates and inclusions with  $\lambda \leq 1 - 2g$ , see 1.1 after [1].

In this work residual stresses are referred to as "macroscopic" if the characteristic length ranges from millimeters to meters and covers the investigated components' dimensions. The "mesoscopic" residual stresses appear on an intermediate scale from millimeters to micrometers. During phase transformation to martensite and bainite lattice distortion can cause stresses on a scale that can be considered mesoscopic. They include stresses within former austenite grains in the new martensite or bainite substructure and depend on crystallographic factors, orientations, volume expansions, etc. These residual stresses can hardly be altered in the manufacturing process and are considered an inherent property of the microstructure. Thus, the selection of the mesoscopic scale for this work is oriented close to the manufacturing process and instead of investigating mesoscopic stresses on a martensite/bainite substructure level in detail we focus on the mesoscopic stresses caused by segregation lines. The segregation lines (so called "lines" but in reality 2D planes) are caused during casting due to enrichment of alloying elements in inter-dendritic spaces and have different chemistry than the initially formed ferritic dendrite. These local inhomogeneities cause different thermal expansion, volume expansion, transformation start temperatures and thus residual stresses. Residual stress measurements on this length scale for simulation comparison, require extensive experimental effort and very precise sample preparation. Since common techniques, such as X-ray diffraction require a prior determination of the chemical profile to compensate measured lattice parameters for the chemical contribution, and an unstrained lattice parameter as a strain reference must be determined. So for this application the developed experimentally verified macroscopic model is a way to give calculated estimates for residual stresses on an intermediate scale, which are experimentally difficult to access.

The third order, or microscopic residual stresses appear on a characteristic length scale from nanometers to micrometers and cover residual stresses around precipitates, voids, dislocations. Especially precipitates play an important role for designing hydrogen-resistant steel since in the recent past their potential for beneficial hydrogen trapping [5] was explored for applications with low hydrogen concentrations. They can act as so-called "deep traps" with high binding energies for hydrogen. Thus we focus on the residual stress fields around precipitates as hydrogen can locally accumulate there.

Residual stresses can never be measured directly and are always calculated from measured strains using assumed or measured elastic properties. The penetration depth versus the spatial resolution [6] decides the selection of the appropriate measurement technique for the application at hand.

To determine residual stresses on a macroscopic level, strains can be



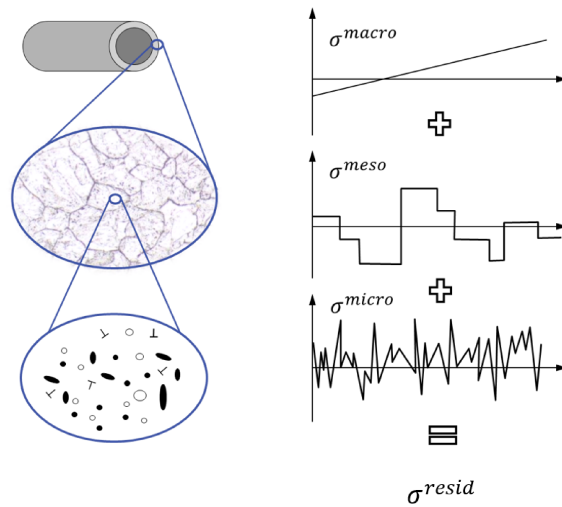


**Figure 1.1:** Schematic depiction of residual stresses in seamless tubes at different length scales.

measured using different destructive techniques, for example hole-drilling techniques or cut compliance methods. Both techniques release residual stresses in stepwise procedures by partial drilling or cutting [6]. The removal of cross section leads to a new residual stress equilibrium, which is accompanied by strains that are detected with strain gauges or optical methods and the released stress can be calculated using Hooke's law [1].

Non destructive measurements are for example diffraction measurements, which also provide higher spatial resolution [6]. For engineering materials neutron diffraction and X-ray diffraction techniques are available. Neutron diffraction reaches high penetration depths of several centimeters for engineering materials with good spatial resolution [1]. The detected lattice strain is an average value over the irradiated strain gauge volume. It is important to adjust or chose proper gauge volume sizes with respect to the investigated microstructure to get statistically liable data. For high-energy (or hard) X-ray diffraction measurements with 20-300 keV the gauge volume is usually relatively long (up to 1 mm) and thin (  $200 \times 200 \mu\text{m}$ ) due to the beam alignment, which can be disadvantageous for some component measurements. For high-energy X-rays the penetration depth in engineering materials is also high (up to several cm, depending on the intensity and exposure time) and with optical aperture the gauge volume can also be shortened [7]. There is conventional X-ray diffraction on a laboratory scale with only a few  $\mu\text{m}$  penetration depth, which is a limiting factor for in-depth measurements, but can be advantageous if for example after surface treatment surface residual stresses should be determined. Then a plane stress state can be assumed in the measurement volume [1].

Macroscopic residual stresses are relevant in steel components for example after cooling [8], after hardening [9] or after welding [10, 11]. In all these cases, the residual strains are assessed after the investigated production step- but the evolution however can be assessed using an accompanying finite element simulation.

For higher local resolution and also multi-phase states diffraction methods can be employed, to determine strains (stresses) during in-situ mechanical loading [12]. When phase transformation is involved, residual stresses are always determined in the final state [13] and mechanical properties, thermal properties and metallurgical properties vary strongly and thus correlating measured stresses to strains is difficult. In this work' simulation framework the phase kinetics and changes in material properties are determined separately and combined in a phase transformation model.

Microscopic stresses can be determined using high-resolution transmission electron microscopy (HR-TEM), as Douin and coworkers did for inclusions in aluminium [14]. In steels, this is more difficult due to the high defect densities, but global lattice strains can be determined in duplex steels [15] using SEM. And residual stresses around a single inclusion of 10  $\mu\text{m}$  have been studied by [16] in high strength steels using X-ray micro-tomography, experimentally and using an elasto-plastic finite element model. For designing low-residual stress steels, a comparison of relevant inclusions is presented in this work. This is supposed to allow a rough classification of precipitates on the one hand by their trapping behavior and on the other hand by their residual stress formation potential.

### 1.3 Manufacturing process

The hot rolling process for seamless steel tubes consists of nine main processing steps depicted in Fig. 1.2. First (a), the bloom in the as-cast condition is cut into billets of the correct weight for the final tube's dimensions. Then the billets are transported to a (b) rotary heating furnace with a temperature of about 1300°C depending on the material, to dissolve and homogenize all alloying elements in the matrix. Next the billet is transported to (c) a cross-roll-piercer, where, based on the Mannesmann principle, a hollow cylinder with specific inner diameter and wall thickness is formed [17]. Then the hollow work piece is attached to a mandrel bar and on (d) a push-bench pushed through a setup of non-driven three-roll-cages and elongated to a maximum length of 22.9 m. A (e) reeler releases the inner mandrel bar followed by (f) a wall thickness inspection. Then, in thermo-mechanically controlled processes, an (j) intermediate cooling step with phase transformation follows, to reach smaller grain sizes. A (g) reheating furnace heats the tube shell to 800 to 1000°C and is followed by the final shaping process: (h) the stretch reducing mill. There the tube shell is elongated with a maximum of 28

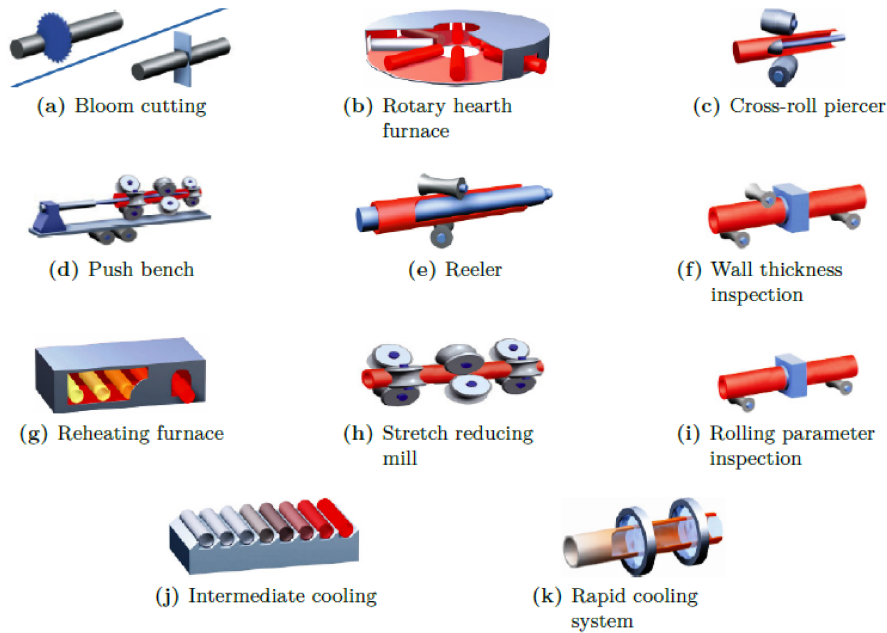


**Figure 1.2:** With permission from [7]: Schematic depiction of the seamless tube manufacturing process with the main process steps (a) to (i) and two intermediate process steps for thermo-mechanically controlled process (TMCP). Step (j) would be subsequent to (f) and (k) after (h).

driven three-roll-cages with progressively increasing rotation speed to its final shape. In the thermo-mechanically controlled process (TMCP), the tube is (k) rapidly cooled to guarantee a controlled phase transformation. If a subsequent heat treatment is required, the optional rapid cooling is skipped and the (i) parameter inspection follows directly. For further details on the manufacturing the reader is referred to [7, 18]

In a subsequent heat treatment the tube is austenitized, quenched and tempered (QT) once. This process could be repeated for additional grain refinement, which is not necessary in the investigated case. The austenitization allows homogenization of solute alloying elements in austenite and releases microstructural textures after rolling and with subsequent quenching gives grain refinement. The quenching adjusts a martensitic microstructure with high strength, but poor toughness. To increase toughness a subsequent tempering step releases internal stresses in martensite, reduces the dislocation density and causes precipitation in martensite.

Since in both processing routes, the TMCP and QT, the final cooling step (rapid cooling or quenching) causes phase transformation from austenite to martensite/bainite and induces residual stresses, the focus of this work is on investigating this step (and subsequent tempering for QT when stresses are

released). The main focus on this work is on residual stress evolution in a QT steel grade. The formation mechanisms can however be transferred to TM grades as well.

## 1.4 Material

The investigated steels in this work are two T95 grades following API standard 5CT [19]. The carbon contents of these steels are 0.31wt%C for steel A and 0.25wt%C for steel B. The latter was developed as sour-gas resistant steel grade and thus the main research focus is on this material. The included publications refer to this grade.

### 1.4.1 Alloying concept

For sour gas resistant seamless steel tubes of high strength a fine-grained tempered martensitic microstructure ( $\sigma_Y > 750$  MPa) and high toughness [19] is required. For this steel class grain refinement and precipitation strengthening are the most relevant strengthening mechanisms [20].

Precipitates in low-alloyed steel form at different process steps along the manufacturing line. Beginning with casting, where oxides and high temperature carbides and nitrides [21] are formed. They are summarized as so called primary carbides. During hot rolling and tempering precipitates containing Ti, V, Nb, Mo and Cr form [21].

The population precipitated in austenite during rolling or in the normalization heat treatment step is incoherent in the resulting martensite/bainite (TM) after phase transformation and also in the final quenched and tempered martensite (QT). Especially NbC due to its strain induced precipitation can prevent austenite grain growth during hot rolling as it changes the recrystallization temperature [22, 23, 24, 25].

No significant effect of microalloying elements on hydrogen uptake or corrosion resistance in sour gas ( $H_2S$ ) environment was found by Riecke in 1991 [26] for tempered ternary alloys. In his work he compared the effect of Mo, V, Ti, Nb and Zr for comparable weight fractions. Later, Mendibide presented an alloying concept for  $H_2S$  resistant steels and mentioned a positive effect of Cr from 0.7-1.3 wt% and also that Nb carbides apparently reduce hydrogen uptake during permeation charging [27]. This effect was not further discussed in detail but could be linked to a larger number of hydrogen traps, when Nb is additionally added.

In a broad variation of alloying and heat treatment, it turned out that higher tempering temperatures positively affect the corrosion resistance (as long as ferrite  $\alpha$  to austenite  $\gamma$  phase transformation is prevented) [28].

For the concept of quenched and tempered low-alloyed steels precipitates function as strengtheners, especially in QT grades, as the as-quenched

martensite strength is reduced in the subsequent tempering step. Ti, V, Nb, Mo are well known to be effective strengtheners [29, 30, 31]

The microalloying elements Ti, V and Nb all have in common, that they form MC carbides an NaCl like fcc rock salt structure and have a 'Baker-Nutting' [32] orientation relationship with bcc iron when formed in martensite/ferrite. If they were formed in austenite, they would exhibit the Kurdjumov-Sachs orientation relationship in bcc iron after phase transformation [33].

TiC and VC differ in their hydrogen trapping behavior. Vanadium forms non-stoichiometric  $V_4C_3$  carbides [34] with free interstitial lattice positions that have been shown to act as additional hydrogen traps [35, 36].

Fors compared in his work all micro-alloying elements with respect to their misfit strain as function of precipitate size first for VC [29] and later for many MC carbides [37]. Based on the lattice parameter for iron and MC carbides Fors calculated the misfit strain for disk like precipitates of Baker-Nutting orientation relationship as a function of slab thickness, i.e. the disk thickness. For the same slab thickness, TiC has about twice the misfit strain of VC and also requires twice the amount of geometrically necessary dislocations [37].

This is of particular interest, since small, incoherent particles show the highest strengthening effect due to the transition from Friedel to Orowan mechanism [38, 20]. Also the interface energy of the precipitate with the matrix plays a role, and this gives a relative comparison, which micro-alloying element should in theory have the highest strengthening potential.

## 1.4.2 Martensite and bainite

### Microstructure

When discussing residual stresses in low alloyed steels the constituent phases must be discussed. During accelerated cooling austenite  $\gamma$  transforms to martensite or bainite. Martensitic transformation is athermal- and the growth rate  $\dot{z}$  is proportional to cooling temperature increment over time  $\dot{T} = \frac{dT}{dt}$ . It starts at a specific temperature called martensite start temperature  $M_s$  and is a displacive shear deformation of the bcc lattice with respect to fcc austenite [39, 40].

The structure of martensite has a hierarchical order and the substructure sizes depend on the carbon content [39, 40]. For low carbon martensite (<0.5wt% carbon) laths with about 0.5  $\mu\text{m}$  width are formed. The size of its substructures also depends on the former austenite grain size and Mn content [41]. The main alloying elements controlling the martensite start temperature are C, Mn, Ni and Si [42].

Phase transformation to bainite is also displacive but below bainite transformation start temperature  $B_s$  it continues at constant temperature. There

are two to three different types of bainite depending on the literature. Ohtani [43] distinguishes three different types of bainite: (I) carbide free bainite, (II) lower bainite and (III) upper bainite. Bhadeshia [44] distinguishes only between upper and lower bainite.

The distinction between martensite and lower bainite can be made either via hardness, optically, EBSD and the orientation with respect to the former austenite grain or the orientation of cementite [40]. The relevant elements controlling bainite transformation are C, Mn, Mo, Cr [42].

### 1.4.3 Interaction with hydrogen

One of the first things known about the interaction of hydrogen and steel was that the susceptibility to hydrogen induced cracking (HIC) and hydrogen embrittlement (HE) increases with its strength [5].

The yield strength of steel depends on the grain size, dislocation density, solution strengtheners and interstitials. All of them hinder dislocations in their movement and thus raise the yield strength [20, 40]. But all these lattice defects act as potential hydrogen trapping sites.

For hydrogen the material's solubility refers to the sum of available interstitial lattice positions and trap sites with different binding energies per unit volume [45, 46]. A trap site can be any lattice defect: grain boundaries, dislocations, voids, precipitates and their interfaces, etc. The traps can be assumed to be in local thermodynamic equilibrium with the lattice and are categorized in shallow or weak traps with binding energies of around 30 kJ/mol (i.e. low angle grain boundaries, interstitial lattice positions, dislocations) and with increasing energy up to deep or strong traps with more than 60 kJ/mol (matrix/precipitate interfaces, carbon vacancies within precipitates, voids) [47].

When the available hydrogen concentration is small compared to the trap solubility (i.e. available trap positions per unit volume), deep traps are filled based on the thermodynamic equilibrium. When more hydrogen is available, also shallow traps are filled. For shallow traps little activation energy for de-trapping is needed and hydrogen can enter the lattice and easily diffuse. The sum of hydrogen at interstitial lattice positions and shallow traps is often referred to as mobile or diffusible hydrogen. But basically all trapped hydrogen is available for diffusion if activation energy for detrapping is provided. However, only the mobile or diffusible hydrogen concentration is responsible for hydrogen embrittlement [48].

Depending on the amount of hydrogen there are two different approaches how to prevent HE. (i) if the hydrogen concentration is lower than the trap solubility, hydrogen accumulates at positions with higher trapping energy that are energetically favorable. If the number of these deep trap sites is high enough to contain all present hydrogen, and the activation energy for escaping these traps cannot be overcome at application temperatures, they

are called 'beneficial' traps. They contain the hydrogen and there is no/little diffusible hydrogen in the matrix left (in equilibrium at a given temperature).

(ii) if the hydrogen concentration is higher than the solubility of the traps at a given temperature, there will be strongly and weakly trapped (diffusible) hydrogen present at trap sites and interstitial matrix positions. The weakly trapped hydrogen is able to diffuse within the matrix and will, when new defects such as crack tips or stress fields are formed, accumulate there due to higher number of available trapping positions in the strained lattice, especially if plastic deformation appears. The local hydrogen accumulation can then cause hydrogen induced damage.

In the case of sour gas, there is a constant supply of hydrogen and thus a condition (ii) with constantly higher hydrogen concentration than material solubility is assumed. In this case, diffusible, weakly trapped hydrogen is present in the matrix and the development approach is to reduce all internal stress concentrations- in form of residual stresses on all length scales, since they act superimposed to external loading. These stress fields and especially plastic deformation, increase the number of trap sites and thus the local hydrogen content, which can lead to hydrogen induced damage.

Moderer [28] tested a number of alloys with a broad variation of micro-alloying elements and the general trend is that with higher tempering temperatures better sour gas resistance can be achieved. And higher tempering temperatures require a delayed ferrite dissolution to austenite and precipitation strengtheners to sustain strength.

Sasaki reported in 2015 that MnS should be avoided in combination with hydrogen, as it acts as a pre-crack[49]. When hydrogen is present in the material (it can be absorbed by surface corrosion processes, cathodic protection, or supplied by hydrogen transport) it interacts with local microstructure. The interaction of hydrogen with residual stresses was investigated by Dabah [50] using high energy X-ray diffraction and was found that hydrogen reduces residual stresses during uptake in a reversible manner.

When discussing hydrogen uptake in low alloyed steels, one has to carefully compare the investigated microstructures. Martensite, bainite and ferrite have been repeatedly reported to differ with respect to hydrogen uptake and hydrogen embrittlement (HE). However, the reason for it is not often addressed: whether it is due to a difference in dislocation density, size of microstructural features such as grain size, block/subblock size and the corresponding boundaries per volume or due to retained austenite in martensite and bainite.

It has been reported that martensite can contain larger amounts of hydrogen compared to bainite and the hydrogen content in martensite increases with increasing carbon content [51]. In a study on martensite and bainite of the same carbon content of 0.2wt%C the susceptibility to hydrogen embrittlement in as-quenched martensite is higher than in bainite [48]. Martensite also shows higher hydrogen contents of 10 ppm compared to ferrite/pearlite

and bainite and has the highest fractions of diffusible hydrogen (4 out of 10 ppm). Note that the effect of the reported value in ppm strongly depends on the strength and microstructure. Bainite has been reported to be more susceptible to hydrogen embrittlement [52] compared to ferrite due to a larger number of weak traps that provide diffusible hydrogen during loading in a ferritic/bainitic steel.

Zuh reported, that [53] QT martensite shows, despite higher strength, better hydrogen resistance than quenched and partitioned (QP), intercritically annealed and quenched and partitioned (IAQP) microstructures containing retained austenite. But this effect seems also to strongly depend on the amount and morphology of retained austenite within the structure.

Regardless of the exact reason, whether it is due to a higher dislocation density, grain and subgrain boundary, number or carbides, etc., the approach selected in this thesis is to determine macroscopic and mesoscopic residual stresses as a function of process conditions for a microstructure containing martensite, tempered martensite and bainite, since higher hydrogen concentrations appear, where stress concentrations and plastic deformation appears.



## 1.5 State of the art

Calculating macroscopic residual stresses using a simulation approach for steels has been topic of research already in the previous century. Fernandes (1985) [54] and Denis [55] (1992) published a numerical framework that considers phase transformation effects in steels. These approaches require data on the material's mechanical, thermo-physical and transformation behavior. The kinetic behavior for displacive transformation was early described by Koistinen and Marburger [56] and was also used in this work. For the diffusive phase transformation approaches from Scheil based on the additivity principle [57], or a thermodynamic formulation from Lusk [58] used by Prime [9], are available.

The selected kinetic model in this work was developed by Garrett [59]. Schemmel [8] and coworkers already implemented a similar framework for residual stress formation in steel cylinders for continuous cooling. This work extends the framework from [8] to consider discontinuous cooling conditions resulting from the spray water quenching equipment, using an approach adapted from [60]. This combination allows calculating the residual stress evolution during discontinuous cooling and requires taking into account all previously formed product phases for a non-continuous cooling path.

On the mesoscopic scale it is known, that segregation can cause residual stresses. This effect is for example pronounced in nickel-base super alloys, where Epishin and coworkers modeled residual stresses due to interdendritic segregation taking into account the dendrite geometry [61]. In steels, solid state phase transformation is involved and may dominate the stress state. Siwecki and colleagues [62] calculated the residual stresses due to segregation in samples from heavy steel plates after quenching. In this experimental study the residual stresses are calculated from experimentally determined residual strains. Their calculations yield similar magnitudes of residual stresses for comparable chemical variations as considered in this work. In this work we numerically investigate the effect of the macroscopic stress state in addition to the isolated investigation of stresses due to chemical variation. Changes in local properties due to segregation are taken into account.

On the microscopic scale it is well established to calculate residual stresses around precipitates using numerical models. A qualitative comparison of different precipitate types with respect to their residual stress formation potential has also already been performed by [63]. These known approaches are combined in this work to complete the quantitative summary of residual stresses on three different length scales for low-alloyed steels.

## 1.6 Modeling

The finite element software ABAQUS [64] is used to implement and calculate the temperature, phase and residual stress evolution on different length scales. Four different finite element models are created to perform the calculations presented in the publications and are briefly introduced in this section.

### 1.6.1 Model types

The finite element model describing the macroscopic temperature and residual stress evolution is presented in detail in chapter 2. The thermal boundary conditions describing spray water cooling were adapted from [60]. The necessary mechanical properties were experimentally determined and include elastic and plastic properties of austenite, as-quenched martensite and bainite. The bainite samples for the mechanical material characterization were specially heat treated to adjust a >90% bainite microstructure. The thermo-physical properties were determined experimentally (thermal expansion, thermal conductivity, density, specific heat) as function of temperature for martensite and austenite. In bainite they are assumed to be similar to martensite. Temperature dependent Poisson's ratios for the phases were calculated using JMatPro [65]. The phase transformation kinetics was fitted to dilatometer curves at cooling rates ranging from 300 °C/s to 0.19 °C/s covering transformations to martensite, bainite and ferrite/pearlite. The kinetic parameters for the Koistinen and Marburger kinetic [56] describing the transformation to martensite and the bainite and ferrite phase transformation kinetic [59, 66] were adjusted both manually and using a least squares optimization routine in Python. Also a Scheil kinetic model [57] was fitted for bainite phase transformation using a Python routine. The phase transformation models as well as the material data were implemented in ABAQUS.

- Axisymmetric macroscopic model of a tube's cross section

This model is employed to calculate the macroscopic temperature, phase evolution and residual stresses as a function of radial position in a tube. Different tube geometries (177.8 mm outer diameter and 12.65 mm wall thickness and 200 mm outer diameter and 22.65 mm wall thickness) and cooling conditions are calculated. The cooling is implemented using a user defined subroutine applying a given amount of water represented by a temperature dependent heat transfer coefficient [67, 68] on the tube's inner and outer surface that accounts for the spray water cooling in the manufacturing process. In axial direction (i.e. z-direction) the mechanical boundary condition is a generalized plane strain condition ( $\varepsilon_z = \text{const.}$ ) and the thermal boundary condi-

tion accounts for heat transfer in axial direction. The thermal problem is solved first using axisymmetric, linear thermal elements DCX4 and subsequently the mechanical solution is calculated with the resulting temperature field using CAX4 elements. The element size is varying from 0.1265 mm to 0.2265 mm for the different dimensions.

The total strain tensor  $\varepsilon^t$  is decomposed into

$$\varepsilon_{ij}^t = \varepsilon_{ij}^{el} + \varepsilon_{ij}^p + \varepsilon_{ij}^{th} + \varepsilon_{ij}^{vol} + \varepsilon_{ij}^{trip} \quad (1.1)$$

The phase evolution for ferrite/pearlite, bainite and martensite has been similarly implemented by [8] and coworkers to investigate residual stresses in steel cylinders and was adapted in this work.

- Mesoscopic *generalized plane strain submodel*  
of an endless segregation plane within the tube to investigate the effect of the mesoscopic stress and temperature evolution on the mesoscopic scale. The boundary conditions are transferred from the macroscopic level. For a point on the inner and outer position the total strain of one element- which corresponds to an area of  $126.5 \times 126.5 \mu\text{m}$  with a segregation line thickness (calculated to adjust certain volume contents) of 20-100  $\mu\text{m}$ .
- Mesoscopic *generalized plane strain model without external loading*  
to isolate the effect of carbon content, volume expansion and phase transformation on residual stress formation for an infinite segregation plate. The martensite start temperature was varied based on local changes in carbon content determined by the martensite lattice parameter in stress free samples. The lattice strain in the segregation line can be correlated to a carbon fluctuation of maximum  $\pm 0.03\text{wt}\%$ . The lattice strain was determined in stress free samples to obtain a macroscopically unstressed reference strain and calculate the macroscopic residual stresses correctly. Metallurgical volume expansion and thermal expansion, which also change with local chemistry, were determined depending on the carbon content [69] and JMatPro [65]
- Microscopic model with single inclusion  
From a material's point of view all particles of different structure than the matrix can be referred to as precipitates, which can form either in the melt, austenite or some product phase. From a mechanical point of view and particularly when discussing strain fields around particles with Eshelby based eigenstrains, an inclusion is referred to as a region  $\Omega$  that is subjected to a stress-free eigenstrain- but is of the same elastic behavior as the matrix. An inhomogeneity has different elastic properties than the matrix [70]. This model is employed to calculate strain energies for  $\text{Mo}_2\text{C}$  carbides in iron.

- Microscopic model with multiple inclusions A submodel from [71] was adapted for modeling a volume element with multiple inclusions of oblate to prolate spherical shape with different aspect ratios and sizes. The cubic volume element is subjected to periodic boundary conditions and either (i) mechanical loading using a reference node to determine the Young's modulus as a function of precipitate phase fraction and (ii) thermal loading to calculate thermo-elastic residual stresses. This model is used to calculate the mesoscopic Young's modulus in a segregation line as a function of carbon content and precipitate volume fraction and thus the mesoscopic residual stresses. Also residual stresses due to thermal mismatch. Note that the inclusions are assumed to be mainly Cr rich cementite, as has been found by TEM and EDX measurements.

### 1.6.2 Phase transformation model

The Koistinen and Marburger model correlates the evolution of the displacive phase transformation from austenite to martensite with the cooling rate [56]. It describes an athermal transformation, since at constant temperature the cooling rate is zero and transformation stops.

Isothermal diffusive phase transformation was described 80 years ago by Avrami [72] and extended by Cahn with the principle of additivity [73]. It implies that the transformation progress at two different temperatures can be combined. Scheil further extended this approach and invented a method, where a fictitious time accounts for transformation at previous continuous cooling as if it had been isothermal and thus allows modeling phase evolution during non-isothermal cooling.

Another approach, considering the nucleation and growth of the product phase as it occurs in diffusive transformation was published by Garrett [59] and Mahnken [66]. This approach requires several fitting parameters (10 per transformation) but allows on the other hand a transformation description over a broader range of cooling rates.

The material model and the necessary data is described in detail in chapter 2. In this section the additional information on the numerical implementation is given and the following section describes the user subroutines SDVINI, USDFLD, EXPAN, HEATVAL, CREEP and FILM to describe the phase transformation and thermal process boundary conditions.

The user subroutines are solved at each integration point [64]. USDFLD returns a user defined number of field variables, which are each assigned to certain phases and influence the material properties. The user subroutines are initialized using SDVINI, where start values for the state variables are defined. State variables are for example phase fraction  $z$ , phase increment  $\Delta z$ , phase formation rates  $\dot{z} = dz/dt$ , temperature  $T$  and other internal variables. To initialize the user defined field, the following keywords must be included

in the .inp file: \*User Defined Field, \*Initial Conditions, type=SOLUTION, user and \*Initial Conditions, type=FIELD.

SDVINI

defines the initial values of the state variables

USDFLD

contains the implementation of the phase transformation models, i.e. the Koistinen and Marburger [56] kinetics for martensite formation, where the newly created phase increment per time for the time increment  $\Delta t$  and temperature increment  $\Delta T$  is a function of the kinetic parameter  $\beta$  if the temperature  $T$  is below martensite start temperature  $M_s$ :

$$\Delta z_M = \begin{cases} 0 & \text{if } T < M_s \\ -\beta \Delta T z_\gamma & \text{if } T > M_s \end{cases} \quad (1.2)$$

For transformation to bainite the newly created phase increment  $\Delta z_b$  is calculated following [59, 66] as a function of temperature  $T$ , the nucleation radius  $R$ , the critical nucleation radius  $R_{crit}$ , the free energy  $G_s$  and the austenite volume fraction  $z_\gamma$

$$\Delta z_B = \begin{cases} 0 & \text{if } T > \Theta_0 \\ \Delta z_b(T, R, R_{crit}, G_s, z_\gamma, \dots) & \text{if } T < \Theta_0 \end{cases} \quad (1.3)$$

With a critical nucleation radius  $R_{crit}$ , which is calculated as a function of temperature  $T$  and the parameters  $A_{1,Q}$  and  $\Theta_0$  by

$$R_{crit} = \frac{A_{1,Q} \Theta_0 (\Theta_0 - T)^{0.5}}{T (\Theta_0 - T)}. \quad (1.4)$$

The free energy  $G_s$  is

$$G_s = \frac{A_{3,Q} \Theta_0^2 (\Theta_0 - T)^{1.5}}{(\Theta_0 - T)^2}. \quad (1.5)$$

using parameter  $A_{3,Q}$ . The increment of the nucleation radius  $\Delta R$  is calculated as a function of temperature  $T$  and the parameters  $\alpha_{2u}$  and  $\Theta^*$  as

$$\Delta R = \alpha_{2u} \exp\left(\frac{-|T - \Theta^*|}{B_u}\right). \quad (1.6)$$

The current nucleation radius  $R$  at time increment  $i$  is

$$R_i = R_{i-1} + \Delta R. \quad (1.7)$$

If  $R_i$  exceeds the critical radius  $R_{crit}$  at time  $i$ ,  $R_{crit,i}$  then the phase formation rate  $\Delta\dot{z}_B$  is calculated as

$$\dot{z}_B = A_5 \exp\left(\frac{\Theta^* - T}{B_1}\right) \exp\left(\frac{-G_s}{RT}\right) \left\langle \frac{R - R_{crit}}{R} \right\rangle^n (z_\gamma)^\gamma \quad (1.8)$$

with  $A_5$ ,  $B_1$  and  $n$  as material parameters and  $R$  as the gas constant. The newly created phase increment  $\Delta z_B$  is calculated by

$$\Delta z_B = \dot{z}_B \Delta t. \quad (1.9)$$

The austenite phase fraction is reduced by the martensite and bainite increments

$$\Delta z_\gamma = -\Delta z_M - \Delta z_B \quad (1.10)$$

and the new austenite, martensite and bainite phase fractions are

$$z_{M,i} = z_{M,i-1} + \Delta z_M \quad (1.11)$$

$$z_{B,i} = z_{B,i-1} + \Delta z_B \quad (1.12)$$

$$z_{\gamma,i} = z_{\gamma,i-1} + \Delta z_\gamma. \quad (1.13)$$

UEXPAN

This subroutine governs the thermal and metallurgical expansions  $\varepsilon^{th}$  and  $\varepsilon^{vol}$ .

The thermal expansion increment is the phase-fraction weighted sum of the  $k = 0, \dots, N$  phases times the temperature increment:

$$\Delta\varepsilon^{th} = \sum_{k=0}^N \alpha_k z_k \Delta T \quad (1.14)$$

With  $\alpha_k$  being the thermal expansion coefficient of the phase  $k$ . The metallurgical volume strain increment due to phase transformation is

$$\Delta\varepsilon^{vol} = \sum_{k=0}^N \dot{z}_k (k_k T + d_k) \Delta t \quad (1.15)$$

where  $k_k T$  and  $d_k$  are parameters to describe a linear temperature dependence of the metallurgical expansion.

The returned strain increment EXPAN(1) is  $\Delta\varepsilon^{th} + \Delta\varepsilon^{vol}$ .

HETVAL

The latent heat returns the heat flux increment  $\Delta\dot{Q}^{TR}(\dot{z}_k)$  ( $J/m^3s$ ), which is created by dissipation during phase transformation.  $H$  is implemented following [57] as:

$$\Delta\dot{Q}^{TR}(\dot{z}_k) = \Delta H_k \Delta\dot{z}_k. \text{ for } k = 1, \dots, N \quad (1.16)$$

$H_k$  is determined from differential scanning calorimetry curves at different cooling rates for the individual phases and is the integral of the specific heat (J/kgK) over temperature.

#### CREEP

In order to describe the phenomenon of transformation induced plasticity, the plastic strain during transformation is implemented using the subroutine creep.

The creep subroutine returns the sum of the creep strain increment  $\Delta\varepsilon^{trip}$  and classical creep strain increment  $\Delta\varepsilon^{cr}$ . However, classical creep is only considered when calculating the tempering kinetics and is not active in the quenching procedures. Leblond's initial formulation of the TRIP strain [74]

$$\varepsilon_{ij}^{trip} = K\sigma_{ij}\Phi_z \quad (1.17)$$

$$\Phi_z = z(2 - z) \quad (1.18)$$

where  $K$  is some constant at the order of  $10^{-4}$  MPa $^{-1}$ ,  $\sigma_{ij}$  is the applied stress and  $\Phi_z$  a saturation function. The incremental formulation is

$$\Delta\varepsilon_{ij}^{trip} = K S_{ij} \Phi'_z \Delta t \quad (1.19)$$

$$\frac{d\Phi_z}{dt} = \Phi'_z = 2\dot{z} - 2z\dot{z} = 2\dot{z}(1 - z) \quad (1.20)$$

The creep formulation in ABAQUS however is

$$\Delta\varepsilon_{ij}^{cr} = \frac{1}{3}\Delta\varepsilon^{sw} R_{ij} + \Delta\varepsilon^{cr} n_{ij}. \quad (1.21)$$

Where  $R_{ij}$  denotes the matrix of swelling ratios and  $n_{ij}$  is the gradient of the deviatoric stress potential, which is defined as

$$n_{ij} = \frac{\partial Q}{\partial \sigma_{ij}} = \frac{3}{2} \frac{S_{ij}}{Q} \quad (1.22)$$

with  $Q$  as the equivalent stress,  $\sigma_{ij}$  is the applied stress and  $S_{ij}$  the deviatoric stress tensor. And since  $\Delta\varepsilon^{sw}=0$

$$\Delta\varepsilon_{ij}^{cr} = \Delta\varepsilon^{cr} \frac{3}{2} \frac{S_{ij}}{Q}. \quad (1.23)$$

The creep formalism is used to implement the TRIP strain, i.e.

$$\Delta\varepsilon_{ij}^{cr} \equiv \Delta\varepsilon_{ij}^{trip}. \quad (1.24)$$

Thus the TRIP strain increment  $\Delta\varepsilon^{trip}$  is calculated for each product phase  $k$  as

$$\Delta\varepsilon_k^{trip} = 2K_k Q f'(z_1 \dots z_N) \dot{z}_k \Delta t \quad (1.25)$$

Note that the interaction with other product phases evolving simultaneously is accounted for by the saturation function  $f'(z, \dots, z_n)$  with

$$f'(z_1 \dots z_N) = \left( 1 - \sum_{i=1}^N z_i \right). \quad (1.26)$$

Classical creep is implemented by means of a temperature dependent power law. Since during tempering the stresses relax in as-quenched martensite/ bainite the creep law was parametrized with measurements on as-quenched martensite.

#### FILM

The FILM subroutine applies a given amount of water represented by a temperature dependent heat transfer coefficient to the inner and outer surface of the tube's axisymmetric model. The heat transfer coefficient is calculated following [67, 68].

In reality the cooling boxes are fixed and the tube moves along them. In the model it is more efficient to keep the tube fixed and to let the cooling boxes move with a velocity  $v$ . With the given tube geometry, the position of each box  $x_i$  is calculated over time. If the position of a point on the tube coincides with the position of one of the cooling boxes, then the heat transfer coefficient is switched to corresponding temperature dependent values. Otherwise, a fixed coefficient for contact with air is applied.



## 1.7 Main findings

The main findings of this work are:

- An experimentally verified process model accounting for phase transformation during accelerated cooling of steel tubes, that yields residual stress distributions

*Specifically:* After quenching: Residual stresses in tangential and axial direction range from -800 MPa to 700 MPa. Radial stresses are below 100 MPa.

After tempering: Macroscopic residual stresses in all directions are reduced to  $\pm 20$  MPa.

- Low-residual stress cooling concepts for the investigated material are derived: Reduction of temperature gradients, cooling from both sides and phase transformation initiated on inner and outer surface yields low residual stresses

*Specifically:* Residual stresses of dimension  $177.8 \times 12.65$  mm can be reduced to  $\pm 250$  MPa using internal and external cooling.

- The macroscopic residual stress state is independent of microstructure: low-residual stress distributions can be achieved with mostly martensite but also mostly bainite microstructure.

*Specifically:* Residual stress distributions with tangential and axial stresses of  $\pm 250$  MPa can be achieved with both, mainly martensitic or mainly bainitic microstructure.

- Segregation lines can locally cause residual stresses. After accelerated cooling they depend on local transformation start temperatures and after tempering on the different coefficients of thermal expansion.

*Specifically:* For an experimentally determined change in local chemistry residual stresses of  $\pm 30$  MPa remain in segregated areas and matrix.

- Residual stresses around inhomogeneities, in this work referred to as microscopic residual stresses, remain after tempering for secondary precipitates and can be present after accelerated cooling for primary carbides and oxides.

*Specifically:* Average thermo-elastic residual stresses in the matrix are 30 to 60 MPa. Local residual stresses can range up to 500 MPa.

- For Mo<sub>2</sub>C precipitates the shape and orientation is determined by interface anisotropy.

*Specifically:* The incoherent interface energy is about 3 times higher than the mechanical strain energy for the investigated inclusion size. Both interface and strain energy yield a minimum for inclusion orientations observed in reality.

The developed models allow the calculation of residual stresses in low-alloyed steels on three different length scales. Strategies for cost efficient processing routes yielding low residual stresses can be derived on this basis.

# Bibliography

- [1] P. J. Withers and H. K.D.H. Bhadeshia. Residual stress part 1 - Measurement techniques. *Materials Science and Technology*, 17(4):355–365, 2001. ISSN 02670836. doi: 10.1179/026708301101509980.
- [2] H. Kaesche. *Die Korrosion der Metalle*, 2011. URL <http://link.springer.com/10.1007/978-3-642-18428-4>.
- [3] W. R. Revie. *Uhlig's Corrosion Handbook*. John Wiley & Sons, Inc., third edit edition, 2011. ISBN 964-7445-88-1.
- [4] P. J. Bouchard and P. J. Withers. The appropriateness of residual stress length scales in structural integrity. *Journal of Neutron Research*, 12(1-3):81–91, 2004. ISSN 14772655. doi: 10.1080/10238160410001734504.
- [5] A. Turnbull. Perspectives on hydrogen uptake, diffusion and trapping. *International Journal of Hydrogen Energy*, 40(47):16961–16970, 2015. ISSN 03603199. doi: 10.1016/j.ijhydene.2015.06.147. URL <http://dx.doi.org/10.1016/j.ijhydene.2015.06.147>.
- [6] N. S. Rossini, M. Dassisti, K. Y. Benyounis, and A. G. Olabi. Methods of measuring residual stresses in components. *Materials and Design*, 35:572–588, 2012. ISSN 02641275. doi: 10.1016/j.matdes.2011.08.022. URL <http://dx.doi.org/10.1016/j.matdes.2011.08.022>.
- [7] G. Winter. *Macro- and Microscopic Properties of Gradient Ultra High Strength Thermo-Mechanically Rolled Seamless Steel Tubes*. Dissertation, Montanuniversitaet Leoben, 2015.
- [8] M. Schemmel, P. Prevedel, R. Schöngrundner, W. Ecker, and T. Antretter. Size effects in residual stress formation during quenching of cylinders made of hot-work tool steel. *Advances in Materials Science and Engineering*, 2015, 2015. ISSN 16878442. doi: 10.1155/2015/678056.
- [9] M. B. Prime, V. C. Prantil, P. Rangaswamy, and F. P. García. Residual stress measurement and prediction in a hardened steel ring. *Materials Science Forum*, 347(January 2014):223–228, 2000. ISSN 02555476. doi: 10.4028/www.scientific.net/msf.347-349.223.

- [10] D. Deng. FEM prediction of welding residual stress and distortion in carbon steel considering phase transformation effects. *Materials and Design*, 30(2):359–366, 2009. ISSN 02641275. doi: 10.1016/j.matdes.2008.04.052.
- [11] M. Islam, A. Buijk, M. Rais-Rohani, and K. Motoyama. Simulation-based numerical optimization of arc welding process for reduced distortion in welded structures. *Finite Elements in Analysis and Design*, 84: 54–64, 2014. ISSN 0168874X. doi: 10.1016/j.finel.2014.02.003. URL <http://dx.doi.org/10.1016/j.finel.2014.02.003>.
- [12] J. Johansson, M. Odén, and X. H. Zeng. Evolution of the residual stress state in a duplex stainless steel during loading. *Acta Materialia*, 47(9): 2669–2684, 1999. ISSN 13596454. doi: 10.1016/S1359-6454(99)00149-4.
- [13] H. Dai, J.A. Francis, H.J. Stone, H.K.D.H. Bhadeshia, and P.J. Withers. Characterizing phase transformations and their effects on ferritic weld residual stresses with X-rays and neutrons. *Metallurgical and Materials Transactions A: Physical Metallurgy and Materials Science*, 39 (13):3070–3078, 2008. ISSN 10735623. doi: 10.1007/s11661-008-9616-0.
- [14] J. Douin, P. Donnadiou, and F. Houdellier. Elastic strain around needle-shaped particles embedded in Al matrix. *Acta Materialia*, 58(17):5782–5788, 2010. ISSN 13596454. doi: 10.1016/j.actamat.2010.06.053. URL <http://dx.doi.org/10.1016/j.actamat.2010.06.053>.
- [15] J. Kang, Y. Ososkov, J.D. Embury, and D.S. Wilkinson. Digital image correlation studies for microscopic strain distribution and damage in dual phase steels. *Scripta Materialia*, 56(11):999–1002, 2007. ISSN 13596462. doi: 10.1016/j.scriptamat.2007.01.031.
- [16] A. Stienon, A. Fazekas, J. Y. Buffière, A. Vincent, P. Daguier, and F. Merchi. A new methodology based on X-ray micro-tomography to estimate stress concentrations around inclusions in high strength steels. *Materials Science and Engineering A*, 513-514(C):376–383, 2009. ISSN 09215093. doi: 10.1016/j.msea.2009.02.008.
- [17] R. Pschera. *Modellierung und Simulation des Schrägwalzens von Rundknüppeln zu Rohrluppen unter Berücksichtigung der Mikrostrukturentwicklung und der Umformbarkeit von Primärstrukturen*. Dissertation, Montanuniversitaet Leoben, 2009.
- [18] J. Klarner. *Thermomechanische Behandlung beim Walzen von nahtlosen Stahlrohren*. Dissertation, Montanuniversitaet Leoben, 2009.
- [19] API 5CT. API 5CT: Specification for Casing and Tubing. *API Specification*, page 306, 2005.

- [20] G. Gottstein. *Physikalische Grundlagen der Materialkunde*. Springer-Lehrbuch. Springer Berlin Heidelberg, Berlin, Heidelberg, 1998. ISBN 978-3-540-62670-1. doi: 10.1007/978-3-662-09331-3. URL <http://link.springer.com/10.1007/978-3-662-09331-3>.
- [21] S. Zamberger, T. Wojcik, J. Klarner, G. Klösch, H. Schifferl, and E. Kozeschnik. Computational and experimental analysis of carbonitride precipitation in tempered martensite. *Steel Research International*, 84(1):20–30, 2013. ISSN 16113683. doi: 10.1002/srin.201200047.
- [22] S. S. Hansen, J. B.V. Sande, and M. Cohen. Niobium carbonitride precipitation and austenite recrystallization in hot-rolled microalloyed steels. *Metallurgical Transactions A*, 11(3):387–402, 1980. ISSN 03602133. doi: 10.1007/BF02654563.
- [23] B. Dutta and C. M. Sellars. Effect of composition and process variables on Nb(C, N) precipitation in niobium microalloyed austenite. *Materials Science and Technology (United Kingdom)*, 3(3):197–206, 1987. ISSN 17432847. doi: 10.1179/mst.1987.3.3.197.
- [24] B. Dutta, E. Valdes, and C. M. Sellars. Mechanism and kinetics of strain induced precipitation of Nb(C,N) in austenite. *Acta Metallurgica Et Materialia*, 40(4):653–662, 1992. ISSN 09567151. doi: 10.1016/0956-7151(92)90006-Z.
- [25] J. Fernández, S. Illescas, and J. M. Guilemany. Effect of microalloying elements on the austenitic grain growth in a low carbon HSLA steel. *Materials Letters*, 61(11-12):2389–2392, 2007. ISSN 0167577X. doi: 10.1016/j.matlet.2006.09.021.
- [26] E. Riecke and B. Johnen. Einflüsse von Mo, V, Nb, Ti, Zr und deren Karbiden auf die Korrosion und Wasserstoffaufnahme von Eisen in H<sub>2</sub>S-haltigen Lösungen. *Materials and Corrosion*, 42(10):528–536, 1991. ISSN 15214176. doi: 10.1002/maco.19910421005.
- [27] C. Mendibide and T. Sourmail. Composition optimization of high-strength steels for sulfide stress cracking resistance improvement. *Corrosion Science*, 51(12):2878–2884, 2009. ISSN 0010938X. doi: 10.1016/j.corsci.2009.08.013. URL <http://dx.doi.org/10.1016/j.corsci.2009.08.013>.
- [28] L. Moderer. Sauergasbeständigkeit neuer hochfester Stähle. 2012.
- [29] D. H.R. Fors, S.A.E. Johansson, M.V.G. Petisme, and G. Wahnström. Theoretical investigation of moderate misfit and interface energetics in the Fe/VN system. *Computational Materials Science*, 50(2):550–559, 2010. ISSN 09270256. doi: 10.1016/j.commatsci.2010.09.018. URL <http://dx.doi.org/10.1016/j.commatsci.2010.09.018>.

- [30] T. Depover, O. Monbaliu, E. Wallaert, and K. Verbeken. Effect of Ti, Mo and Cr based precipitates on the hydrogen trapping and embrittlement of Fe-C-X Q&T alloys. *International Journal of Hydrogen Energy*, 40(47):16977–16984, 2015. ISSN 03603199. doi: 10.1016/j.ijhydene.2015.06.157. URL <http://dx.doi.org/10.1016/j.ijhydene.2015.06.157>.
- [31] G. Xu, X. Gan, G. Ma, F. Luo, and H. Zou. The development of Ti-alloyed high strength microalloy steel. *Materials and Design*, 31(6):2891–2896, 2010. ISSN 02641275. doi: 10.1016/j.matdes.2009.12.032. URL <http://dx.doi.org/10.1016/j.matdes.2009.12.032>.
- [32] R. G. Baker, D. G. Brandon, and J. Nutting. The growth of precipitates. *Philosophical Magazine*, 4(48):1339–1345, 1959. ISSN 00318086. doi: 10.1080/14786435908233369.
- [33] T. N. Baker. Processes, microstructure and properties of vanadium microalloyed steels. *Materials Science and Technology*, 25(9):1083–1107, 2009. ISSN 02670836. doi: 10.1179/174328409X453253.
- [34] S. Yamasaki and H. K.D.H. Bhadeshia. Modelling and characterisation of Mo<sub>2</sub>C precipitation and cementite dissolution during tempering of Fe-C-Mo martensitic steel. *Materials Science and Technology*, 19(6):723–731, 2003. ISSN 02670836. doi: 10.1179/026708303225002929.
- [35] J. Takahashi, K. Kawakami, and T. Tarui. Direct observation of hydrogen-trapping sites in vanadium carbide precipitation steel by atom probe tomography. *Scripta Materialia*, 67(2):213–216, 2012. ISSN 13596462. doi: 10.1016/j.scriptamat.2012.04.022. URL <http://dx.doi.org/10.1016/j.scriptamat.2012.04.022>.
- [36] J. Takahashi, K. Kawakami, and Y. Kobayashi. Origin of hydrogen trapping site in vanadium carbide precipitation strengthening steel. *Acta Materialia*, 153:193–204, 2018. ISSN 13596454. doi: 10.1016/j.actamat.2018.05.003. URL <https://doi.org/10.1016/j.actamat.2018.05.003>.
- [37] D.H.R. Fors and G. Wahnström. Theoretical study of interface structure and energetics in semicoherent Fe(001)/MX(001) systems (M=Sc, Ti, V, Cr, Zr, Nb, Hf, Ta; X=C or N). *Physical Review B - Condensed Matter and Materials Physics*, 82(19):1–13, 2010. ISSN 10980121. doi: 10.1103/PhysRevB.82.195410.
- [38] J. Friedel and P. Feltham. The mechanism of work-hardening and slip-band formation. *Proceedings of the Royal Society of London. Series A. Mathematical and Physical Sciences*, 242(1229):147–159, 1957. ISSN 2053-9169. doi: 10.1098/rspa.1957.0163.

- [39] J.W. Christian. *Theory of Transformations in Metals and Alloys*. Pergamon Press Ltd, third edit edition, 2002. ISBN 0080440193.
- [40] H. K.D.H. Bhadeshia and R. Honeycombe. *Steels Microstructure and properties*. Elsevier, third edit edition, 2006. ISBN 9780750680844. doi: 10.1016/B978-0-7506-8084-4.X5000-6. URL <https://linkinghub.elsevier.com/retrieve/pii/B9780750680844X50006>.
- [41] S. Morito, H. Yoshida, T. Maki, and X. Huang. Effect of block size on the strength of lath martensite in low carbon steels. *Materials Science and Engineering A*, 438-440(SPEC. ISS.):237–240, 2006. ISSN 09215093. doi: 10.1016/j.msea.2005.12.048.
- [42] S.M.C. Van Bohemen. Bainite and martensite start temperature calculated with exponential carbon dependence. *Materials Science and Technology*, 28(4):487–495, 2012. ISSN 02670836. doi: 10.1179/1743284711Y.0000000097.
- [43] H. Ohtani, S. Okaguchi, Y. Fujishiro, and Y. Ohmori. Morphology and properties of low-carbon bainite. *Metallurgical Transactions A*, 21(3): 877–888, 1990. ISSN 03602133. doi: 10.1007/BF02656571.
- [44] H. K.D.H. Bhadeshia. *Bainite in Steels*. IOM Communications Ltd, 2nd editio edition, 2001. ISBN 1861251122.
- [45] J. Svoboda and F. D. Fischer. Modelling for hydrogen diffusion in metals with traps revisited. *Acta Materialia*, 60(3):1211–1220, 2012. ISSN 13596454. doi: 10.1016/j.actamat.2011.11.025. URL <http://dx.doi.org/10.1016/j.actamat.2011.11.025>.
- [46] A. Drexler, T. Depover, K. Verbeken, and W. Ecker. Model-based interpretation of thermal desorption spectra of Fe-C-Ti alloys. *Journal of Alloys and Compounds*, 789:647–657, 2019. ISSN 09258388. doi: 10.1016/j.jallcom.2019.03.102. URL <https://doi.org/10.1016/j.jallcom.2019.03.102>.
- [47] A. Drexler, T. Depover, S. Leitner, and W. Verbeken, K.and Ecker. Microstructural based hydrogen diffusion and trapping models applied to Fe-C[sbnd]X alloys. *Journal of Alloys and Compounds*, 826:154057, 2020. ISSN 09258388. doi: 10.1016/j.jallcom.2020.154057. URL <https://doi.org/10.1016/j.jallcom.2020.154057>.
- [48] T. Depover, E. Wallaert, and K. Verbeken. On the synergy of diffusible hydrogen content and hydrogen diffusivity in the mechanical degradation of laboratory cast Fe-C alloys. *Materials Science and Engineering A*, 664:195–205, 2016. ISSN 09215093. doi: 10.1016/j.msea.2016.03.107. URL <http://dx.doi.org/10.1016/j.msea.2016.03.107>.

- [49] D. Sasaki, M. Koyama, and H. Noguchi. Factors affecting hydrogen-assisted cracking in a commercial tempered martensitic steel: Mn segregation, MnS, and the stress state around abnormal cracks. *Materials Science and Engineering A*, 640:72–81, 2015. ISSN 09215093. doi: 10.1016/j.msea.2015.05.083. URL <http://dx.doi.org/10.1016/j.msea.2015.05.083>.
- [50] E. Dabah, T. Kannengiesser, D. Eliezer, and T. Boellinghaus. Hydrogen interaction with residual stresses in steel studied by synchrotron X-ray diffraction. *Materials Science Forum*, 772:91–95, 2014. ISSN 02555476. doi: 10.4028/www.scientific.net/MSF.772.91.
- [51] D. Pérez Escobar, T. Depover, E. Wallaert, L. Duprez, M. Verhaege, and K. Verbeken. Thermal desorption spectroscopy study of the interaction between hydrogen and different microstructural constituents in lab cast Fe-C alloys. *Corrosion Science*, 65:199–208, 2012. ISSN 0010938X. doi: 10.1016/j.corsci.2012.08.017.
- [52] J. H. Park, M. S. Oh, and S. J. Kim. Effect of bainite in microstructure on hydrogen diffusion and trapping behavior of ferritic steel used for sour service application. *Journal of Materials Research*, 32(7):1295–1303, 2017. ISSN 20445326. doi: 10.1557/jmr.2016.480.
- [53] X. Zhu, K. Zhang, W. Li, and X. Jin. Effect of retained austenite stability and morphology on the hydrogen embrittlement susceptibility in quenching and partitioning treated steels. *Materials Science and Engineering A*, 658:400–408, 2016. ISSN 09215093. doi: 10.1016/j.msea.2016.02.026. URL <http://dx.doi.org/10.1016/j.msea.2016.02.026>.
- [54] F. M. B. Fernandes, S. Denis, and A. Simon. Mathematical model coupling phase transformation and temperature evolution during quenching of steels. *Materials Science and Technology*, 1(10):838–844, oct 1985. ISSN 02670836. doi: 10.1179/026708385790123991. URL <http://openurl.ingenta.com/content/xref?genre=article{%&}issn=0267-0836{%&}volume=1{%&}issue=10{%&}spage=838>.
- [55] S. Denis, D. Farias, and A. Simon. Mathematical Model Coupling Phase Transformations and Temperature Fvolutions in Steels. *ISIJ International*, 32(3):316–325, 1992. ISSN 09151559. doi: 10.2355/isijinternational.32.316.
- [56] D. P. Koistinen and R. E. Marburger. A general equation prescribing the extent of the austenite-martensite transformation in pure iron-carbon alloys and plain carbon steels. *Acta Metallurgica*, 7(1):59–60, 1959. ISSN 00016160. doi: 10.1016/0001-6160(59)90170-1.



- [57] C. H. Gür and J. Pan. *Handbook of Thermal Process Modelling*. CRC Press, Boca Raton, 2009. ISBN 9780849350191.
- [58] M. Lusk, G. Krauss, and H.-J. Jou. A Balance Principle Approach for Modeling Phase Transformation Kinetics. *Le Journal de Physique IV*, 05(C8):C8-279-C8-284, 1995. ISSN 1155-4339. doi: 10.1051/jp4:1995839.
- [59] R. P. Garrett, S. Xu, J. Lin, and T. A. Dean. A model for predicting austenite to bainite phase transformation in producing dual phase steels. *International Journal of Machine Tools and Manufacture*, 44(7-8):831-837, 2004. ISSN 08906955. doi: 10.1016/j.ijmachtools.2004.01.004.
- [60] I. Busic. *Abschrecksimulation von Stahlrohren*. Diploma thesis, Montanuniversitaet Leoben, 2010.
- [61] A. Epishin, T. Link, U. Bruckner, B. Fedelich, and P. Portella. Effects of Segregation in Nickel-Base Superalloys: Dendritic Stresses. In *Superalloys 2004 (Tenth International Symposium)*, pages 537-543. TMS, 2004. ISBN 0-87339-576-X. doi: 10.7449/2004/Superalloys.2004.537-543. URL <http://www.tms.org/Superalloys/10.7449/2004/Superalloys{ }2004{ }537{ }543.pdf>.
- [62] T. Siwecki, T. Koziel, W. B. Hutchinson, and P. Hansson. Effect of Micro-Segregation on Phase Transformation and Residual Stress. *Materials Science Forum*, 539-543:4596-4601, mar 2007. ISSN 1662-9752. doi: 10.4028/www.scientific.net/MSF.539-543.4596. URL <http://www.tms.org/Superalloys/10.7449/2004/Superalloys{ }2004{ }537{ }543.pdf><https://www.scientific.net/MSF.539-543.4596>.
- [63] C. Hsueh and P. F. Becher. Residual thermal stresses in ceramic composites. Part I: with ellipsoidal inclusions. *Materials Science and Engineering: A*, 212(1):22-28, jul 1996. ISSN 09215093. doi: 10.1016/0921-5093(96)10176-3. URL <https://linkinghub.elsevier.com/retrieve/pii/0921509396101763>.
- [64] Dassault Systems. Abaqus standard. URL <https://www.3ds.com/products-services/simulia/products/abaqus/abaqusstandard/>.
- [65] Sente Software Ltd. Jmatpro. URL <https://www.sentesoftware.co.uk/jmatpro>.
- [66] R. Mahnken, A. Schneidt, S. Tschumak, and H. J. Maier. On the simulation of austenite to bainite phase transformation. *Computational Materials Science*, 50(6):1823-1829, 2011. ISSN 09270256. doi:

- 10.1016/j.commatsci.2010.12.032. URL <http://dx.doi.org/10.1016/j.commatsci.2010.12.032>.
- [67] J. Wendelstorf, K. H. Spitzer, and R. Wendelstorf. Spray water cooling heat transfer at high temperatures and liquid mass fluxes. *International Journal of Heat and Mass Transfer*, 51(19-20):4902–4910, 2008. ISSN 00179310. doi: 10.1016/j.ijheatmasstransfer.2008.01.032.
- [68] R. Viscorova, R. Scholz, K. H. Spitzer, and J. Wendelstorf. Spray water cooling heat transfer under oxide scale formation conditions. *WIT Transactions on Engineering Sciences*, 53:163–172, 2006. ISSN 17433533. doi: 10.2495/HT060161.
- [69] J. M. Moyer and G. S. Ansell. The volume expansion accompanying the martensite transformation in iron-carbon alloys. *Metalurgical Transactions A*, 6(9):1785–1791, sep 1975. ISSN 0360-2133. doi: 10.1007/BF02642308. URL <http://link.springer.com/10.1007/BF02642308>.
- [70] T. Mura. *Micromechanics of defects in solids*. Springer Netherlands, Dordrecht, 1982. ISBN 978-94-011-8548-6. doi: 10.1007/978-94-011-9306-1. URL <http://link.springer.com/10.1007/978-94-011-9306-1>.
- [71] K. Prabitz. Beurteilung des Gefährdungspotentials von Porenbildung in Polymeren beim Einbetten elektronischer Komponenten in der Medizintechnik, 2017.
- [72] M. Avrami. Kinetics of phase change. I: General theory. *The Journal of Chemical Physics*, 7(12):1103–1112, 1939. ISSN 00219606. doi: 10.1063/1.1750380.
- [73] J.W. Cahn. Transformation kinetics during continuous cooling. *Acta Metallurgica*, 4(6):572–575, 1956. ISSN 00016160. doi: 10.1016/0001-6160(56)90158-4.
- [74] J. B. Leblond, J. Devaux, and J. C. Devaux. Mathematical modelling of transformation plasticity in steels I: Case of ideal-plastic phases. *International Journal of Plasticity*, 5(6):551–572, 1989. ISSN 07496419. doi: 10.1016/0749-6419(89)90001-6.

## Chapter 2

# Publication 1

*Residual stress and microstructure evolution in  
steel tubes for different cooling conditions  
- Simulation and verification*

The following chapter is reprinted here with identical content as in [1] published in

*Materials Science & Engineering A* 747 (2019) 73–79  
DOI: 10.1016/j.msea.2019.01.037

submitted 13 December 2018, accepted 9 January 2019,  
available online 11 January 2019

The format and style has been adapted to the general style of this monograph.

*Residual stress and microstructure evolution in  
steel tubes for different cooling conditions  
- Simulation and verification*

**Authors**

Silvia Brunbauer<sup>1\*</sup>, Gerald Winter<sup>2</sup>, Thomas Antretter<sup>3</sup>, Peter Staron<sup>4</sup>,  
Werner Ecker<sup>1</sup>

<sup>1</sup>Materials Center Leoben Forschung GmbH, Roseggerstraße 12,  
Leoben, Austria

<sup>2</sup>voestalpine Tubulars GmbH & Co KG, Alpinestrasse 17,  
Kindberg-Aumuehl, Austria

<sup>3</sup>Institute of Mechanics, Montanuniversitaet Leoben, Franz Josef Strasse  
18,  
Leoben, Austria

<sup>4</sup>Institut für Werkstofforschung, Helmholtz-Zentrum Geesthacht, Max  
Planck-Straße 1, Geesthacht, Deutschland

\*corresponding author: [silvia.brunbauer@mcl.at](mailto:silvia.brunbauer@mcl.at)

*Keywords*

Simulation; Residual Stresses; Phase Transformation; Quenching; Steel;  
Heat Treatment

## 2.1 Abstract

A finite element modelling approach is applied to investigate the evolution of residual stresses, temperature and phase fraction during quenching of low-alloyed seamless steel tubes. Under real-process quenching conditions, non-continuous cooling occurs that results in a stopping and restarting transformation front throughout the tube's radial direction. It is shown that the simulated temperature history, transformation kinetics and the residual stresses from the thermo-mechanical model can be correlated with experimentally observed residual stresses and micro-hardness investigations of produced tubes. The effect of the discontinuous cooling was found to be negligible with respect to residual stresses for comparable conditions, but it can cause local self-annealing and micro-hardness drops. The combination of outer and inner cooling of the tube influences residual stress and micro-hardness distribution significantly.

## 2.2 Introduction

Quantitative knowledge of residual stresses and their distribution in steel products is essential to guarantee their quality and safety in use. Several ways to calculate residual stresses in components are documented in literature, ranging from analytical solutions to frameworks for finite element (FE) based model approaches. A detailed literature review on the theoretical framework for implementing phase transformation in residual stress calculations was given by Rohde and Jeppsson in 2000 [2]. In 2008, Simsir and Gür published a FE method based framework for steel quenching simulations [3] and later investigated the effects of asymmetrical specimen geometries on residual stress distributions [4]. A similar framework was used to simulate the influence of size effects during quenching of steel cylinders by Schemmel and coworkers [5] in a FE model. In the recent past, the focus of modelling residual stresses with simulation methods also included microstructural influences such as crystallographic orientation on the occurring transformation-induced plasticity (TRIP) [6] as well as the influence of asymmetric cooling conditions on hot rolled plates [7]. Many industrial quenching processes use a cooling setup that can cause non-continuous cooling and thus discontinuously progressing phase transformation. In this paper, the effect of non-continuous cooling conditions on residual stresses and phase transformation in seamless steel tubes is presented. This involves discussing the effects of a stepwise propagating phase transformation front and the effects of plasticity and transformation-induced plasticity on the resulting stress state. The stepwise propagation of phase transformation appears, because during the quenching procedure the tubes are cooled by moving through a spray water cooling line, which consists of several cooling

baskets. Near each basket the cooling efficiency is high, while between two baskets the heat flux is lower and the warmer regions near the inner diameter reheat the outer area. To investigate the residual stress evolution under the non-continuous cooling conditions of the spray water quench, depending on the tube dimension and the cooling speed, a simulation framework is implemented in the FE program ABAQUS. User subroutines are used to account for phase transformations, cooling conditions and material properties. The simulation results are compared to online temperature measurements to verify the thermal model boundary conditions. For the comparison of the residual stress simulation results with the real process, tubes of two different dimensions were produced, and after manufacturing, a slice was cut off to perform stress measurements on it. The evolving residual stresses were calculated by means of a consecutive analysis of three problems: (i) the time dependent temperature profile controlled by the austenitization temperatures and cooling system; (ii) the evolving solid-state transformations during accelerated cooling, which serves as input for (iii) the residual stress evolution during phase transformation.

## 2.3 Methods

The following section describes the process, the model and the included theory in detail.

### 2.3.1 Process description

The investigated quenching process is part of a quenching and tempering procedure. During quenching, the tube is cooled very rapidly from austenitization temperature to about 60°C. The austenitization aims at homogenizing the material after the rolling process and the subsequent rapid cooling gives a fully martensitic microstructure with high strength. To achieve this kind of microstructure the tube is transported to a water-quenching system, where it is cooled while it moves through eight cooling baskets with spray water nozzles, see Fig. 2.1. Depending on their dimensions different cooling routes are chosen for the tubes; the dimension 178x12.65mm is cooled only by the cooling baskets, whereas the dimension 200x22.65mm is additionally cooled by a lance that also applies water from the inside. Fig. 2.1 depicts the schematic time temperature profile during quenching and tempering (QT) process and the cooling equipment.

### 2.3.2 Model description

The following section gives a description of the model that combines the thermal boundary conditions, the solid-state phase transformation model and the necessary input data for the stress simulation.

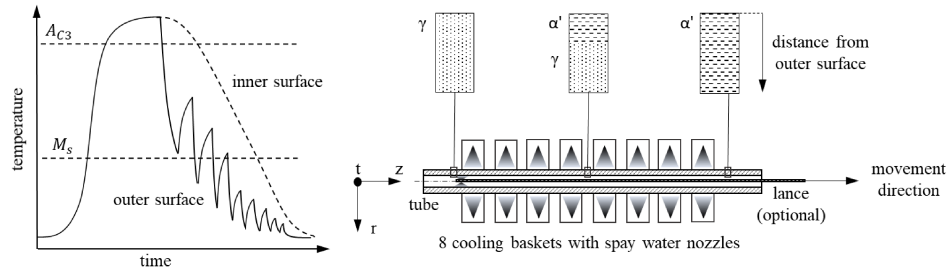


**Figure 2.1:** Left: Schematic time-temperature diagram of austenitizing and quenching process. Right: Schematic representation of the quenching setup.

### Thermal and mechanical boundary conditions

Thermal boundary conditions are a simplified representation of the real process conditions. While in reality, the cooling baskets are immobile and the tube moves through them, it is computationally more efficient to solve the inverse problem, i.e., the pipe is fixed and temperature sinks move along the surface, see Fig. 2.2. Because of symmetry, only a slice of the tube is modeled which is admissible since temperature gradients in  $z$ -direction can be neglected. Since the tube is free to rotate during cooling around its direct axis, the cooling conditions within one basket can be assumed as homogeneous in tangential direction. The thermal transition condition is applied using an ABAQUS user defined subroutine, where an if-condition toggles between the heat transfer coefficient for steel to water and for steel to air. The heat transfer coefficient is embedded based on the work of Wendelsdorf [8] and Viscorova [9] who provide an analytical fit based on measurement data for a temperature and water amount dependent heat transfer coefficient for spray water cooling. During accelerated cooling residual stresses can be induced by large temperature gradients and by transformation from austenite to martensite on the surface. The stresses result from the different occurring strains during cooling: the thermal strains, the volume strains by the change of the crystal lattice, the transformation-induced plastic strains in addition to elastic and plastic strains. The stresses are calculated by correlating these strains with the elastic and plastic material properties for the occurring phase fraction combination. For the boundary conditions in  $z$ -direction (see Fig. 2.2) it is assumed that the tubes' cross sections remain plane and normal to the  $z$ -axis. However, the displacement in  $z$ -direction is unconstrained. In the  $r$ - $z$  plane axisymmetric conditions apply for both the temperature and the stress field. This assumption is valid as long as the cooling conditions can be considered uniform in tangential direction. The problem at hand can be treated as weakly coupled, i.e., the thermal problem is calculated first providing the input for the subsequent mechanical

analysis. For the investigated material, experiments show that the stress influence on the transformation start temperature for martensite and bainite is negligible. This implies that the stress field does not affect the phase transformation and thus the temperature field. Consequently, the mechanical calculation can be performed subsequent to the thermal calculation in a “weakly coupled” manner.

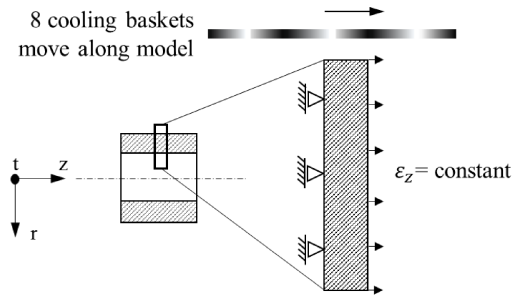


**Figure 2.2:** Schematic depiction of the model boundary conditions in an axisymmetric generalized plane strain model.

### Phase transformation model

The phase transformation model combines four main aspects: The transformation kinetics; the strains that are caused by phase transformation and thermal expansion; transformation-induced plasticity (TRIP); and latent heat. The transformation kinetics model is adapted to dilatometer data for a range of cooling conditions not only limited to quenching conditions. This is to enable future process variations and include not only the transformation from austenite to martensite but also to bainite. For the diffusionless solid-state phase transformation from austenite to martensite the Koistinen and Marburger kinetics model is chosen [10, 11]. The diffusion controlled phase transformations is modeled according to Garrett [10] and Mahnken [12]. The necessary model parameters are adapted using a python routine for optimization. The routine takes the time dependent temperature measurements from the dilatometer at different cooling conditions as input and calculates the phase fractions for the given cooling conditions based on optimized transformation kinetic parameters and dilatation based on thermal expansion and transformation strains of the individual phases. Then the calculated strains are compared with the measured strains and the parameters are adopted accordingly. A framework for the implementation of thermal strains, transformation strains and latent heat as a function of phase fraction and formation rate is used according to literature [2, 4, 13, 14, 15]. The thermal properties such as thermal expansion, thermal conductivity, specific heat as well as the mechanical properties like elastic modulus, Poisson ratio



and yield stress, generally referred to as property  $P_k$ , are linearly weighted by phase fractions  $z_k$  for  $k = 0 \dots N$  phases by

$$P(T, z_k) = \sum_{k=0}^N P_k z_k, \quad (2.1)$$

where  $k = 0$  denotes the parent phase and nonzero  $k$  the product phases. The transformation strains  $\varepsilon_{ij}^{TR}$  for martensite and bainite is given by

$$\varepsilon_{ij}^{TR} = \delta_{ij} \sum_{k=10}^N \beta_k(T) \dot{z}_k, \quad (2.2)$$

where  $\delta_{ij}$  is the identity tensor,  $\beta_k(T)$  denotes the temperature dependent uniaxial transformation strain and  $\dot{z}_k$  the formation rate. The latent heat of the transformations,  $Q^{TR}(\dot{z}_k)$ , is the enthalpy  $\Delta H_k$  times the formation rate of phase  $k$ ,

$$Q^{TR}(\dot{z}_k) = \Delta H_k \dot{z}_k. \quad (k = 1 \dots N) \quad (2.3)$$

The transformation-induced TRIP strains are implemented following Greenwood and Johnson [16] and are implemented in the FE program using a modified Leblond's [17] formulation:

$$\varepsilon_{ij}^{TRIP} = \frac{3}{2} K_k S_{ij} f'(z_1 \dots z_N) \dot{z}_k \quad (2.4)$$

Where  $z_k$  denotes the transformed fraction of product phase  $k$  and the function  $f'(z_1 \dots z_N)$  makes sure that the corresponding TRIP strain saturates when the parent phase has been consumed by  $1 \dots N$  product phases:

$$f'(z_1 \dots z_N) = 2 \left( 1 - \sum_{i=1}^N z_i \right). \quad (2.5)$$

The calculations were performed in the finite element simulation program ABAQUS using DCAX4 and CAX4 elements for the thermal and mechanical calculation step with a size of 0.12x0.12mm.

### Simulation input data

The investigated material is a micro-alloyed high strength steel with 0.3 wt% carbon. To describe the thermal conductivity  $\lambda$ , specific heat  $c_p$ , Young's modulus  $E$  and Poisson ratio  $\nu$  data from JMatPro calculations for the individual phases (austenite and martensite) are used as input data. The data for the phases are combined according to the phase fractions calculated from the phase transformation kinetic model, see equation (2.1). Table 2.1 and table 2.2 give the temperature dependent input data for austenite and martensite.

**Table 2.1:** With JMatPro calculated temperature dependent thermo-physical and elastic properties of austenite.

$T(K)$	$\lambda(W/mK)$	$c_p(J/kgK)$	$\rho(kg/m^3)$	$E(MPa)$	$\nu(-)$
25	17.01	450	—	198560	0.294
300	20.37	513	—	174000	0.311
600	23.93	595	—	146550	0.328
900	27.48	618	7542	117890	0.346

**Table 2.2:** With JMatPro calculated temperature dependent thermo-physical and elastic properties of martensite.

$T(K)$	$\lambda(W/mK)$	$c_p(J/kgK)$	$\rho(kg/m^3)$	$E(MPa)$	$\nu(-)$
25	38.22	445	7837	210450	0.296
200	40.52	561	—	192840	0.302
400	38.64	615	—	157690	0.313

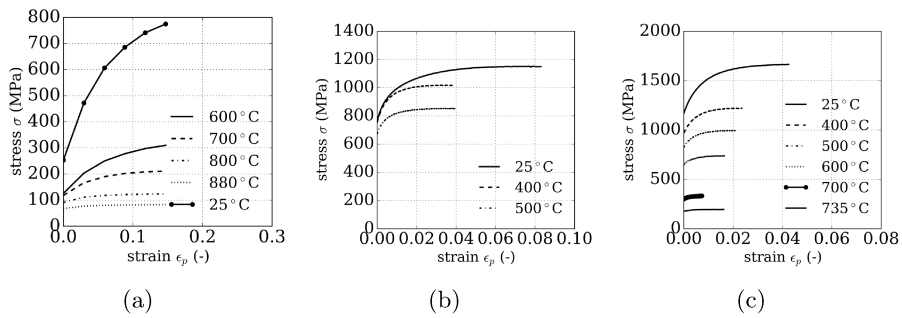


**Figure 2.3:** Flow curves at different temperatures from tensile tests for austenite (a), bainite (b) and martensite (c). The flow curve for austenite (a) at 25°C is extrapolated.

**Table 2.3:** Model parameters for the bainite phase transformation following [18]:

$A_5$	$\Theta^*$	$B_1$	$n$	$\gamma$	$A_1/Q^*$	$A_3$	$\Theta_0$	$\alpha_{2u}$	$B_u$
(-)	(°K)	(°K)	(-)	(-)	(-)	(-)	(°K)	(s <sup>-</sup> )	(°K)
7.23	710	40	16	1.005	10.85	3.5e-5	850	7.23	150

The plastic material data for austenite, martensite and bainite were obtained in tensile tests at elevated temperature (see Fig. 2.3).

The parameters for the Koistinen and Marburger kinetic were optimized as follows:  $\alpha_M = 0.021$  and  $M_s = 370^\circ\text{C}$ . The bainite phase transformation kinetic was implemented following the work of Garrett [9] and Mahnken [11] and the parameters are presented in Table 2.3.

The Greenwood and Johnson parameter for the martensite phase transformation was experimentally determined to be  $K_M = 8.96\text{e-}5$  (MPa<sup>-1</sup>) and for the bainite phase transformation  $K_B = 8.83\text{e-}5$  (MPa<sup>-1</sup>).

## 2.4 Measurements

The plastic material data were experimentally obtained for austenite, martensite and bainite in thermo-mechanical material tests on cylindrical specimens with a narrowed gauge length that were cut from the tube. The used test equipment was a universal testing machine Instron 8803 with a vacuum heating chamber, a load cell U10M with maximum 250 kN from HBM and a laser extensometer by the company Fiedler Optoelektronik GmbH model P-2S-50. An additional heat treatment according to CCT diagrams was applied to achieve specimens of min 95% pure phases. Temperature measurements on a test tube during quenching are performed using a high-temperature data acquisition tool during quenching that detects data from thermocouples. The thermocouples are fixed by a ceramic bond on the outer surface of the tube. The hardness H 0.2 is tested on a Buehler micro hardness tester. The high-energy X-ray diffraction residual stress measurements were performed at the beamline P07 of Helmholtz-Zentrum Geesthacht, located at the PETRA III synchrotron source of DESY, Hamburg. Rings of 10 mm thickness were cut from manufactured tubes and the stresses in radial and tangential direction were measured with an energy of 87 keV and using conical slits evaluating the 211 bcc peak. The Greenwood and Johnson parameter was measured following the work of Neubert and coworkers [19].

## 2.5 Results

In this section, the validation of the heat transfer coefficient for the tube production line is presented and compared with simulation results. The

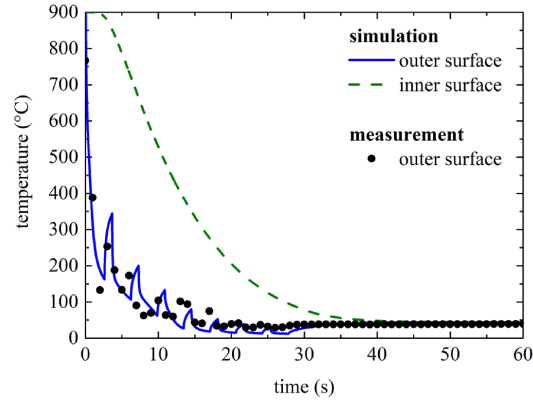


**Figure 2.4:** Comparing temperature online measurements with simulation results for a test-tube.

simulation of a fictitious production case is shown to point out the difference in residual stress distribution with and without discontinuous cooling. Followed by temperature profiles and phase fraction evolution for two manufactured tubes and the comparison of resulting residual stress distributions with measurements.

First, simulation data are compared with temperature measurements. The online-process measurement is performed on a test tube of similar chemical composition, which is equipped with thermocouples. Unlike in realistic process cooling conditions the annealing temperature has been set to  $900^{\circ}\text{C}$  rather than  $880^{\circ}\text{C}$ . The calculated temperature on the outer surface of the tube show rapid cooling every time one of the eight cooling baskets passes. Between two cooling baskets, there is a cooling stop and the outer material points are re-heated by the warmer material from the interior of the tube's wall. The agreement of the calculated profiles and the achieved end temperature at cooling stop indicate that the heat transfer coefficient calculated by a water amount and temperature dependent fit of the Nukiyama curve [8] are appropriate for this heat transfer dominated problem on the outer surface, see Fig. 2.4.

Secondly, after verifying the heat transfer coefficient with the test tube, the simulation results for continuous cooling conditions are discussed. This is to understand the differences in residual stress distribution after continuous and discontinuous cooling followed by the comparison of time and spatially resolved results for the two real process dimensions with discontinuous cooling. The section consist of the following cases: (1) A model case with continuous cooling for the dimension of 177.8 mm outer diameter and 12.65 mm wall thickness (this dimension is now referred to as dimension 1). (2) Cooling of dimension 1 with real process discontinuous cooling con-

ditions. (3) Cooling of dimension with 200 mm outer diameter and 22.65 mm wall thickness, referred to as dimension 2, with real process and thus discontinuous cooling condition. Both real process simulations (case 2 and case 3) are compared with residual stress and hardness measurements.

Next, the calculated inner and outer surface temperature for the model case with continuous cooling of dimension 1 are shown in Fig. 2.5a. The continuous cooling is accomplished by fully cooling the tube with the first cooling basket. This leads to a complete martensitic transformation without interruption. The temperature on the inner surface is time delayed due to the thermal conductivity. When the temperature in the two points falls below the martensite start temperature  $M_s$  the transformation starts, as can be seen in Fig. 2.5b. The transformation is accompanied by a volume change and the TRIP effect. The evolution of the different strain contributions in tangential direction is depicted in Fig. 2.5c. The total tangential strain  $\varepsilon_t$  is split up into its components: an elastic component  $\varepsilon_t^{el}$ ; a component  $\varepsilon_t^{th+vol}$  that accounts for thermal expansion  $\varepsilon_t^{th}$  and volume expansion  $\varepsilon_t^{vol}$ ; and a component  $\varepsilon_t^{p+trip}$  that accounts for the sum of classical plasticity  $\varepsilon_t^p$  due to thermal misfits and TRIP  $\varepsilon_t^{trip}$ .

The component  $\varepsilon_t^{el}$  denotes the elastic strain contribution in tangential direction. It can be seen that the elastic contribution is small compared to  $\varepsilon_t^{p+trip}$ . Before the phase transformation during cooling from the annealing temperature to  $M_s$ , the plastic strain  $\varepsilon_t^p$  is positive for point 1 on the outer surface and negative for point 2 on the inner surface due to the thermal misfit. When the transformation starts the TRIP contribution leads to decreasing  $\varepsilon_t^{p+trip}$ . This is because the stress state changes from tensile to compressive regime due to the volume expansion in the transforming region, see Fig. 2.5d, and according to equation (4) this leads to a negative TRIP strain.

When the transformation has finished in point 2, see in Fig. 2.5b at 21 s, the difference in the stresses at point 1 and point 2 is small compared to the difference at 40 s, see Fig. 2.5d. This is due to the thermal expansion. Since transformation finishes at the inner point 1 at about 200°C while point 2 is already cooled to 20°C an additional change in stresses is visible in Fig. 2.5d, when transformation has already stopped.

The resulting residual stress distribution for continuous cooling, the plastic strain  $\varepsilon_t^p$  and the transformation-induced plasticity  $\varepsilon_t^{trip}$  are depicted in Fig. 2.6.

Fig. 2.6 shows that the contribution of transformation-induced plasticity  $\varepsilon_t^{trip}$  is small compared to plasticity  $\varepsilon_t^p$  caused by stresses due to thermal and volume expansion. It shows that after the tube is cooled to ambient temperature, the plastic strain near the inner surface of the tube increases again because this austenitic region has to balance compressive stresses from already transformed martensite as the phase transformation continues from the outer to the inner surface. Before the phase transformation starts, the

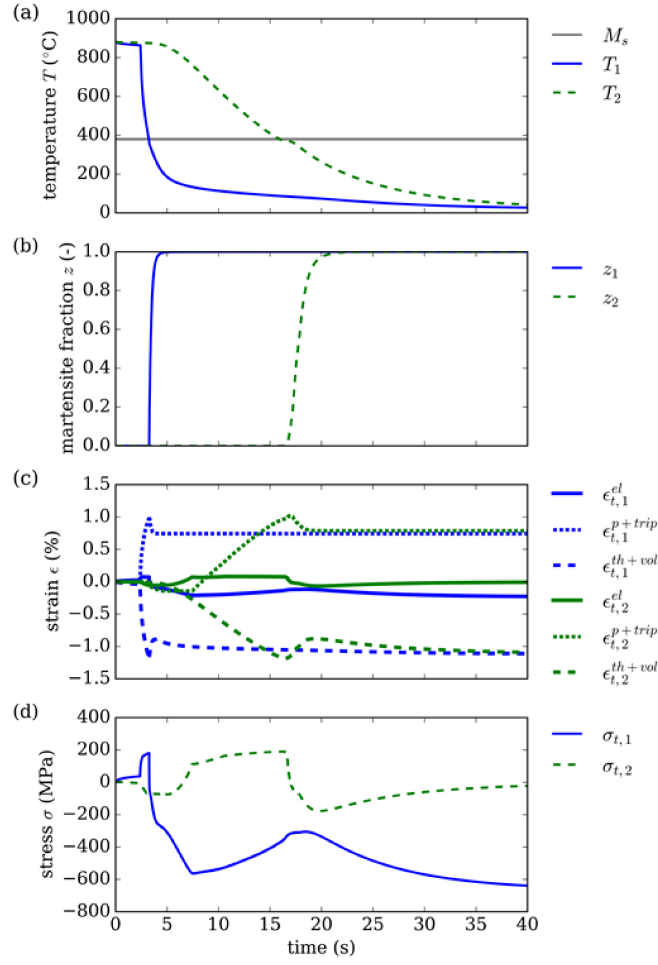


**Figure 2.5:** Diagram showing simulation results for continuous cooling. Point 1 on the outer surface, point 2 on the inner surface. (a) the temperature  $T$ , (b) the phase fraction  $z$ , (c) the strain contributions  $\epsilon_t^{el}$ ,  $\epsilon_t^{p+trip}$  and  $\epsilon_t^{th+vol}$  in tangential direction and (d) the stress  $\sigma$  in tangential direction over time.

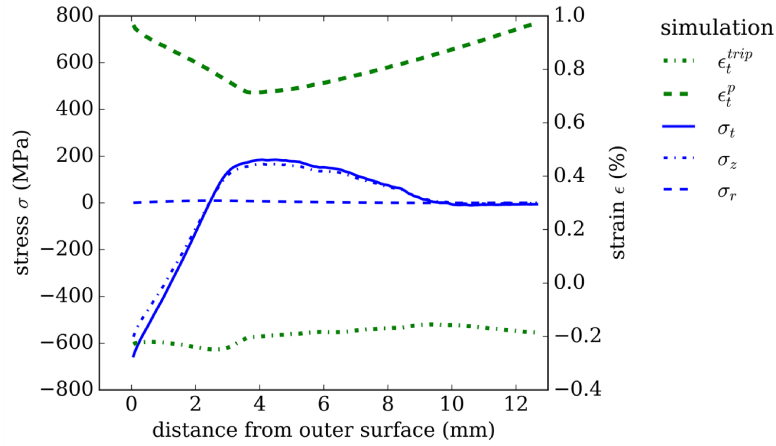


**Figure 2.6:** Simulation results for continuous cooling: residual stresses and plastic strains in tangential direction as a function of distance from outer surface at the end of quenching for the dimension 177.8x12.65mm (dimension 1).

outer surface must be cooled to  $M_s$  temperature, which causes positive plastic strains in the region near the outer surface and negative plastic strains in the region near the inner surface. The area with the minimum plastic strain  $\epsilon_t^p$  in the middle region of the plot (which is also the middle of the tube's radial direction) corresponds to the position where plastic deformation due to thermal contraction is zero.

The transformation-induced plasticity plays a dominating role in defining the final stress state in the inner region, since most of the transformation happens in the compressive regime. This leads to a negative trip strain that reduces the occurring plastic strains due to phase transformation and changes the relative amount of plastic strain caused by proceeding transformation and by thermal misfit. Since the occurring strains also have to satisfy the axial symmetric boundary condition, the total tangential strain is given by

$$\epsilon_t = \frac{u_r}{r} \quad (2.6)$$

The effect of the discontinuous process conditions is discussed in comparison to the continuous cooling case. Starting with dimension 1, the temperature evolution over time is shown in Fig. 2.7a. On the outer surface, the temperature decreases with each cooling basket interrupted by a re-heating process in between. This results from the gap between two adjacent baskets, where no spray water is applied represented in the model by a lower heat transfer coefficient. It is found that the outer surface is reheated several times by the still warmer inner material during quenching. The points 1–7 mark the end of every reheating interval. The comparison with Fig. 2.7b

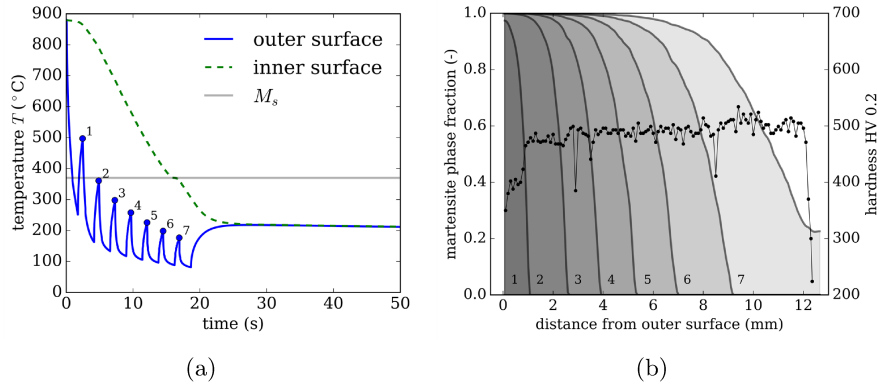


**Figure 2.7:** (a) Diagram showing the calculated temperature over time for the inner and outer surface. The blue dots mark the times where the phase fraction distribution is plotted in (b): diagram showing martensite phase fraction distribution and micro-hardness measurements over distance from outer surface for 177.8x12.65mm for discontinuous quenching conditions (dimension 1).

reveals, that the discontinuous cooling on the surface leads to a stepwise propagation of the martensitic phase transformation. The grey colored areas represent the distribution of transformed martensite as a function of the distance from the outer surface at the end of each re-heating section. Comparing the simulation results with micro-hardness measurements reveals that the re-heating of the individual sections causes a slight drop in hardness. This might be caused by self-annealing effects and confirm the stepwise simulation results.

The resulting residual stress distribution is shown in Fig. 2.8 and looks similar to the continuous case shown in Fig. 2.6. This reveals that discontinuous cooling has little effect on the resulting residual stress distribution for comparable conditions. The final distribution is rather determined by plasticity  $\varepsilon^p$  caused by thermal misfits and TRIP  $\varepsilon^{trip}$ . Comparing the TRIP strain  $\varepsilon^{trip}$  in Fig. 2.6 to Fig. 2.8 reveals that the discontinuous cooling is reflected in the locally varying TRIP strain. In the discontinuous case,  $\varepsilon^{trip}$  shows local kinks at positions where the transformation front has stopped. Plastic and TRIP strain compensate each other at these points, which reduces deviations in the resulting residual stress distribution.

Dimension 2 requires internal cooling due to the higher wall thickness. The calculated temperature profiles for dimension 2 over time are depicted for the outer and inner surface in Fig. 2.9. The results show that the internal cooling causes a rapid temperature drop on the inner surface followed by a re-heating by the inner areas (see the dashed green line). The comparison of the martensite distribution and the marked times at the end of re-heating



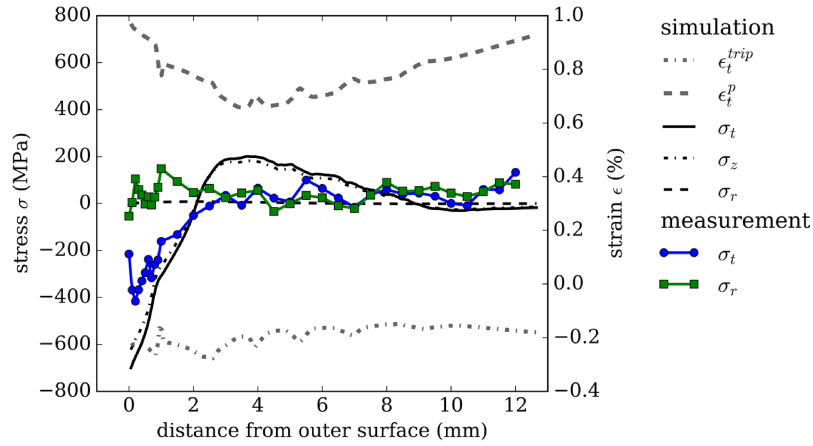


**Figure 2.8:** Simulation results for discontinuous cooling: residual stresses and plastic strains compared with the high-energy X-ray diffraction measurement results as a function of distance from outer surface at the end of quenching for the dimension 177.8x12.65mm (dimension 1).

section show again a correlation with hardness measurements. Additionally the hardness measurements reveal that the martensite transformed by the cooling of the inner quench (IQ) shows a greater drop in hardness. This is because the region near the inner surface is self-annealed at almost 650°C, i.e., a higher self-annealing temperature compared to the outer regions.

The resulting residual stress distribution of dimension 2 with internal and external cooling is shown in Fig. 2.10. The outer area is in a compressive stress state after quenching, while the inner area is under tension. The tensile stresses on the inner surface are caused by the internal cooling. When internal cooling is applied additionally to the external cooling, phase transformation starts from both surfaces simultaneously. By contrast, at the end of the inner cooling, the phase transformation progresses only from the outer side, and thus causes the anti-symmetric stress distribution. This becomes more evident as the simulation of dimension 2 without internal cooling shows a similar stress distribution as dimension 1 without the pronounced tensile peak on the inner surface. However, without internal cooling bainite transformation is promoted due to the slower cooling rates.

## 2.6 Conclusions

Simulation of non-continuous cooling of a tube manufacturing process allows correlating the temperature history and phase evolution with micro hardness measurements in the tube. Understanding and reducing residual stresses and their evolution in complex cooling processes is the first step for focused

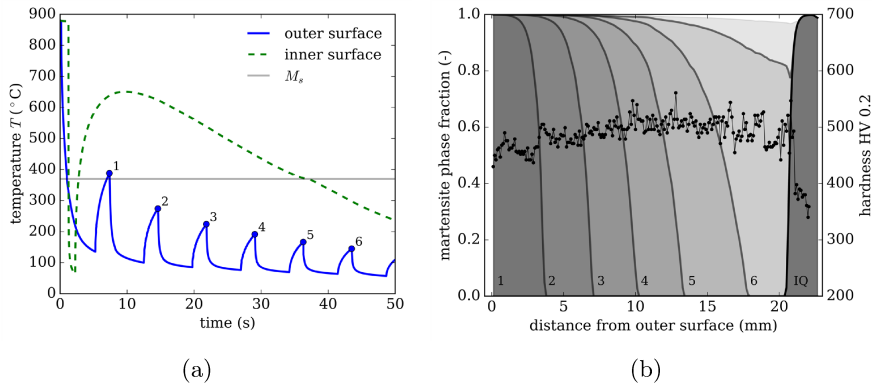


**Figure 2.9:** (a) Diagram showing the calculated temperature over time for the inner and outer surface and. (b) diagram showing martensite phase fraction and microhardness measurements over distance form outer surface for 200x22.65mm (dimension 2) for discontinuous conditions with internal and external cooling.

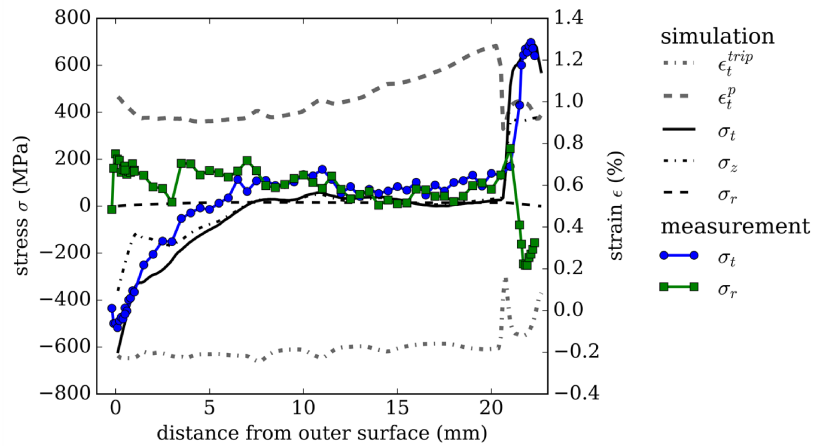


**Figure 2.10:** Diagram showing the simulation results for the residual stresses and plastic strains compared with the high-energy X-ray diffraction measurement results as a function of distance from outer surface at the end of quenching for the dimension 200x22.65mm (dimension 2) for discontinuous conditions with internal and external cooling.

residual stress design for best product performance and operating conditions. The main conclusions are:

- The non-continuous cooling leads to a combination of cooling and re-heating phases in the tubes' radial direction, which in turn gives a stepwise martensite formation, confirmed by hardness measurements, and causes local self-annealing.
- Detailed analysis of time and spatially resolved simulation results allow the understanding of residual stress evolution.
- The residual stress distribution is strongly dominated by plasticity due to thermal misfits. The transformation-induced plasticity plays an important role, since it counteracts the classical plasticity and shifts stresses near the inner surface to values close to zero.
- The effect of the discontinuous cooling was found to be negligible with respect to residual stresses, but it can cause local self-annealing and micro-hardness drops.
- A basic Koistinen and Marburger phase transformation model considering temperature dependent transformation strains and transformation-induced plasticity yields good qualitative agreement with residual stress measurements. Further model improvements might consider a non-homogeneous austenite grain size distribution before quenching and decarburization effects on the surface.

**Acknowledgments** The authors gratefully acknowledge the financial support under the scope of the COMET program within the K2 Center “Integrated Computational Material, Process and Product Engineering (IC-MPPE)” (Project No 859480). This program is supported by the Austrian Federal Ministries for Transport, Innovation and Technology (BMVIT) and for Digital and Economic Affairs (BMDW), represented by the Austrian research funding association (FFG), and the federal states of Styria, Upper Austria and Tyrol.

**Data availability** The raw/processed data required to reproduce these findings cannot be shared at this time as the data also forms part of an ongoing study.

# Bibliography

- [1] S. Brunbauer, G. Winter, T. Antretter, P. Staron, and W. Ecker. Residual stress and microstructure evolution in steel tubes for different cooling conditions – Simulation and verification. *Materials Science and Engineering A*, 747:73–79, 2019. ISSN 09215093. doi: 10.1016/j.msea.2019.01.037. URL <https://doi.org/10.1016/j.msea.2019.01.037>.
- [2] J. Rohde and A. Jeppsson. Literature review of heat treatment simulations with respect to phase transformation, residual stresses and distortion. *Scandinavian Journal of Metallurgy*, 29(2):47–62, 2000. ISSN 03710459. doi: 10.1034/j.1600-0692.2000.d01-6.x.
- [3] C. Şimşir and C. H. Gür. A FEM based framework for simulation of thermal treatments: Application to steel quenching. *Computational Materials Science*, 44(2):588–600, 2008. ISSN 09270256. doi: 10.1016/j.commatsci.2008.04.021.
- [4] C. Şimşir and C. H. Gür. 3D FEM simulation of steel quenching and investigation of the effect of asymmetric geometry on residual stress distribution. *Journal of Materials Processing Technology*, 207(1-3):211–221, 2008. ISSN 09240136. doi: 10.1016/j.jmatprotec.2007.12.074.
- [5] M. Schemmel, P. Prevedel, R. Schöngrundner, W. Ecker, and T. Antretter. Size effects in residual stress formation during quenching of cylinders made of hot-work tool steel. *Advances in Materials Science and Engineering*, 2015, 2015. ISSN 16878442. doi: 10.1155/2015/678056.
- [6] L. Pan, W. He, and B. Gu. Effect of crystallographic orientation on quenching stress during martensitic phase transformation of carbon steel plate. *Journal Wuhan University of Technology, Materials Science Edition*, 32(5):1213–1219, 2017. ISSN 19930437. doi: 10.1007/s11595-017-1733-4.
- [7] J. Wang, G. Niu, Z. Yang, H. Cao, and C. Liu. Influence of Cooling Intensity Difference Between Upper and Lower Surface to the Residual Stress Distribution of 7050 Aluminum

- Alloy Plates. In *High Performance Structural Materials*, pages 221–233. Springer Singapore, Singapore, 2018. ISBN 9789811301049. doi: 10.1007/978-981-13-0104-9\_24. URL [http://dx.doi.org/10.1007/978-981-13-0104-9\\_{\\_}24](http://dx.doi.org/10.1007/978-981-13-0104-9_{_}24)[http://link.springer.com/10.1007/978-981-13-0104-9\\_{\\_}24](http://link.springer.com/10.1007/978-981-13-0104-9_{_}24).
- [8] J. Wendelstorf, K. H. Spitzer, and R. Wendelstorf. Spray water cooling heat transfer at high temperatures and liquid mass fluxes. *International Journal of Heat and Mass Transfer*, 51(19-20):4902–4910, 2008. ISSN 00179310. doi: 10.1016/j.ijheatmasstransfer.2008.01.032.
- [9] R. Viscorova, R. Scholz, K. H. Spitzer, and J. Wendelstorf. Spray water cooling heat transfer under oxide scale formation conditions. *WIT Transactions on Engineering Sciences*, 53:163–172, 2006. ISSN 17433533. doi: 10.2495/HT060161.
- [10] R. P. Garrett, S. Xu, J. Lin, and T. A. Dean. A model for predicting austenite to bainite phase transformation in producing dual phase steels. *International Journal of Machine Tools and Manufacture*, 44(7-8):831–837, 2004. ISSN 08906955. doi: 10.1016/j.ijmachtools.2004.01.004.
- [11] D. P. Koistinen and R. E. Marburger. A general equation prescribing the extent of the austenite-martensite transformation in pure iron-carbon alloys and plain carbon steels. *Acta Metallurgica*, 7(1):59–60, 1959. ISSN 00016160. doi: 10.1016/0001-6160(59)90170-1.
- [12] R. Mahnken, A. Schneidt, T. Antretter, U. Ehlenbröcker, and M. Wolff. Multi-scale modeling of bainitic phase transformation in multi-variant polycrystalline low alloy steels. *International Journal of Solids and Structures*, 54:156–171, 2015. ISSN 00207683. doi: 10.1016/j.ijsolstr.2014.10.021. URL <http://dx.doi.org/10.1016/j.ijsolstr.2014.10.021>.
- [13] S. Denis, D. Farias, and A. Simon. Mathematical Model Coupling Phase Transformations and Temperature Evolutions in Steels. *ISIJ International*, 32(3):316–325, 1992. ISSN 09151559. doi: 10.2355/isijinternational.32.316.
- [14] F. M. B. Fernandes, S. Denis, and A. Simon. Mathematical model coupling phase transformation and temperature evolution during quenching of steels. *Materials Science and Technology*, 1(10):838–844, oct 1985. ISSN 02670836. doi: 10.1179/026708385790123991. URL <http://openurl.ingenta.com/content/xref?genre=article{&}issn=0267-0836{&}volume=1{&}issue=10{&}spage=838>.

- [15] C. H. Gür and J. Pan. *Handbook of Thermal Process Modelling*. CRC Press, Boca Raton, 2009. ISBN 9780849350191.
- [16] G. W. Greenwood and R. H. Johnson. The deformation of metals under small stresses during phase transformations. *Proceedings of the Royal Society of London. Series A. Mathematical and Physical Sciences*, 283 (1394):403–422, 1965. ISSN 2053-9169. doi: 10.1098/rspa.1965.0029.
- [17] J. B. Leblond, J. Devaux, and J. C. Devaux. Mathematical modelling of transformation plasticity in steels I: Case of ideal-plastic phases. *International Journal of Plasticity*, 5(6):551–572, 1989. ISSN 07496419. doi: 10.1016/0749-6419(89)90001-6.
- [18] R. Mahnken, A. Schneidt, S. Tschumak, and H. J. Maier. On the simulation of austenite to bainite phase transformation. *Computational Materials Science*, 50(6):1823–1829, 2011. ISSN 09270256. doi: 10.1016/j.commatsci.2010.12.032. URL <http://dx.doi.org/10.1016/j.commatsci.2010.12.032>.
- [19] S. Neubert, A. Pittner, and M. Rethmeier. Experimental determination of TRIP-parameter K for mild- and high-strength low-alloy steels and a super martensitic filler material. *SpringerPlus*, 5(1), 2016. ISSN 21931801. doi: 10.1186/s40064-016-2474-0.

## Chapter 3

# Publication 2

### *Model-based residual stress design in multiphase seamless steel tubes*

The following chapter is reprinted here with identical content as in [1] published in

*Materials* 2020, 13(2) 439  
DOI: 10.3390/ma13020439

submitted 15 November 2019, accepted 10 January 2020,  
available online 16 January 2020

The format and style has been adapted to the general style of this monograph.

*Model-based residual stress design in multiphase  
seamless steel tubes*

**Authors**

Silvia Leitner<sup>1\*</sup>, Gerald Winter<sup>2</sup>, Jürgen Klarner<sup>2</sup>, Thomas Antretter<sup>3</sup>,  
Werner Ecker<sup>1</sup>

<sup>1</sup>Materials Center Leoben Forschung GmbH, Roseggerstraße 12,  
Leoben, Austria

<sup>2</sup>voestalpine Tubulars GmbH & Co KG, Alpinestrasse 17,  
Kindberg-Aumuehl, Austria

<sup>3</sup>Institute of Mechanics, Montanuniversitaet Leoben, Franz Josef Strasse  
18,  
Leoben, Austria

\*corresponding author: [silvia.leitner@mcl.at](mailto:silvia.leitner@mcl.at)

*Keywords*

simulation; XRD measurements; design; residual stress; phase trans-  
formation; low-alloyed steel



### 3.1 Abstract

Residual stresses in quenched seamless steel tubes highly depend on the cooling conditions to which the tubes have been subjected. The design aspect of how to use controlled cooling strategies in multiphase steel tubes to achieve certain residual stress and phase configurations is discussed. In an experimentally validated finite element (FE) model considering a coupled evolution of martensite and bainite, three cooling strategies are tested for a low-alloyed 0.25 wt.% C steel tube. The strategies are (i) external cooling only, (ii) internal and external cooling for low residual stresses in a mainly martensitic tube, and (iii) internal and external cooling with low cooling rate for a mainly bainitic tube. The strategies represent design cases, where low residual stresses with different phase compositions are provoked, in order to show the potential of numerical analysis for residual stress and property design. It can be concluded that, for the investigated steel class, intense external cooling leads to a characteristic residual stress profile regardless of the dimension. A combination of external and internal cooling allows a more flexible design of residual stress and phase distribution by choosing different cooling parameters (i.e., water amount and cooling times). In general, lower cooling rates lead to lower thermal misfit strains, and thus less plasticity and lower residual stresses.

### 3.2 Introduction

The novel aspect of this work is to use an experimentally verified multiphase process model and present mechanism-based cooling strategies tailored to specific requirements, such as defined residual stress state and multiphase composition. Residual stresses are nowadays usually calculated using finite element (FE) models. Denis et al. [2] gave a mathematical description on how to couple thermal, mechanical, and metallurgical fields including phase transformation in 1992, which is the essential framework for calculating residual stresses during heat treatment. Rhode and Jeppsson [3] published a detailed literature review on the established models and a comparison of experiment and simulation. A very general overview for numerical modelling for stresses in heat treatment applications can be found in the work of [4].

The effect of manufacturing process and material parameters on residual stresses or distortion considering phase transformation has already been investigated using FE methods for different applications. For welding, for example, Fu et al. [5] investigated in 2016 the influence of welding sequences on distortion, while Bhatti [6] focused on the influence of thermo-mechanical material properties on residual stresses and distortion. Islam et al. [7] additionally used numerical optimization to reduce distortion for arc welding processes and combined distortion modelling with optimization.

For conventional hardening, Prime investigated and predicted residual stresses in a steel ring [8] and Eck and coworkers [9] modelled the residual stress evolution in a more complex component, that is, tire protection chains. Schemmel et al., in 2015, pointed out the effect of component sizes on residual stress formation [10].

When phase transformation is involved, as in ferritic steel products, the concomitant volume expansion and transformation-induced plasticity (TRIP) [11] can have a strong impact on the resulting residual stress distributions, as discussed in the work of [10]. Deng pointed out the impact of phase transformation in medium carbon steels has on residual stresses [12]. When multiple phase transformations (i.e., austenite to martensite and bainite) appear, however, this has to be accounted for in the TRIP strain and modelling strategy is proposed.

The systematic use of simulation to improve residual stresses or distortion for ferritic steels has been discussed in the literature. Especially for welding, recently published papers investigated the tuning of process parameters in order to reduce residual stresses and distortions [13]; however, in some cases without considering TRIP and metallurgical volume expansion, as in the literature on welding mentioned above from Islam, Fu, and Bhatti. Nallathambi et al. [14] investigated the systematic reduction of distortion and the effects of certain material properties such as yield strength and transformation start temperatures with the FE method for cooled steel profiles. Islam et al. [7] even used optimization techniques to minimize distortion in welds, but did not take into account phase transformation effects.

In this paper, a numerical simulation of a tube quenching process is presented considering all relevant phase transformation effects with the goal of testing sets of process parameters that result in residual stresses as low as possible. To find processing routes that result in desired residual stress states with a defined phase composition, for example, mainly martensitic, mainly bainitic, or mixed, model-based design strategies are developed and used instead of iterative optimization routines.

It can be distinguished between *minimum*, *optimum*, and *low* residual stress configurations. Low residual stresses (close to zero) do not always imply that this is the optimum stress configuration, because, in some cases, it is beneficial to have high compressive residual stresses (however, residual stresses must be always self-equilibrated, and thus compressive stresses near the surface must lead to tensile stresses elsewhere). Stress configurations showing low residual stresses also do not automatically imply that this is a minimum possible residual stress configuration. To find a global minimum for all phase transformation and cooling configurations, a numerical minimization would be necessary, as performed, for example, in the work of [7].

The focus of this work is to use a FE integrated physical-based cooling model and test different cooling strategies to design different phase distri-

bution and stress configurations computationally. In the present work, the simulation results of three different strategies to provoke certain stress and phase configurations for a tube with 200 mm outer diameter and 22.65mm (200x22.65mm) wall thickness are investigated:

The cooling strategies include the following:

- (i) external cooling only, that is, the coolant is applied only to the tube's outer surface;
- (ii) both, external and internal cooling for mainly martensitic microstructure, that is, an additional cooling is applied through a cooling device from inside the tube;
- (iii) and both external and internal cooling, mainly to adjust a bainitic microstructure.

The critical physical quantity, giving rise to residual stresses in the investigated low-alloyed steels, is the temperature distribution, which, in turn, influences plasticity and TRIP. A strategy on how to reduce residual stresses after quenching is proposed. The main contribution of this work is modelling strain and stress evolution during coupled bainite and martensite transformation in seamless tubes. Differences between low-stress and high-stress cooling concepts are pointed out and mechanism-based cooling strategies are proposed to design tailored residual stress configurations in multiphase steel tubes.

### 3.3 Materials and methods

This section gives a brief model description of the investigated material, the used FE model and the employed cooling strategies.

#### 3.3.1 Model description

A tube with 200 mm outer diameter and 22.65 mm wall thickness is modelled by an axisymmetric thin strip (see Fig. 3.1) subject to generalized plane strain condition ( $\varepsilon_z = \text{const.}$ ) in axial direction. The FE software ABAQUS/Standard (version 2018) [15] is used and the chosen 2D axisymmetric element types are DCAX4 for the thermal and CAX4 elements for the mechanical calculation step with a size of 0.12x0.12mm and a generalized plane strain condition in axial direction. The model thickness is 0.12mm in axial direction, that is, one element line. The mechanical boundary conditions are shown in Fig. 3.1 and the thermal boundary conditions apply the heat transfer coefficients  $\alpha_{os}$  on the outer surface and  $\alpha_{is}$  on the inner surface and a continuous condition on the surfaces perpendicular to axial direction.

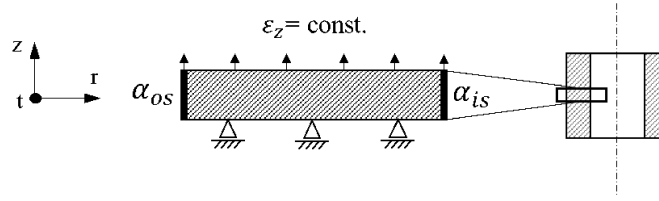


**Figure 3.1:** Schematic depiction of model and the applied boundary conditions.

**Table 3.1:** Cooling parameters for the three different cooling strategies.

Title	Internal Cooling ( $kg/m^2s^{-1}$ )	External Cooling ( $kg/m^2s^{-1}$ )	Cooling Speed ( $ms^{-1}$ )
Strategy 1	-	80	0.2
Strategy 2	100	10	0.2
Strategy 3	100	10	0.1

The tangential and radial strains  $\varepsilon_t$  and  $\varepsilon_r$  are

$$\varepsilon_t = \frac{u_r}{r} \quad \text{and} \quad \varepsilon_r = \frac{\partial u_r}{\partial r} \quad (3.1)$$

The cooling boundary conditions on the inner and outer surface impose the assumed process cooling conditions. An austenitic tube moves with  $880^\circ\text{C}$  into an array of eight cooling baskets with short gaps between them; within one cooling basket, the heat transfer coefficient is calculated following the work of [16] as a function of temperature and water amount and is greater than in the gaps, where the tube has no water contact, but is exposed to air. For contact with air,  $\alpha_{os}$  is constant at  $40\text{W/m}^2\text{K}$ . When internal cooling is applied,  $\alpha_{is}$  is calculated as described above using the work of [16], and is not applied by eight baskets, but by one inner cooling device. The setup is implemented in the FE software ABAQUS with the user subroutine FILM for the heat transfer coefficient, and a more detailed description of the manufacturing setup can be found in the work of [17].

The following variations of water amounts and cooling speeds are used, see Table 3.1 (the speed at which the tube moves along the cooling system).

The variation of the applied water amount changes the heat transfer coefficient, and thus the heat flux, which in turn governs the local temperature distributions and phase evolution. Diffusionless, that is, martensitic phase transformation, is modelled using the Koistinen–Marburger relationship [18], where the martensite growth rate  $\dot{z}_m$  is implemented proportional to the rate of undercooling  $\dot{T}$  and the still transformable remaining austenite fraction  $z$ , that is,  $\dot{z}_m = -\beta\dot{T}z_\gamma$ .

The phase transformation model for diffusive phase transformation is implemented using a model developed in three consecutive papers by Garrett

and Mahnken [19] for the basic framework, and in the works of [20, 21], who added a distinction for upper and lower bainite and included additional variant selection.

The model parameters were taken from the work of [17]. Alternative models for diffusive phase transformation at non-isothermal conditions use, for example, a stepwise isothermal Scheil approach based on the additivity principle described in detail in the works of [2, 4]. Lusk et al. [22] consider a set of thermodynamic Avrami-type equations as implemented, for example, by Prime [8]. In this work, a model proposed by Mahnken was chosen for its higher accuracy over a wide cooling range and the physical foundation of most of its parameters.

The phase transformation models are implemented in an incremental form in ABAQUS using user subroutines [15]. The subroutine USDFLD assigns  $N-1$  calculated product phase fractions to  $N-1$  variables of a user defined field, as the mother phase austenite is not assigned to an individual variable. To account for the change in properties for a combination of different phases, namely, the change in thermal expansion, volume expansion, TRIP strain, latent heat, Young's modulus, and Poisson's ratio, the properties  $P_k$  for  $k = 0, \dots, N$  phases are linearly weighted by their phase fraction  $z_k$  by the following:

$$P(T, z_k) = \sum_{k=0}^N P_k z_k, \quad (3.2)$$

The weighted thermal strain increment  $\varepsilon^{th}$  and volume expansion increment  $\varepsilon^{vol}$  are calculated in the user subroutine UEXPAN. The equivalent TRIP strain increment  $\varepsilon^{trip}$  is calculated in the user subroutine CREEP. The user subroutine HEATVAL accounts for the change in latent heat, following the works of [4, 17].

The TRIP strain during phase transformation [11] is implemented using the formulation of the work of [23]. The formulation was slightly adapted in the work of [17] and this work to account for the fact that the austenite is consumed by multiple phase transformations. The modification was not used to the full extent in our previous work [17], as the focus was on model development and not process design, but is of relevance now for combined martensite and bainite phase transformation and reads as follows:

$$\varepsilon_{ij}^{trip} = \frac{3}{2} K_k S_{ij} f'(z_1 \dots z_N) \dot{z}_k \quad (3.3)$$

where  $z_k$  is the fraction of product phase  $k$  and the function  $f'(z_1, \dots, z_N)$  ensures that the corresponding TRIP strain saturates with decreasing parent phase, which has transformed to  $1, \dots, N$  product phases:

$$f'(z_1 \dots z_N) = 2 \left( 1 - \sum_{i=1}^N z_i \right). \quad (3.4)$$

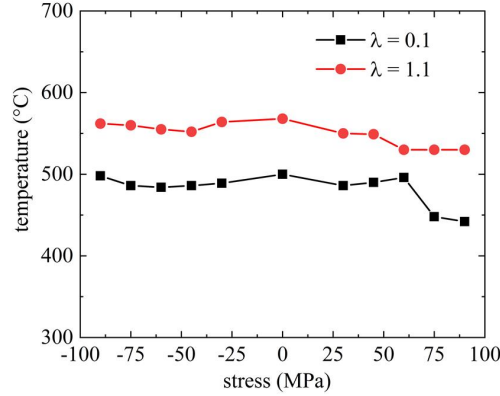


**Figure 3.2:** Dependency of the transformation start temperature of martensite  $M_s$  (black,  $\lambda = 0.1$ ) and of bainite  $B_s$  (red,  $\lambda = 1.1$ ) for different applied stresses.

The material parameters  $K_k$ , also known as the Greenwood–Johnson [11] parameter, are determined by means of dilatometric experiments performed at two different cooling rates to induce martensite or bainite formation, respectively, and subject to an additional mechanical load following the method as proposed in the work of [24]. These experiments also reveal if the phase transformation start temperatures ( $M_s$  and  $B_s$ ) are sensitive to the applied stress. Fig.3.2 shows the results for the transformation start temperatures for martensite ( $\lambda = 0.1$ ) ( $\lambda$  is time required for cooling from 800 to 500°C in hectoseconds) and bainite ( $\lambda = 1.1$ ) for an applied stress ranging from -90 to 90 MPa, which is about half the yield strength of the austenite at this temperature.

The stress applied during phase transformation has only a small impact on the transformation start temperature, as shown in Fig. 3.2 - not at all for the austenite–martensite transformation ( $\lambda = 0.1$ ) and very little for austenite–bainite phase transformation ( $\lambda = 1.1$ ). This allows a numerical calculation of the cooling problem in a weakly coupled manner because applied stresses do not affect the solution for the thermal field. So, the transient heat problem is solved first and the results serve as input for the mechanical problem.

The theoretical Greenwood–Johnson parameter for the martensite phase transformation at room temperature is as follows [11]:

$$K = \frac{5}{6} \frac{\Delta V/V}{\sigma_{Y,\gamma}} \sim \frac{5}{6} \frac{0.0261 RT}{250 MPa} \approx 8.7 \cdot 10^{-5} MPa^{-1} \quad (3.4)^1$$

<sup>1</sup>In the original paper the equation was accidentally given by  $\frac{5}{3} \frac{0.0261 RT}{250 MPa}$ , which yields the remaining plastic strain after a full transformation cycle, i.e.  $\alpha \leftrightarrow \gamma$ . The equation however, must be corrected by a factor of 1/2 to yield the remaining strain after  $\gamma \rightarrow \alpha$  transformation.

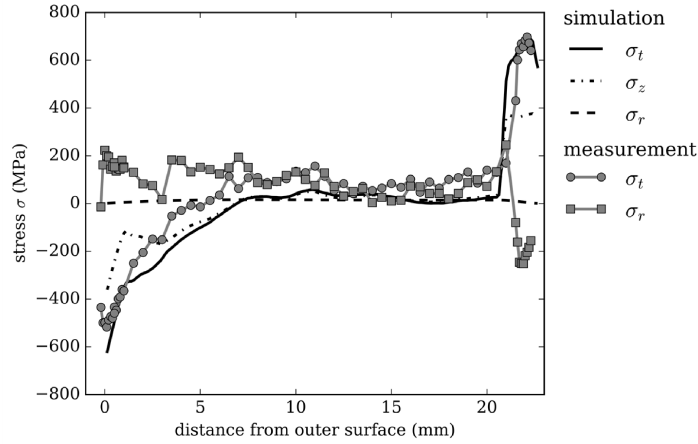


**Figure 3.3:** Comparison of high-energy X-ray diffraction residual stress measurements with simulation results for an industrial case.

The volume expansion  $\Delta V/V$  is 0.0261(-) after cooling to room temperature for martensite and 0.0264(-) for bainite, respectively. The value was calculated from dilatometer curves and corresponds to volume expansions given by the work of [25] for a steel with 0.25 wt.%C. The yield strength  $\sigma_{Y,\gamma}$  is the yield strength of the weaker phase, that is, the austenite yield strength of 250 MPa at a temperature range covering the transformation interval. Because it cannot be measured directly, it has to be extrapolated from tensile tests carried out at temperatures  $> M_s$ ; see the work of [26]. The measured values for the Greenwood–Johnson parameter are  $K_M = 8.9 \cdot 10^{-5} \text{MPa}^{-1}$  for martensite phase transformation and  $K_B = 8.83 \cdot 10^{-5} \text{MPa}^{-1}$  for bainite.

Temperature dependent thermo-physical properties are used, namely, the thermal expansion coefficient, heat capacity, and thermal conductivity, as well as temperature dependent elastic and plastic properties, with a temperature dependent Young’s modulus and Poisson’s ratio (calculated using JMatPro [27]) and temperature dependent yield strength and flow curves from measurement data for the phases austenite, martensite, and bainite. The material data and flow curves can be found in a previous publication [17].

For the model validation, a tube of the investigated dimension was produced in an industrial process using internal and external cooling and high-energy X-ray diffraction measurements were performed to determine tangential and radial residual stresses [17]. The process conditions were applied to the FE model and the simulation results are compared with the measurements in Fig. 3.3. The calculated stresses correlate qualitatively and quantitatively with the measurements in tangential direction. On the inner and outer surface, radial stresses have to be zero and the observed deviation in the measurement results is the result of artefacts.

### Design strategy

Considering two possible phase transformations in the model (i.e., from austenite to martensite/bainite), the current work focuses on finding cooling conditions that result in residual stresses close to zero MPa and different phase constituents.

Even if compressive stresses on the outer surface as for strategy 1 can be beneficial in some applications (e.g., corrosion, crack initiation), they may be detrimental in terms of distortion in subsequent process steps, such as annealing or machining. Hence, this work focuses generally on the stress evolution and, for this particular application, on their reduction.

It has been shown by the authors of [17] that areas with severe plastic deformation in austenite owing to thermal misfits show high residual stresses at room temperature. Therefore, the approach was to lower the thermal misfit in austenite, by lowering the temperature gradients with more moderate cooling and still preserving mainly martensite phase composition, as in strategy 2. To this end, the applied water amount was reduced and adjusted individually at the inner as well as the outer surface to obtain similar temperature gradients.

One way of producing mainly a bainitic microstructure is to cool at very low rates following a almost horizontal line of a continuous cooling transformation (CCT) phase diagram. In this work, however, the goal is to get lower bainite by ‘quasi’ isothermal transformation close to the martensite start temperature, as shown in strategy 3. This is achieved by quick cooling on the surfaces combined with self-annealing and the still warm inner area of the tube and is discussed in detail in the following results section.

## 3.4 Results

In this section, the simulation results for three different cooling strategies are discussed. The residual stress in the radial, axial, and tangential direction are denoted as  $\sigma_r$ ,  $\sigma_z$ , and  $\sigma_t$ . The total strain  $\varepsilon$  is split up into the sum of contributions from the elastic part  $\varepsilon^{el}$ , thermal expansion  $\varepsilon^{th}$  and metallurgical volume expansion  $\varepsilon^{vol}$ , and inelastic strain contributions from plasticity  $\varepsilon^p$  and transformation induced plasticity  $\varepsilon^{trip}$ . The used subscripts indices then denote the respective strain component.

$$\varepsilon = \varepsilon^{el} + \varepsilon^{th} + \varepsilon^{vol} + \varepsilon^p + \varepsilon^{trip} \quad (3.5)$$

### 3.4.1 Strategy 1

Cooling strategy 1 uses external cooling only, which for the investigated dimension, 200x22.65 mm, leads to a mainly martensitic microstructure. Fig. 3.4a shows the temperature evolution at a point on the inner surface



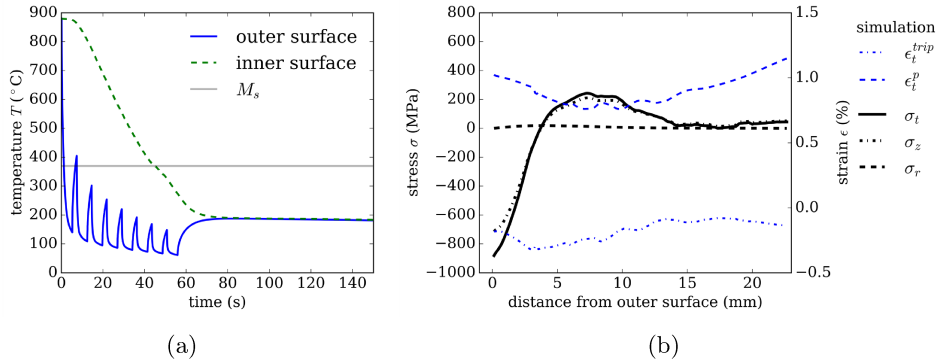


**Figure 3.4:** Strategy 1. (a) Temperature evolution using external cooling only. (b) Resulting residual stresses and plastic strain in tangential direction after quenching as a function of distance from the tube's outer surface.

and at the same axial position on the outer surface of the tube. The spikes of the curve pertaining to the temperature evolution on the outer surface result from the setup of the cooling equipment. The minima in the temperature distribution are always at the end of a cooling basket. Between two baskets, the still hot inner regions re-heat the outer surface when there is no contact with water, leading to the characteristic spiked temperature evolution.

Fig. 3.4b shows the residual stress distribution and plastic strain contributions  $\epsilon_t^p$  and  $\epsilon_t^{trip}$  in the tangential direction as a function of the distance from the outer surface. The compressive stresses in the tangential  $\sigma_t$  and axial  $\sigma_z$  direction of  $\sim 900$  MPa decaying towards the inner surface are characteristic for external cooling. Comparing this stress distribution for the dimension of 200 x 22.65 mm with a smaller dimension of 177.8 x 12.65 mm investigated in the work of [17] reveals that this trend is independent of the tube's dimension for the given steel class and cooling intensity.

The residual stress distribution in tangential and axial direction is essentially determined by the inelastic strain contributions  $\epsilon_t^p$  and  $\epsilon_t^{trip}$ . Thermal misfits that arise during cooling lead to plastic strain in austenite, which influences the stress distribution during transformation, and thus affects the TRIP contributions,  $\epsilon_t^{trip}$ . Meanwhile, the volume jump due to transformation into either martensite or bainite always leads to similar strain contributions  $\epsilon_t^{vol}$  over the cross section, and is thus not depicted in Fig. 3.4b. The evolution of plastic strain and TRIP strain for a purely martensitic, but representative reference case is discussed in detail in the work of [17]. Fig. 3.5a shows snapshots at specific times of the distribution of the martensite (green) and bainite (blue) fraction as a function of the distance from the outer surface. Fig. 3.5b shows the front view of Fig. 3.5a. The plots show how the phase transformation progresses; the martensitic transformation starts at the outer surface and progresses towards the inner surface over

time. A maximum of 20% bainite forms in the middle region.

The bainite formation in this middle region happens as a result of the cooling setup; here, the material points transform partly to martensite, but the transformation stops between two cooling baskets owing to reheating, which raises the temperature above the martensite start temperature  $M_s$ . Owing to the preceding transformation history (microplasticity, interface formation, and so on), the remaining austenite contains a large number of nucleation sites, thus giving rise to an accelerated formation of bainite. This is accounted for by the term  $(1 - z)^\gamma$  in Equation (12) the work of [20]. The variable is a constant growth parameter and  $z$  is the already transformed product phase fraction.

The expression  $(1 - z)^\gamma$  was modified in this work to account for the multiphase transformation to  $\left(1 - \sum_{i=1}^N z_i\right)^\gamma$  for  $i = 1, \dots, N$  product phases. This reduces the remaining austenite fraction also by the previously formed martensite fraction, which is no longer available for bainite formation.

### 3.4.2 Strategy 2

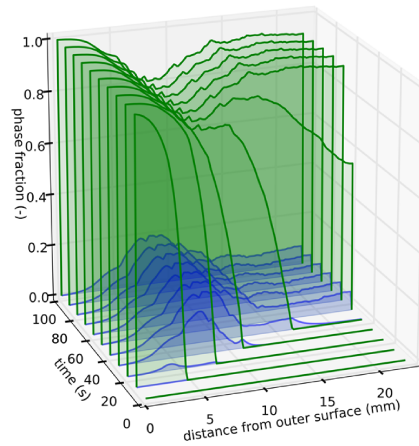
Fig. 3.6a,b show the temperature distribution for a quenching concept generating low-residual stresses; in this strategy, internal cooling is applied additionally to the external cooling (temperature on the inner surface is the green, dashed line in Fig. 3.6a). Martensite transformation starts from both surfaces: inner and outer. The inner region is cooled for only 3 s by an inner cooling device inserted into the tube, and is re-reheated subsequently by the still hot middle region of the tube's wall (curves for several different points in the middle region are not shown for better readability).

Comparing Fig. 3.6b to Fig. 3.4b shows that the residual stresses are reduced significantly; for example, on the outer surface from -900 MPa to -200 MPa and on the inner surface from 20 MPa to -150 MPa.

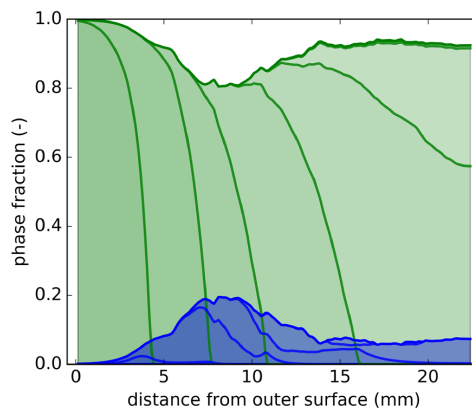
A comparison of the distribution of the plastic strain component in tangential directions shown in Fig. 3.6b versus Fig. 3.4b reveals the effect of the temperature gradient. These thermal misfits cause classical plasticity in the austenite with low yield strength.

The TRIP strain  $\varepsilon^{trip}$  remains of a similar magnitude (in the range of -0.4% to 0.0%) as for strategies 1 and 2, despite the slightly slowed down transformation— but with different distribution owing to the altered temperature profile and thermal misfits.

This is an expected result, as the austenite yield strength is not implemented as strain rate dependent, because no strong strain rate dependence was detected experimentally- and the integral under the phase evolution rate integrated over time must always be 1. Thus, a fully completed phase transformation always leads to a similar TRIP magnitude for similar cooling rate and the distribution is altered owing to changes in the stress state during transformation.



(a)



(b)

**Figure 3.5:** Strategy 1. (a) Snapshots at different times of phase distributions over distance from outer surface (green: martensite; blue: bainite). (b) Front view of Fig. 3.5a depicting phase distributions as a function of distance from the tube's outer surface.

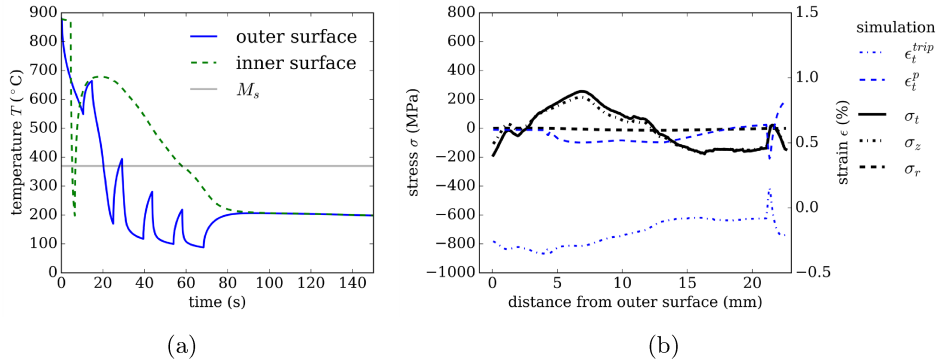


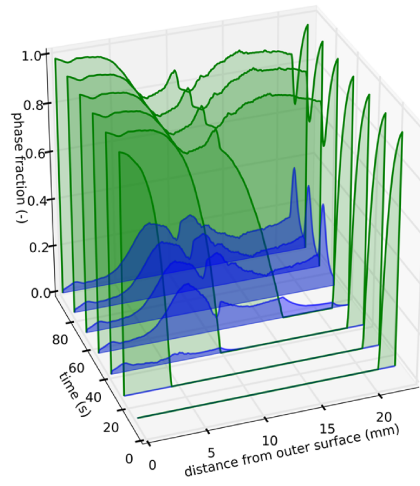
**Figure 3.6:** Strategy 2. (a) Temperature evolution using external and internal cooling. (b) Resulting residual stresses and plastic strain in tangential direction after quenching as a function of distance from the tube's outer surface.

Only the stress configuration changes as a result of thermal misfits. When the thermal misfits differ between the two cooling strategies, they change the stress state, plastic strain, and TRIP strain. Comparing Fig. 3.7b with Figure 10 in the work of [17] shows that a mainly martensitic microstructure is achieved in both cases. In the present study, much lower residual stresses are obtained by reducing the cooling intensity to a minimum.

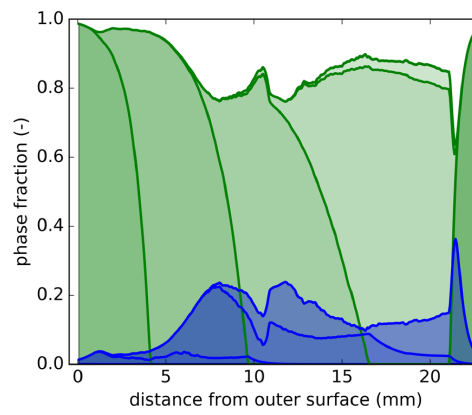
### 3.4.3 Strategy 3

The effect of the misfit strains in austenite becomes more obvious in cooling strategy 3, where martensite is formed only near the inner and the outer surface, while 100 vol.% bainite is formed in the middle region. The bainite formation is more favored in strategy 3 by the slow cooling in the middle region, as compared with strategy 1 and strategy 2; see Fig. 3.6a and Fig. 3.8a. Between 100 s and 300 s, bainite forms 'quasi-isothermal' with a cooling rate of about  $0.5K/s$ . When the cooling rate becomes lower after 70 s, and the 'quasi-isothermal' transformation begins. The radial temperature gradient across the tube's wall is close to zero; see Fig. 3.8a.

The plastic strain in tangential direction of 0.5% caused by thermal misfit on the outer surface (see Fig. 3.8b) is comparable to the plastic strain in strategy 2, as the cooling rates near the surface are initially similar. However, because, in strategy 3, the total amount of cooling is lower, the martensite transformation stops after 6 mm from the outer and 1.5 mm from the inner surface. Between 5 mm and 10 mm, the plastic strain drops to a lower value of 0.2%, from 0.5% to 0.2%. Comparing this to Fig. 3.9a reveals that this corresponds to the phase change caused by the change in



(a)



(b)

**Figure 3.7:** Strategy 2. (a) Snapshots at different times of phase distributions over distance from outer surface (green: martensite; blue: bainite). (b) Front view of Fig. 3.7a depicting phase distributions as a function of distance from the tube's outer surface.

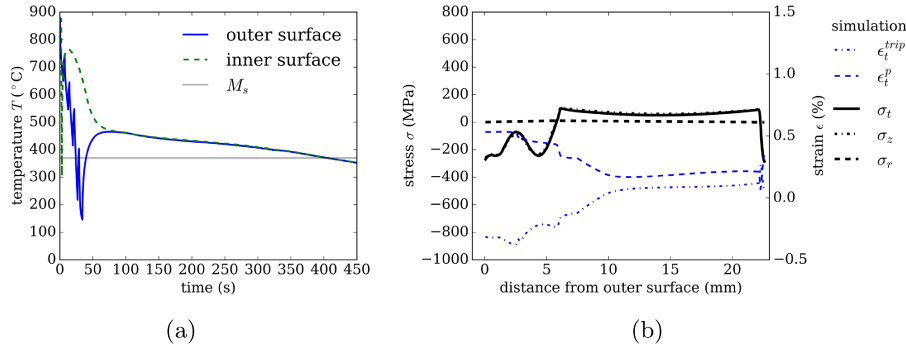
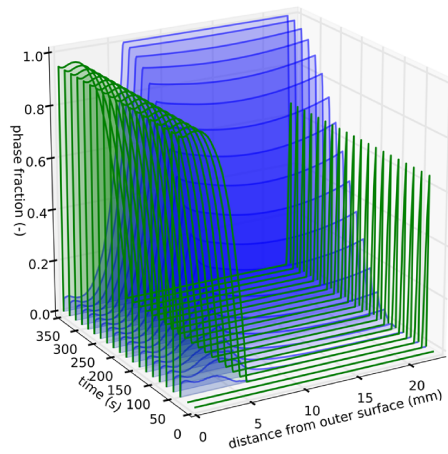


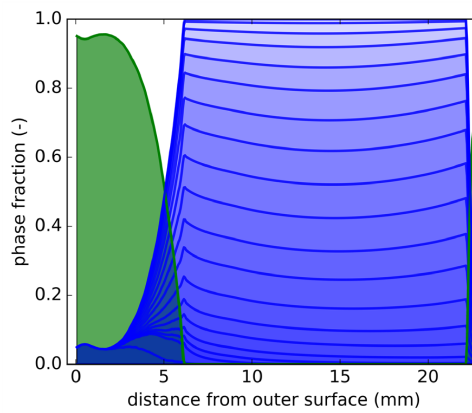
**Figure 3.8:** Strategy 3. (a) Temperature evolution using internal and external cooling. (b) Resulting residual stresses and plastic strain in tangential direction after quenching over distance from the outer tube’s surface.

the cooling conditions.

This overall bainite evolution for this ‘quasi-isothermal’ condition can be seen in Fig. 3.9b, where the phase fraction evolution follows an S-shape in a time interval between 50 and 350 s, as expected for a diffusive phase transformation. As mentioned in the previous section, the volume expansion of bainite formation is slightly larger than for martensite transformation (0.0261(-) for martensite compared with 0.0264(-) for bainite). The results show that the change in the residual stresses results from the much lower cooling rate, leading to less plastic strain and lower stresses during transformation. This in turn changes the TRIP strain and leads to overall residual stresses lower than 200 MPa. The presented results refer to a low-alloyed steel class with 0.25 wt.% carbon. Changes in the composition and grain size can affect the transformation start temperatures, as shown by [28]. Especially carbon affects the resulting yield strength, as documented experimentally by the authors of [29]. Volume expansion, yield strength, transformation start temperatures, and kinetics have been systematically shown to affect the resulting distortions or stresses by the authors of [6]. The plastic strain and TRIP strain are dependent on the austenite yield strength, which, in turn, correlates to the austenite grain size according to the Hall–Petch relationship, as shown by the authors of [26]. This implies that, when the austenite grain size is reduced, the yield strength and thus the resulting TRIP strain and plastic strain distribution will be lowered. The martensite yield strength depends on the block size and also corresponds to the former austenite grain size, as shown by the authors of [30].



(a)



(b)

**Figure 3.9:** Strategy 3. (a) Snapshots at different times of phase distributions over distance from outer surface (green: martensite; blue: bainite). (b) Front view of Fig. 3.9a depicting phase distributions as a function of distance from the tube's outer surface.

### 3.5 Discussion and conclusion

A multiphase numerical model is presented to show three systematic design strategies on how to adjust distinct microstructures and stress states in low-alloyed seamless steel tubes. The model accounts for the different physical phase transformation mechanisms relevant at the respective cooling rates. Three distinct cooling strategies and their effect on phase fraction and residual stress evolution were investigated: (i) strategy 1, resulting in a mainly martensitic microstructure; (ii) strategy 2, generating very low residual stress; and (iii) strategy 3, resulting in a predominantly bainitic microstructure.

The use of intense external cooling leads to a characteristic residual stress distribution regardless of the geometry with compressive stresses on the outer surface (177.8 mm x12.65 mm [16] or 200 mm x22.65 mm) for the investigated material and wall thickness range. Depending on the application and subsequent processing steps, a low-stress concept is not always a desirable option. If compressive stresses are favored, the simulation framework can be employed to find a maximum for compressive stresses on the inner and/or outer surface.

A combination of internal and external cooling can lower residual stresses considerably, while a similar microstructure can be preserved. This is shown by the comparison of strategy 1, using external cooling only, and strategy 2, where a combination of internal and external cooling and lower cooling rates reduce thermal misfits. The thermal misfits cause plastic strain  $\varepsilon^p$  in the austenitic state, as can be best seen in strategy 1, which is one of the main contributors to residual stresses. For the investigated cooling cases, the resulting residual stresses are dominated by both plastic strain,  $\varepsilon^p$ , and TRIP strain,  $\varepsilon^{trip}$ .

Different microstructures, mainly martensitic or mainly bainitic, at low residual stress levels can be adjusted with different intensities of internal and external cooling. Rapid cooling on both surfaces, as in strategy 2, can yield mainly martensitic microstructure, while short cooling followed by ‘quasi-isothermal’ bainitic transformation, as in strategy 3, yields a mainly bainitic microstructure, but both strategies result in low residual stresses.

To reduce residual stresses effectively, balanced phase transformation fronts from both surfaces during quenching are favorable and temperature gradients should be as low as possible to keep thermal misfits low, while still adjusting the desired microstructure. Further research should be dedicated to investigating the fundamental effect of prior martensite formation on the subsequent bainite transformation kinetics experimentally, with simulation methods, and to extending the modelling framework to include changes in chemistry and austenite grain sizes.

**Author Contributions:** Conceptualization, S.L. and W.E.; methodology,



S.L.; software, S.L.; validation, S.L., W.E., and T.A.; formal analysis, S.L.; investigation, S.L. and W.E.; resources, S.L., W.E., G.W., and J.K.; data curation, S.L.; writing—original draft preparation, S.L.; writing—review and editing, W.E., J.K., G.W., and T.A.; visualization, S.L.; supervision, W.E. and T.A.; project administration, W.E. and J.K.; funding acquisition, W.E., T.A., and J.K. All authors have read and agreed to the published version of the manuscript.

**Funding:** The authors gratefully acknowledge the financial support under the scope of the COMET program within the K2 Center "Integrated Computational Material, Process, and Product Engineering (IC-MPPE)" (Project No 859480). This program is supported by the Austrian Federal Ministries for Transport, Innovation, and Technology (BMVIT) and for Digital and Economic Affairs (BMDW), represented by the Austrian research funding association (FFG), and the federal states of Styria, Upper Austria, and Tyrol.

**Conflicts of Interest:** The authors declare no conflict of interest.

# Bibliography

- [1] S. Leitner, G. Winter, J. Klarner, T. Antretter, and W. Ecker. Model-Based Residual Stress Design in Multiphase Seamless Steel Tubes. *Materials*, 13(2):439, jan 2020. ISSN 1996-1944. doi: 10.3390/ma13020439. URL <https://www.mdpi.com/1996-1944/13/2/439>.
- [2] S. Denis, D. Farias, and A. Simon. Mathematical Model Coupling Phase Transformations and Temperature Evolutions in Steels. *ISIJ International*, 32(3):316–325, 1992. ISSN 09151559. doi: 10.2355/isijinternational.32.316.
- [3] J. Rohde and A. Jeppsson. Literature review of heat treatment simulations with respect to phase transformation, residual stresses and distortion. *Scandinavian Journal of Metallurgy*, 29(2):47–62, 2000. ISSN 03710459. doi: 10.1034/j.1600-0692.2000.d01-6.x.
- [4] C. H. Gür and J. Pan. *Handbook of Thermal Process Modelling*. CRC Press, Boca Raton, 2009. ISBN 9780849350191.
- [5] G. Fu, M. I. Lourenço, M. Duan, and S. F. Estefen. Influence of the welding sequence on residual stress and distortion of fillet welded structures. *Marine Structures*, 46:30–55, 2016. ISSN 09518339. doi: 10.1016/j.marstruc.2015.12.001. URL <http://dx.doi.org/10.1016/j.marstruc.2015.12.001>.
- [6] A. A. Bhatti, Z. Barsoum, H. Murakawa, and I. Barsoum. Influence of thermo-mechanical material properties of different steel grades on welding residual stresses and angular distortion. *Materials and Design*, 65:878–889, 2015. ISSN 18734197. doi: 10.1016/j.matdes.2014.10.019. URL <http://dx.doi.org/10.1016/j.matdes.2014.10.019>.
- [7] M. Islam, A. Buijk, M. Rais-Rohani, and K. Motoyama. Simulation-based numerical optimization of arc welding process for reduced distortion in welded structures. *Finite Elements in Analysis and Design*, 84: 54–64, 2014. ISSN 0168874X. doi: 10.1016/j.finel.2014.02.003. URL <http://dx.doi.org/10.1016/j.finel.2014.02.003>.

- [8] M. B. Prime, V. C. Prantil, P. Rangaswamy, and F. P. García. Residual stress measurement and prediction in a hardened steel ring. *Materials Science Forum*, 347(January 2014):223–228, 2000. ISSN 02555476. doi: 10.4028/www.scientific.net/msf.347-349.223.
- [9] S. Eck, P. Prevedel, S. Marsoner, W. Ecker, and M. Illmeier. Using finite element simulation to optimize the heat treatment of tire protection chains. *Journal of Materials Engineering and Performance*, 23(4):1288–1295, 2014. ISSN 15441024. doi: 10.1007/s11665-013-0854-y.
- [10] M. Schemmel, P. Prevedel, R. Schöngrundner, W. Ecker, and T. Antretter. Size effects in residual stress formation during quenching of cylinders made of hot-work tool steel. *Advances in Materials Science and Engineering*, 2015, 2015. ISSN 16878442. doi: 10.1155/2015/678056.
- [11] G. W. Greenwood and R. H. Johnson. The deformation of metals under small stresses during phase transformations. *Proceedings of the Royal Society of London. Series A. Mathematical and Physical Sciences*, 283 (1394):403–422, 1965. ISSN 2053-9169. doi: 10.1098/rspa.1965.0029.
- [12] D. Deng. FEM prediction of welding residual stress and distortion in carbon steel considering phase transformation effects. *Materials and Design*, 30(2):359–366, 2009. ISSN 02641275. doi: 10.1016/j.matdes.2008.04.052.
- [13] R. Pietzsch, M. Brzoza, E. Kaymak, Y. Specht, and A. Bertram. Minimizing the Distortion of Steel Profiles by Controlled Cooling. *steel research international*, 76(5):399–407, may 2005. ISSN 16113683. doi: 10.1002/srin.200506028. URL <http://doi.wiley.com/10.1002/srin.200506028>.
- [14] A.K. Nallathambi, Y. Kaymak, E. Specht, and A. Bertram. Sensitivity of material properties on distortion and residual stresses during metal quenching processes. *Journal of Materials Processing Technology*, 210 (2):204–211, 2010. ISSN 09240136. doi: 10.1016/j.jmatprotec.2009.09.001.
- [15] Dassault Systems. Abaqus standard. URL <https://www.3ds.com/products-services/simulia/products/abaqus/abaqusstandard/>.
- [16] J. Wendelstorf, K. H. Spitzer, and R. Wendelstorf. Spray water cooling heat transfer at high temperatures and liquid mass fluxes. *International Journal of Heat and Mass Transfer*, 51(19-20):4902–4910, 2008. ISSN 00179310. doi: 10.1016/j.ijheatmasstransfer.2008.01.032.

- [17] S. Brunbauer, G. Winter, T. Antretter, P. Staron, and W. Ecker. Residual stress and microstructure evolution in steel tubes for different cooling conditions – Simulation and verification. *Materials Science and Engineering A*, 747:73–79, 2019. ISSN 09215093. doi: 10.1016/j.msea.2019.01.037. URL <https://doi.org/10.1016/j.msea.2019.01.037>.
- [18] D. P. Koistinen and R. E. Marburger. A general equation prescribing the extent of the austenite-martensite transformation in pure iron-carbon alloys and plain carbon steels. *Acta Metallurgica*, 7(1):59–60, 1959. ISSN 00016160. doi: 10.1016/0001-6160(59)90170-1.
- [19] R. P. Garrett, S. Xu, J. Lin, and T. A. Dean. A model for predicting austenite to bainite phase transformation in producing dual phase steels. *International Journal of Machine Tools and Manufacture*, 44(7-8):831–837, 2004. ISSN 08906955. doi: 10.1016/j.ijmachtools.2004.01.004.
- [20] R. Mahnken, A. Schneidt, S. Tschumak, and H. J. Maier. On the simulation of austenite to bainite phase transformation. *Computational Materials Science*, 50(6):1823–1829, 2011. ISSN 09270256. doi: 10.1016/j.commatsci.2010.12.032. URL <http://dx.doi.org/10.1016/j.commatsci.2010.12.032>.
- [21] R. Mahnken, A. Schneidt, T. Antretter, U. Ehlenbröcker, and M. Wolff. Multi-scale modeling of bainitic phase transformation in multi-variant polycrystalline low alloy steels. *International Journal of Solids and Structures*, 54:156–171, 2015. ISSN 00207683. doi: 10.1016/j.ijsolstr.2014.10.021. URL <http://dx.doi.org/10.1016/j.ijsolstr.2014.10.021>.
- [22] M. Lusk, G. Krauss, and H.-J. Jou. A Balance Principle Approach for Modeling Phase Transformation Kinetics. *Le Journal de Physique IV*, 05(C8):C8–279–C8–284, 1995. ISSN 1155-4339. doi: 10.1051/jp4:1995839.
- [23] J. B. Leblond, J. Devaux, and J. C. Devaux. Mathematical modelling of transformation plasticity in steels I: Case of ideal-plastic phases. *International Journal of Plasticity*, 5(6):551–572, 1989. ISSN 07496419. doi: 10.1016/0749-6419(89)90001-6.
- [24] S. Neubert, A. Pittner, and M. Rethmeier. Experimental determination of TRIP-parameter K for mild- and high-strength low-alloy steels and a super martensitic filler material. *SpringerPlus*, 5(1), 2016. ISSN 21931801. doi: 10.1186/s40064-016-2474-0.

- [25] J. M. Moyer and G. S. Ansell. The volume expansion accompanying the martensite transformation in iron-carbon alloys. *Metallurgical Transactions A*, 6(9):1785–1791, sep 1975. ISSN 0360-2133. doi: 10.1007/BF02642308. URL <http://link.springer.com/10.1007/BF02642308>.
- [26] L. Norström. The influence of nitrogen and grain size on yield strength in type AIS1 316L austenitic stainless steel. *Metal Science*, 11(6):208–212, 1977. ISSN 03063453. doi: 10.1179/msc.1977.11.6.208.
- [27] Sente Software Ltd. Jmatpro. URL <https://www.sentesoftware.co.uk/jmatpro>.
- [28] C. Heinze, A. Pittner, M. Rethmeier, and S. S. Babu. Dependency of martensite start temperature on prior austenite grain size and its influence on welding-induced residual stresses. *Computational Materials Science*, 69:251–260, 2013. ISSN 09270256. doi: 10.1016/j.commatsci.2012.11.058. URL <http://dx.doi.org/10.1016/j.commatsci.2012.11.058>.
- [29] J.M Chilton and P.M Kelly. The strength of ferrous martensite. *Acta Metallurgica*, 16(5):637–656, may 1968. ISSN 00016160. doi: 10.1016/0001-6160(68)90137-5. URL <https://linkinghub.elsevier.com/retrieve/pii/0001616068901375>.
- [30] S. Morito, H. Yoshida, T. Maki, and X. Huang. Effect of block size on the strength of lath martensite in low carbon steels. *Materials Science and Engineering A*, 438-440(SPEC. ISS.):237–240, 2006. ISSN 09215093. doi: 10.1016/j.msea.2005.12.048.

## Chapter 4

### Publication 3

*Residual stress evolution in low-alloyed steels on  
three different length scales*

Unpublished manuscript.

## Residual stress evolution in low-alloyed steels on three different length scales

### Authors

Silvia Leitner<sup>1\*</sup>, Gerald Winter<sup>2</sup>, Jürgen Klarner<sup>2</sup>, Thomas Antretter<sup>3</sup>,  
Werner Ecker<sup>1</sup>

<sup>1</sup>Materials Center Leoben Forschung GmbH, Roseggerstraße 12,  
Leoben, Austria

<sup>2</sup>voestalpine Tubulars GmbH & Co KG, Alpinestrasse 17,  
Kindberg-Aumuehl, Austria

<sup>3</sup>Institute of Mechanics, Montanuniversitaet Leoben, Franz Josef Strasse  
18,  
Leoben, Austria

\*corresponding author: [silvia.leitner@mcl.at](mailto:silvia.leitner@mcl.at)

### *Highlights*

- Quantifying higher order residual stresses in cooled seamless steel tubes
- Mesoscopic residual stresses calculated as function martensite start temperature and segregation line chemistry
- Ranking of residual stress formation potential of common inclusions

### *Keywords*

Finite Element method; Residual stresses; Higher order stresses; Phase transformation; Heat treatment; Low-alloyed steel;

## 4.1 Abstract

The work presents a qualitative and quantitative model-based and experimentally validated residual stress evolution in low-alloyed steel at three different length scales during heat treatment. For a seamless steel tube the macroscopic temperature, phase and stress evolution is calculated by means of a continuum model of the heat treatment process of the tube. The strain and temperature evolution is transferred to a submodel, which resolves the locally varying chemistry being a result of interdendritic segregation. This allows an assessment of mesoscopic stresses which may contribute to lower local crack growth resistance and corrosion properties. Within the segregation lines and the surrounding matrix precipitates form. They are categorized with respect to their tendency for formation of microscopic residual stresses. After rapid cooling macroscopic stresses up to 700 MPa may form dependent on the cooling procedure- as well as mesoscopic stresses up to  $\Delta 50$  MPa. Common inclusions are ranked by their tendency for residual stress formation.

## 4.2 Introduction

The residual stresses in low-alloyed steels are of interest, since they may deteriorate the steel's mechanical performance. Residual stresses can affect fatigue behavior [1] and also influence interaction with hydrogen [2]. Thus, quantifying residual stresses is an important step to guarantee component integrity. Since residual stresses exist on different length scales, i.e. they self-equilibrate at different characteristic lengths [3], their cause and scale determining the mechanical performance is not known a priori. Bouchard and Withers displayed for the example of a weld line in steel in 2004 [3] which scales are to be considered. They classify type I as macroscopic residual stresses, where the characteristic length  $\lambda$  over which they self-equilibrate is about the component size  $S$ ; type II residual stresses appear on length scales of  $3g \leq \lambda \leq 10g$ , where  $g$  denotes the grain size; for type III residual stress  $\lambda \leq g$ . In this work we refer to type I stresses as macroscopic, type II as mesoscopic, and type III as microscopic residual stresses.

Modeling approaches to combine different length scales were, for example, published by [4] for the example of a high speed tool steel. Golanski [5] published in 1997 a general approach on how to homogenize and transfer the effect of residual stresses from one scale to another.

Breaking the microstructure down into calculable pieces is frequently accomplished by means of representative volume elements (RVEs). If the necessary volume is too big for efficient computations, smaller elements with lower complexity can be considered such as statistical RVEs (SRVEs). Also real geometry models, as in Zhang (2016) [6] can be used if the focus is on



investigating geometry effects. Zhang et al also reported in 2016 that in this multiscale setup the residual stresses are dominated by those caused by thermal misfits superimposed with the macroscopic stress state.

Residual stresses on the macroscopic scale are calculated in this work using a continuum model developed in [7] which yields temperature, phase fraction and temperature evolution as a function of the tube's radial position during heat treatment consisting of quenching and optional subsequent tempering. A study on how to adapt the quenching process in order to lower residual stresses is published in [8].

The mesoscopic model of a section of the tube's wall focuses on residual stresses around segregation lines (planes), caused by interdendritic segregation during casting. This segregation produces local chemical inhomogeneities which can be the source of residual stresses. The segregation structure was determined from micrographs. A simplified model of an infinite segregation plane is created for further analysis.

The microscopic substructure is implemented by means of a "characteristic" volume element taking precipitate stress fields into account with prolate to oblate randomly distributed ellipsoids with an experimentally verified phase fraction.

Residual stresses are never directly experimentally accessible, but are always calculated from residual strains. Macroscopic stresses are accessible via strain measurement techniques, such as technological experiments with strain gauges or cut compliance tests [9]. The stresses are then calculated using elastic, macroscopic material properties. The final stress state can be characterized this way after any manufacturing step. An accompanying thermo-mechanical simulation accounting for the phase transformations provides insight to the stress formation mechanisms during processing.

The mesoscopic residual stresses (strains) around segregated areas referred to in this work, are difficult to access experimentally. They equilibrate in steels on length scales which are on an intermediate level between the grain structure on the lower boundary and the macroscopic continuum properties on the upper bound ( $1g \leq \lambda \leq 3g$ ), and are on a slightly smaller scale than in the definition given by [3]. Due to the chemical inhomogeneities, properties such as lattice parameters and stiffness change locally, which complicates the correlation of strain fields with stress fields.

Siwecki and colleagues [10] calculated the residual stresses due to segregation samples from heavy steel plates after quenching. This experimental study calculates the residual stresses from residual strains. They measured comparable chemical variations for Cr and Mo as considered in this work but observed larger changes in local carbon content. Their calculations yield similar magnitudes of residual stresses assuming the same elastic properties in segregated and depleted zone. In this work we numerically investigate the effect of the macroscopic stress state in addition to the isolated investigation of the effect of chemical variation. The variation of material properties due

to chemical variation is additionally considered.

To quantify mesoscopic residual stresses numerically in a low- and micro-alloyed steel, an experimentally verified modeling approach is used. Transformation kinetics, as well as relevant material properties are varied with respect to chemical composition to characterize the effect of composition change on residual stresses.

Microscopic stresses around inclusions or even around dislocation cores can experimentally be accessed with high resolution imaging techniques, such as TEM or high-resolution TEM [11] or also using X-ray diffraction and can again be calculated from strain maps [9]. A modeling approach was selected to determine microscopic stresses in low-alloyed steel, to give a qualitative and quantitative ranking of different inclusion types as well as to determine average and local effects of inclusions on the matrix stress state. First the average residual stress formation potential based on thermo-elastic considerations after [12] is calculated for common inclusion types. Then the histograms for maximum principal stresses as a function of precipitate volume fraction are compared.

### 4.3 Methods and Modeling

Residual stress formation in micro-alloyed steel on three different length scales is modeled. The following models are used, see in Fig. 4.1: (i) a process model calculating the temperature, phase and residual stress evolution on a macroscopic scale, developed in [7, 8] (ii) a model on the mesoscopic scale describing an infinite segregation "line" (plane) and (iii) a volume element containing inclusions for calculating microscopic stresses.

On the mesoscopic scale two different model variants are used: an *unconstrained* model, where the reference point (RP, see Fig. 4.1) remains unconstrained during cooling to isolate the contribution of chemical variation on residual stress formation. In the second mesoscopic model, referred to as the mesoscopic *submodel*, the thermal and mechanical boundary conditions from different points of the macroscopic model (i.e. on the outer surface point 1, and on the inner surface point 2) are transferred to this model in order to determine the effect of macroscopic gradients on the mesoscopic scale in addition to chemical variation. Since the mesoscopic model describes a selected volume element and not a representative VE, the applied boundary conditions are compensated for the elastic anisotropy due to the geometrical constellation in the selected volume element.

In the mesoscopic model the direction 3 coincides with the tangential direction  $t$ , and direction 1 with the radial direction  $r$  of the macroscopic model. For the microscopic model, the precipitates are statistically oriented, resulting in an isotropic material response of the volume element and no sub-coordinate system is given here.

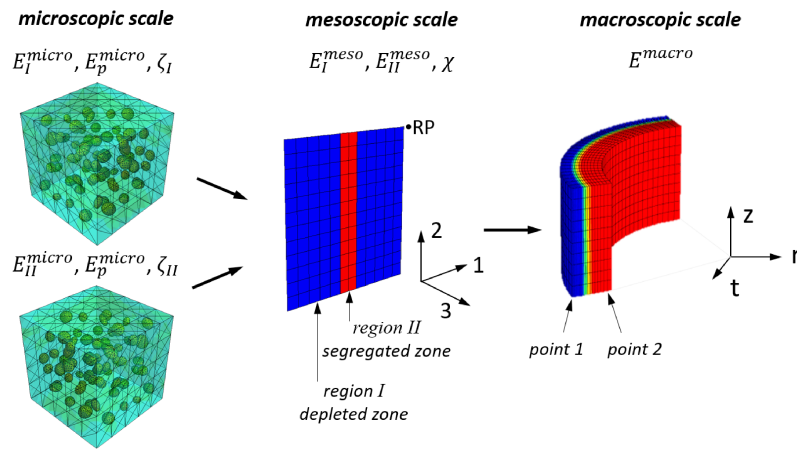


**Figure 4.1:** Schematic overview over the mixture of properties on the different modeling scales: In the microscopic model the material properties of matrix  $E_i^{micro}$  are mixed with the precipitate properties  $E_p^{micro}$  of the volume fraction  $\zeta_i$  for the regions  $i = I, II$  to obtain the mesoscopic properties  $E_I^{meso}$  and  $E_{II}^{meso}$ . In the mesoscopic model  $E_I^{meso}$  and  $E_{II}^{meso}$  are mixed with the experimentally determined volume fraction  $\chi$  to calculate the macroscopic modulus  $E^{macro}$ . For two different points point 1 and point 2 the mesoscopic residual stresses are calculated by means of a mechanical submodel using the reference point RP. The microscopic residual stresses are calculated using  $E_i^{micro}$  and  $E_p^{micro}$  for different precipitate volume fractions  $\zeta_i$ .

The mesoscopic residual stress formation is influenced by local chemical inhomogeneities, which alter phase transformation kinetics and material properties. The changes in martensite start temperature  $M_s$ , thermal expansion  $\alpha$ , metallurgical volume expansion  $\Delta V$  and Young's modulus  $E_I^{micro}$  and  $E_{II}^{micro}$  for the depleted region (region I, see Fig. 4.1) and the segregated region (region II, see Fig. 4.1) are varied based on measured variations in C, Mo and Cr content.

The depleted region I and the segregated region II can differ in precipitate volume fraction  $\zeta_i$ , for  $i = I, II$ . Thus the mesoscopic Young's modulus  $E_i^{meso}$  in the corresponding region contain a carbon content dependent matrix contribution  $E_i^{micro}$  a contribution from the precipitates  $E_p^{micro}$ . It is assumed that the regions I and II contain the same species of precipitates and only the volume fraction differs.

The mesoscopic moduli  $E_i^{meso}$  for the regions  $i = I, II$  can be calculated using a homogenization function  $f$ :

$$E_i^{meso} = f(E_i^{micro}, \zeta_i, E_p^{micro}) \quad (4.1)$$

The homogenization function  $f$  can range from the Voigt upper bound of  $((1 - \zeta_i)E_i^{micro} + \zeta_i E_p^{micro})$  to the Reuss lower bound  $((1 - \zeta_i)/E_i^{micro} + (\zeta_i/E_p^{micro})^{-1})$ . For the investigated case  $f$  is between the upper and lower bound and is calculated numerically using the microscopic model.

$E_I^{micro}$ ,  $E_{II}^{micro}$  are a-priori unknown since the variation in carbon content between region I and region II is, known but not the total content. In a first step,  $E^{meso}$  is calculated as a function of precipitate volume fraction  $\zeta$  and C content as a preliminary result, see Fig. 4.2. For an experimentally observed volume fraction of  $\zeta = 4\%$  in region I and II the microscopic moduli  $E_i^{micro}$  are adjusted, that the resulting mesoscopic moduli  $E_i^{meso}$  yield a measured macroscopic modulus  $E^{macro}$  for the experimentally determined segregation line phase fraction  $\chi = 20\%$ .

The macroscopic stiffness  $E^{macro}$  is calculated using a second numerical homogenization function  $F$ , which is provided by the mesoscopic unconstrained model. The volume fraction  $\chi$  of the segregated region I and the mesoscopic moduli serve as input

$$E^{macro} = F(\chi, E_I^{meso}, E_{II}^{meso}). \quad (4.2)$$

In the elastic consideration, the stiffness of the embedded precipitates adds to these moduli in the depleted region I and the segregated region II.

With the thus determined microscopic and mesoscopic elastic properties, the stresses on the corresponding length scales can be calculated with the above presented finite element models for quenched and tempered state. To quantify the microscopic residual stresses around inclusions and precipitates, a number of common inclusions in low-alloyed steel is selected and compared with respect to their potential for thermo-elastic residual stress formation.

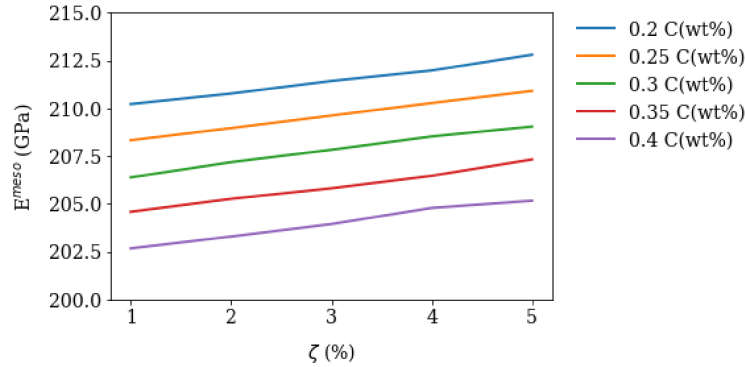


**Figure 4.2:** Calculated Young's modulus  $E^{meso}$  as a function of precipitate volume fraction  $\zeta$  and different matrix carbon contents.

#### 4.3.1 Phase transformation model

The phase transformation model describes the displacive phase transformations for two product phases  $z_i$  for  $i = 1, 2$  from austenite to martensite and bainite. The kinetic is governed by the Koistinen Marburger kinetic for transformation to martensite and by a model developed by Garrett and Mahnken for transformation to bainite. The model parameters were adjusted using dilatometer curves for different cooling rates and can be found in our previous publication [7]. The phase transformation kinetic is combined with the concomitant changes in material properties and transformation related effects by a user defined field in ABAQUS [13]. The current phase composition is assigned to field variables and the temperature dependent data for elasticity, yield curves, thermal expansion, thermal conductivity and specific heat of the individual phases are mixed accordingly [7, 8].

The phase transformation from austenite to martensite primarily depends on the carbon content, which alters the martensite start temperature. An exponential correlation model for change in martensite start temperature [14] as a function of local composition is implemented. The bainite phase transformation also depends on carbon and other alloying elements, but for the work at hand was considered to be unchanged since under process conditions no bainite is formed.

#### 4.3.2 Macroscopic model

The macroscopic phase transformation model was developed to calculate the temperature, phase and residual stress evolution in seamless steel tubes during accelerated cooling [7, 8]. In the investigated manufacturing setup, the tube moves through a cooling equipment consisting of eight cooling baskets, which apply spray water. This yields a non-continuous cooling progress. Temperature gradients, phase evolution and residual stresses differ on the

inner and outer surface. The temperature dependent elastic, plastic and thermophysical properties for the macroscopic model are used from [7, 8].

The macroscopic cooling process is investigated for a tube of 12.65 mm wall thickness and 177.8 mm outer diameter. The non-continuous cooling on the outer surface and high temperature gradients yield a "spiky" temperature profile over time, while on the inside the temperature decays continuously over time. Two submodels are devised from this macroscopic model: (i) on the outer and (ii) on the inner surface. The effect of different local temperature evolution and the tube's macroscopic mechanics on segregation lines is investigated.

### 4.3.3 Mesoscopic model

In the mesoscopic model (see Fig. 4.1), residual stresses in an infinite segregation plane (called segregation "line") and the depleted areas are investigated.

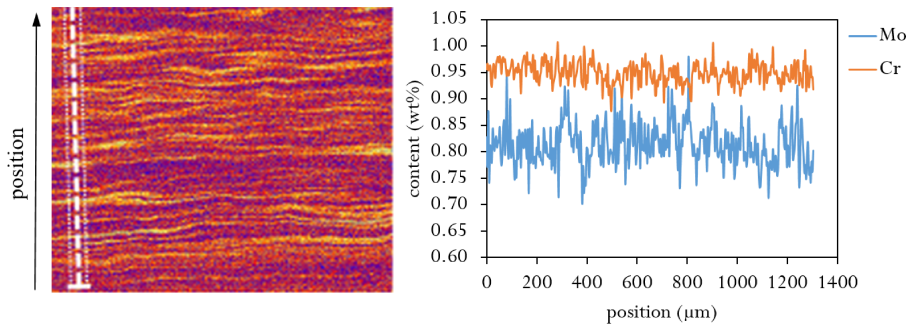


**Figure 4.3**

Since the chemical composition in the segregation lines differ from the depleted zones in Mo, Cr and C concentration. Residual stress evolution is affected by a change in mechanical, thermos-physical and phase transformation properties. The local chemical enrichment in the segregation lines was determined using electron diffraction scattering (EDX) scanning over the tubes cross section and an exemplary measurement is shown in Fig. 4.3. The local enrichment in carbon was calculated from high-energy x-ray diffraction on 2 mm thick tube segments, where macroscopic tangential, axial and radial stresses are relieved. The measurements were performed at the P07 beamline of Helmholtz-Zentrum Geesthacht at PETRA III synchrotron source of DESY in Hamburg with an energy of 87 keV. From the determined lattice parameter in the as-quenched state, the relative carbon variation was calculated using the correlation published by Moyer [15]. A maximum to minimum difference of 0.03wt%C was determined. For the calculations, a much broader change in carbon content is considered to evaluate a broader

spread of chemical variation.

As mentioned before, two submodels on the tube's outer (point 1) and inner (point 2) surface are investigated. The mechanisms driving this mesoscopic residual stress formation are revealed using an *unconstrained* mesoscopic model without the submodel boundary conditions from the macroscopic model that is subjected to cooling. The boundary conditions in the unconstrained case are generalized plane strain boundary conditions in the three directions 1,2,3 since the model is small compare to the tube's wall thickness. It is later shown, that this simplification is possible since the mesoscopic stresses act superimposed to the macroscopic stresses despite all non-linearities during phase transformation.

For the *submodeling* case the displacements resulting from the macroscopic model are transferred to the reference point while the outer faces preserve a generalized plane strain state, as shown in Fig. 4.4.

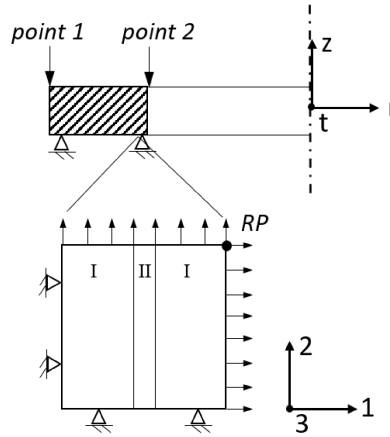


**Figure 4.4:** Schematic model description of the macroscopic axisymmetric process model with constant strain in axial direction ( $\varepsilon_z = \text{const.}$ ) and the submodel on the inner and outer tube's surface as generalized plane strain model in direction 1,2 and 3.

The mechanical properties, including the elastic and plastic material properties mainly depend on grain size and local carbon content. Bechet-Beaujard etching and electron back scattering diffraction (EBSD) pattern revealed, that the former austenite grain size and martensite structure are unaffected by the chemical variation. Thus, it is assumed that the plastic and elastic properties in austenite are equal for segregated and non-segregated areas. The occurring stresses after phase transformation do not exceed the product yield strength in martensite and thus only the change in elastic properties of the product phase was considered relevant. Souissi [16] has calculated the dependence of Young's modulus in martensite as a function of carbon content and with the determined carbon variation, the moduli

vary by 0.5% between segregated and non-segregated area .

The phase transformation kinetics in the segregated (region II) and in the depleted region (region I) are derived from the macroscopic model with a few changes in the segregation line (region II):

- The thermal expansion is changed as a function of carbon content from 0.25 to 0.4 wt%, see Fig. 4.5a.
- The Young's modulus in the segregated area is changed according to the carbon content, see Fig. 4.5b following [16].
- The volume expansion is changed as a function of carbon content from 0.25 to 0.4 wt%, see Fig. 4.5c.
- The martensite start temperature  $M_s$  is shifted to lower temperatures due to the higher carbon, Mo and Cr content following the exponential model [14], see Fig. 4.5d.

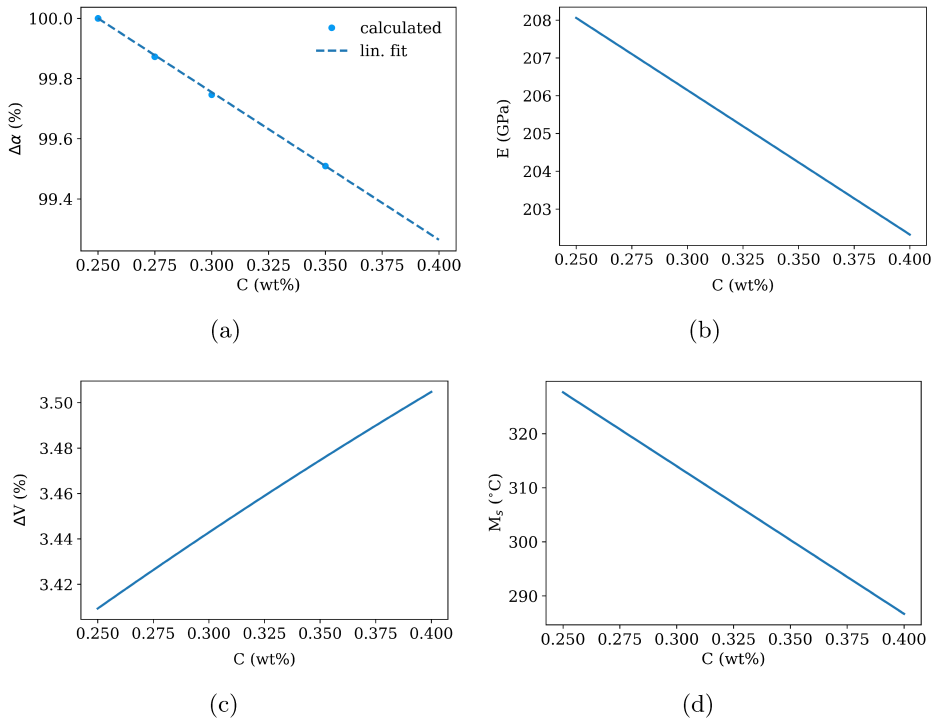


**Figure 4.5:** Dependency of difference in thermal expansion coefficient  $\Delta\alpha$  and metallurgic volume expansion  $\Delta V$  as function of carbon content as well as Young's modulus  $E$  and martensite start temperature  $M_s$  as function of carbon content.



The total coefficient of thermal expansion was calculated using JMatPro [17] as a function of chemistry and is shown in Fig. 4.6 - for different carbon content at different Cr and Mo concentrations, which are the maximum and minimum values from Fig. 4.3. The thermal expansion coefficient with the segregation chemistry is higher than for the depleted region. This implies, that during normal cooling the segregation line would contract more than the depleted zone and would be in tensile stress regime.

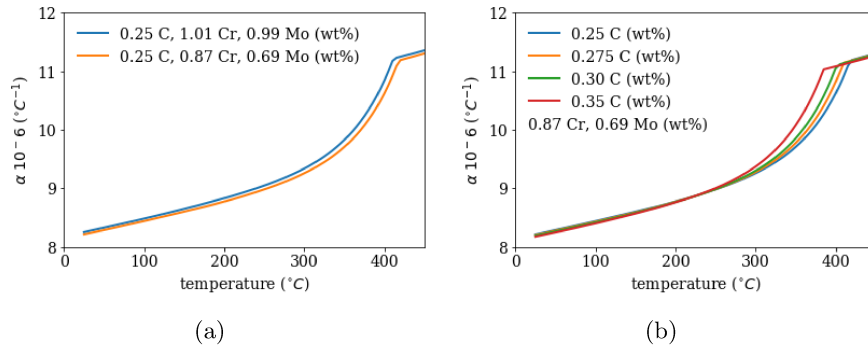


**Figure 4.6:** Calculated thermal expansion coefficient  $\alpha$  (with JMatPro) as function of temperature for different (a) Cr and Mo content for the depleted region I (0.87%Cr,0.69%Mo) and for the segregated region II (1.01%Cr,0.99%Mo) and (b) carbon content in the depleted zone.

In the unconstrained version of the mesoscopic model the thermal expansion, volume expansion, transformation start temperature and  $E^{micro}$  are continuously varied as function of carbon content from 0.25 to 0.4 wt%C. For the submodel case, a carbon segregation of 0.03 wt%C is assumed. This yields a total carbon content in region I of 0.235wt% and in region II 0.265wt% for a precipitate volume fraction of  $\zeta = 0.4\%$  and corresponds to a shift in  $M_s$  by 13 $^\circ\text{C}$  between region I and II.

The length of the modeled region is 150 $\mu\text{m}$  and the thickness of a characteristic segregation line ranges from 10-80 $\mu\text{m}$  depending on the volume fraction and region, which is about 1–2 times the grain size  $g$ . A segregation plane thickness of 50 $\mu\text{m}$  was modeled, which corresponds to a volume fraction  $\chi$  of 20%. First the thermal and subsequently the mechanical problem is solved using quadratic brick elements DC3D20 and C3D20 respectively.

#### 4.3.4 Microscopic model

A matrix cube with embedded inclusions of varying shape and aspect ratio serves as statistical RVE to calculate the residual stresses and the Young's modulus for different matrix carbon contents and precipitate volume fractions. The model is meshed with tetrahedral C3D10 elements of quadratic

shape functions with a coarse element size of  $0.2 \mu\text{m}$  on the outer surface compared to the cubes length of  $1 \mu\text{m}$ , and strong element refinement near the inclusions. The inclusions have randomly varying aspect ratios from 0.5-2 and a main axis length ranging from 40-70 nm. They are meshed with an element size of maximum 10 nm. Periodic boundary conditions are applied the free surfaces. First,(i) a uniaxial displacement is applied on the reference node to determine the Young's modulus  $E^{meso}$  for different carbon content and precipitate volume fraction  $\zeta$  and (ii) to determine the thermo-elastic residual stresses the reference point (RP) is unconstrained.

The microscopic residual stress formation as well as the ranking of different precipitate types is considered elastically below a temperature of  $0.4 T/T_M$  homologous temperature (about  $400^\circ\text{C}$ ) based on deformation mechanism maps in steel [18]. Above this temperature a stress free state is assumed and at cooling from  $400^\circ\text{C}$  to  $25^\circ\text{C}$  residual stresses start at a stress free state and form elastically. This thermo-elastic approach is a simplified measure and for a more precise analysis the crystallographic features and stress relaxation due to creep should be considered.

To calculate the thermo-elastic stresses a uniform temperature field is applied and the amplitude changed from a temperature of  $400^\circ\text{C}$  to RT. A Young's modulus  $E_I^{micro}$  for a matrix carbon content of 0.25 wt%C with  $\nu = 0.33$  and for the inclusions  $E_P^{micro} = 310 \text{ GPa}$  and  $\nu = 0.33$  are assumed, which is supposed to represent a mixture of Cr-rich cementite and Cr/Mo rich MC carbides, which have been shown to be relevant in similar alloys [19].

If a product is subsequently tempered, the macroscopic residual stresses fully relax at a temperature of  $700^\circ\text{C}$ . During cooling to room temperature microscopic and mesoscopic residual stresses form due to thermal misfits between the steel and precipitates.

Isotropic elastic properties  $E$  and  $\nu$  from literature are implemented as a starting value and the elastic properties for the precipitates are shown in table 4.1 for representative carbides, nitrides and oxides. The thermal expansion and elastic data to determine residual stress formation potential of different precipitate types, was mostly taken from first principle calculations and are- if available- average values from  $400^\circ\text{C}$  to  $25^\circ\text{C}$ . The resulting stresses in matrix and inclusion in the depleted region ( $i = I$ ) and the segregated region ( $i = II$ ) were calculated following [12], where for the assumption of spherical inclusions the average stress  $\bar{\sigma}_P$  is

$$\bar{\sigma}_P = \sigma_{11} = \sigma_{22} = \sigma_{33} = \frac{(\alpha_i - \alpha_P)\Delta T}{\frac{1}{3K_P} + \frac{1}{4(1-f)G_i} + \frac{\zeta}{3(1-f)K_i}} \quad (4.3)$$

where the subscript  $P$  denotes the inclusion properties and  $I, II$  the matrix. The average matrix stress  $\bar{\sigma}_{I,II}$  is

$$\bar{\sigma}_i = \frac{-\zeta\bar{\sigma}_P}{1 - \zeta} \quad (4.4)$$

**Table 4.1:** Elastic and thermal properties of a number of homogeneities in low-alloyed steel.

	$\alpha^a$ ( $10^{-6}K^{-1}$ )	B (GPa)	E (GPa)	G (GPa)	$\nu$ (-)	$\sigma_p$ (MPa)	$\sigma_m$ (MPa)
Al <sub>2</sub> O <sub>3</sub>	7.278 [20]	249 [21]	399 [21]	162 [21]	0.24*	-402.5	21.2
MgO	1.272 [20]	164 [21]	310 [21]	130 [21]	0.19*	351.0	-18.5
TiO	5.783 [22]	262 [23]	294*	112*	0.31*	-633.1	33.3
TiN	5.678 [24]	277*	459 [25]	188 [25]	0.22[25]	-658.7	34.7
TiC	4.918 [24]	242 [26]	474 [26]	187*	0.17*	-746.1	39.3
NbC	5.101 [25]	267 [26]	438 [26]	188*	0.23*	-739.3	38.9
VC	5.532 [25]	308 [26]	513 [26]	210*	0.22*	-699.3	36.8
MoC	6.507 [26]	328 [26]	410 [26]	159*	0.29*	-554.8	29.2
Mo <sub>2</sub> C	5.167 [27]	300 [26]	322 [26]	122*	0.32*	-751.6	39.6
Fe <sub>3</sub> C	9.583 [28]	224 [29]	242*	92 [29]	0.36*	-59.8	3.1
Cr <sub>7</sub> C <sub>3</sub>	6.958 [30]	312 [31]	226*	82*	0.38*	-477.5	25.1
BN	5.000 [32]	400 [33]	923*	414*	0.11*	-828.7	43.6
Fe	10.00[7]	174[7]	209*	80*	0.3[7]		

<sup>a</sup> If available, average value from 700 to 25°C

\* Calculated from cited literature values in the given reference.

## 4.4 Results

To get an elastically consistent mesoscopic model and macroscopic model the Young's moduli  $E_I^{meso}$  and  $E_{II}^{meso}$  ( $E_{I,II}^{meso}$ ) were calculated to give a macroscopic modulus of 209 GPa [7] for a segregation line volume fraction  $\chi = 20\%$  and precipitate volume fraction  $\zeta = 4\%$  in both depleted and segregated region.

In the unconstrained version of the mesoscopic model the martensite start temperature  $M_s$ , volume expansion  $\Delta V$  and thermal expansion  $\alpha$  are varied as a function of carbon content for a segregation line volume fraction  $\chi = 20\%$ . The residual stresses are shown in Fig. 4.8 over the local difference in  $M_s$ . In the case of pure martensite formation, the residual stresses increase with the difference in  $M_s$  and saturate at a constant level when transformation in region I and II do not proceed simultaneously anymore.

The mesoscopic submodel is subjected to the thermal and mechanical history and the results are shown in Fig. 4.7 (left) on the outer surface and (right) on the inner surface. On the outer surface the temperature decreases stepwise due to the setup of the cooling baskets, while on the inner surface it decreases continuously. These results match exactly the profiles published in [7] in Fig.3.7a. Due to the lower martensite start temperature  $M_s$  the transformation starts with a visible delay on the inner surface in the

segregation line (region II).

The total strain  $\varepsilon_1, \varepsilon_2$  and  $\varepsilon_3$ , where  $\varepsilon_3$  corresponds to the macroscopic tangential strain, are applied with a reference node and are constant over the investigated mesoscopic model since it is small compared to the tube's wall thickness. The depicted creep strain  $\varepsilon_3^{trip}$  represents the component of the transformation induced plasticity (TRIP) in direction 3. The TRIP strains  $\varepsilon_3^{trip}$  on the inner and outer surface differ, since the stress states during transformation vary.

Comparing the residual stress evolutions  $\sigma_3$  on the outer (point 1) and inner (point 2) surface reveal that the outer surface reaches residual stresses of  $-831$  MPa (I) to  $-873$  MPa (II) in tangential direction and the inner surface  $13$  MPa (I) to  $-50$  MPa (II), where (II) refers to the segregated area and (I) to the depleted area.

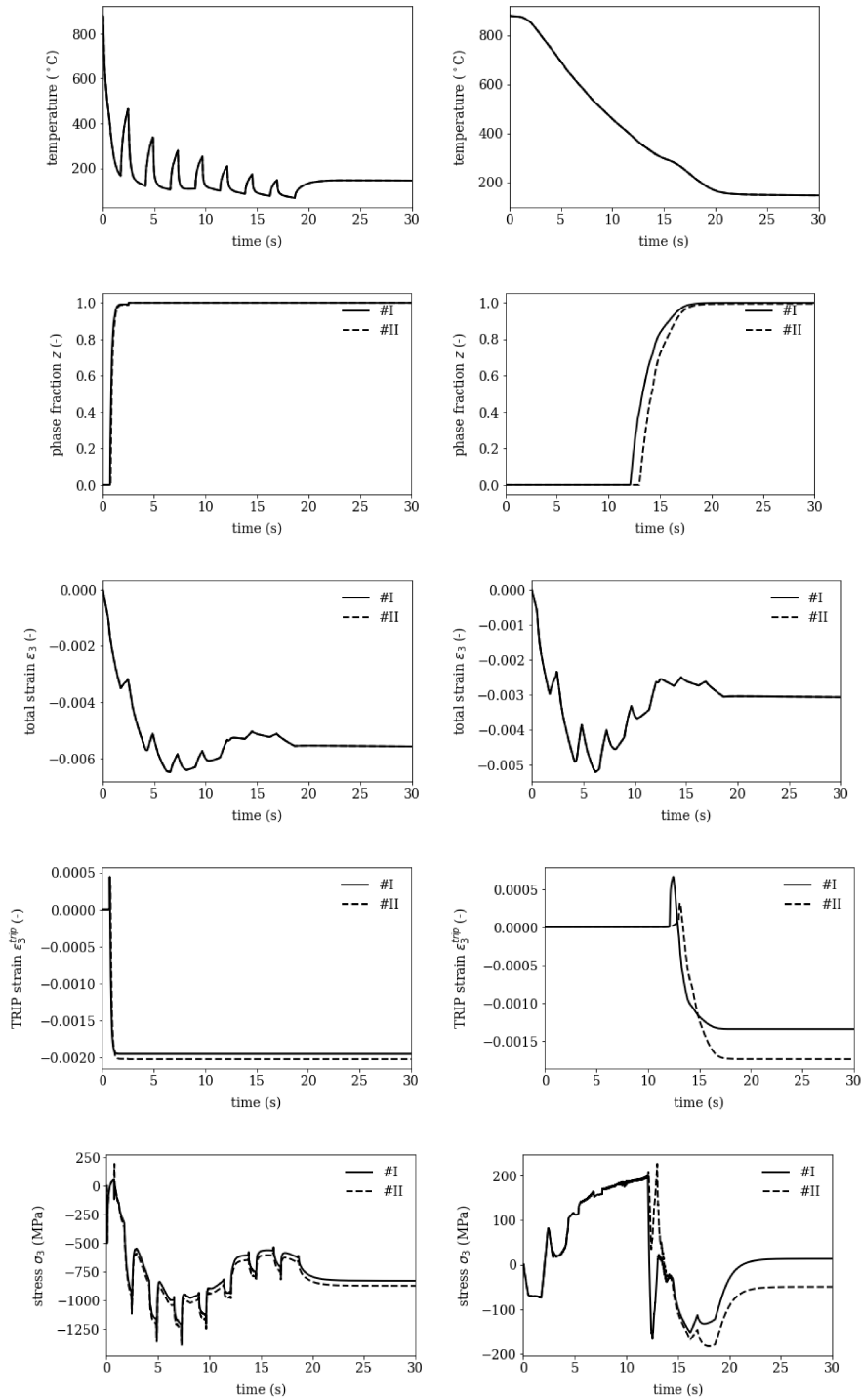
The absolute level of mesoscopic residual stresses matches the findings from the macroscopic calculations and measurements published in [7]- since the elastic values consistently chosen. The difference between the minimum and maximum values on the outer surface of  $42$  MPa and  $63$  MPa on the inner surface match with the values in Fig.4.8. This shows, that despite huge non-linearities during cooling and phase transformation the mesoscopic residual stresses are superimposed to the macroscopic stresses.

The relative stress formation potential (i.e. the average matrix stress  $\sigma_{m,avg}$  of different inclusion types is given for an arbitrary volume fraction  $\zeta$  of  $4\%$ , to get a relative comparison between the species in Fig. 4.9. Boron nitride BN shows the highest residual stress formation potential in steel based on thermo-elastic assumptions, followed by  $\text{Mo}_2\text{C}$ , TiC, NbC and VC. Cementite  $\text{Fe}_3\text{C}$  has a low residual and MgO could potentially cause voids, due to its larger thermal expansion compared to Fe.

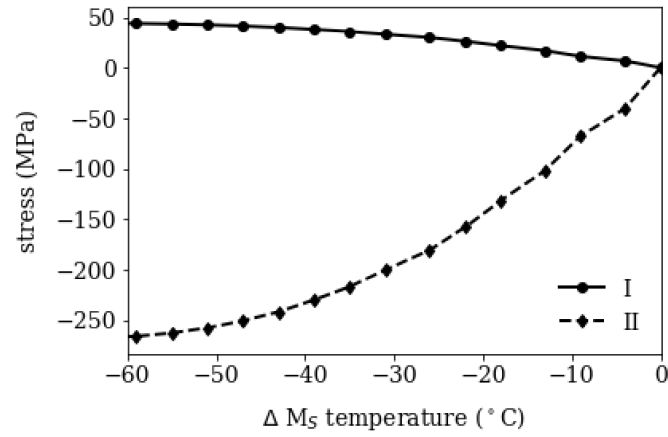
For Cr-rich inclusions the maximum principle stresses of RVE's with varying precipitate volume fractions  $\zeta$  are evaluated at the integration points. The results are shown in Fig. 4.10. and show a bimodal distribution. The first peak, is the most frequently occurring stress changing from  $15$  MPa to  $75$  MPa for volume fractions from  $1\%$  to  $5\%$ . It is of similar magnitude as the calculated average matrix stress in Fig. 4.9. The second peak is close to  $250$  MPa which occurs in the inclusion vicinity. The maximum values of range up to  $550$  MPa- they are mesh size dependent however, but similar mesh size was used to give a relative estimation however.

Figure 4.11 shows a summary of residual stress formation on macroscopic, mesoscopic and microscopic scale for quenched/ or accelerated cooling and tempered condition. Macroscopic stresses form during cooling due to plastic thermal misfits and phase transformation and are fully released after tempering at about  $700^\circ\text{C}$ , as has been experimentally shown in [34].

The mesoscopic stresses in the quenched state cause stresses and the tangential component (submodel direction 3) around a single segregation line of  $\leq \pm 75$  MPa with tensile stresses in the matrix is shown. After



**Figure 4.7:** Results of mesoscopic submodel for (left) a point on the outer surface and (right) a point on the inner surface: the temperature, phase fraction  $z$ , total strain in direction 3 (tangential direction in the macroscopic model), the TRIP strain and the resulting stress.



(a)

**Figure 4.8:** Residual stresses after cooling in depleted (I) and segregated (II) region for pure martensite as function of difference in martensite start temperature  $\Delta M_s$ .

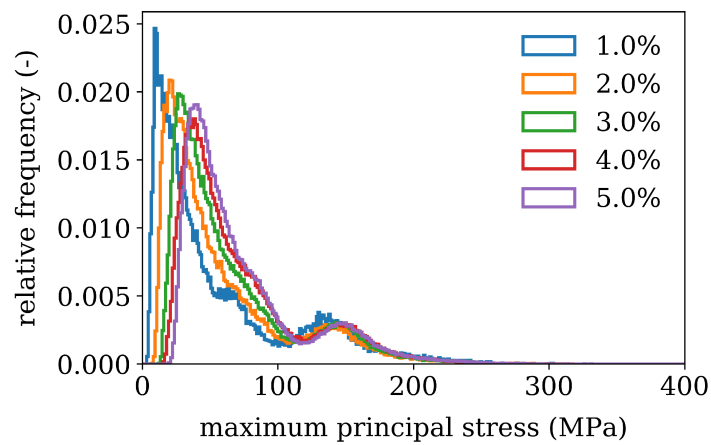


**Figure 4.9:** Histogram showing the maximum principle thermo-elastic stress after cooling for different precipitate volume contents  $\zeta$ .

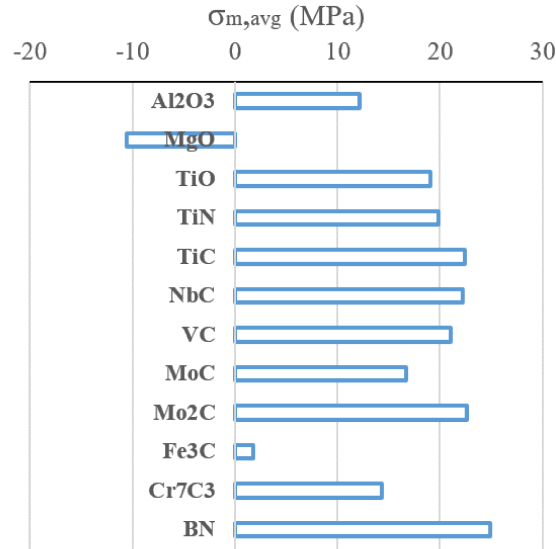


**Figure 4.10:** Residual stress formation potential in matrix for a volume content of  $\zeta = 4\%$  for relative comparison different inclusion types after [12].

tempering, with a thermal mismatch between the segregated and depleted region, stresses of  $\leq \pm 25$  MPa remain. The mesoscopic stresses act over wider ranges of micrometers, but are small in size. After tempering, the segregated region is in tensile stress regime, since the thermal expansion in this region is higher than in the depleted region (compare Fig. 4.6).

The microscopic stresses are higher compared to the mesoscopic ones and equilibrate over small distances  $\leq 0.5 \mu\text{m}$ , which is important since residual stresses only can act as crack opening force, if they act on a larger scale than the defect size is. The microscopic stresses depend on the precipitate volume fractions, which may increase during tempering and the occurring precipitate types. The depicted results show the maximum principal stress along a path cutting through the microscopic model with 1% precipitate volume fraction (left) and 5% volume fraction (right) and show the compressive stress state within the precipitates and tensile stresses in the matrix.

## 4.5 Summary and conclusions

The residual stress formation in low-alloyed seamless steel tubes during accelerated cooling was investigated. A mesoscopic submodel on the tube's inner and outer surface, reveals that regardless of many nonlinearities (phase transformation, plasticity, TRIP,..) the mesoscopic residual stresses due to interdendritic segregation appear superimposed to the macroscopic level.

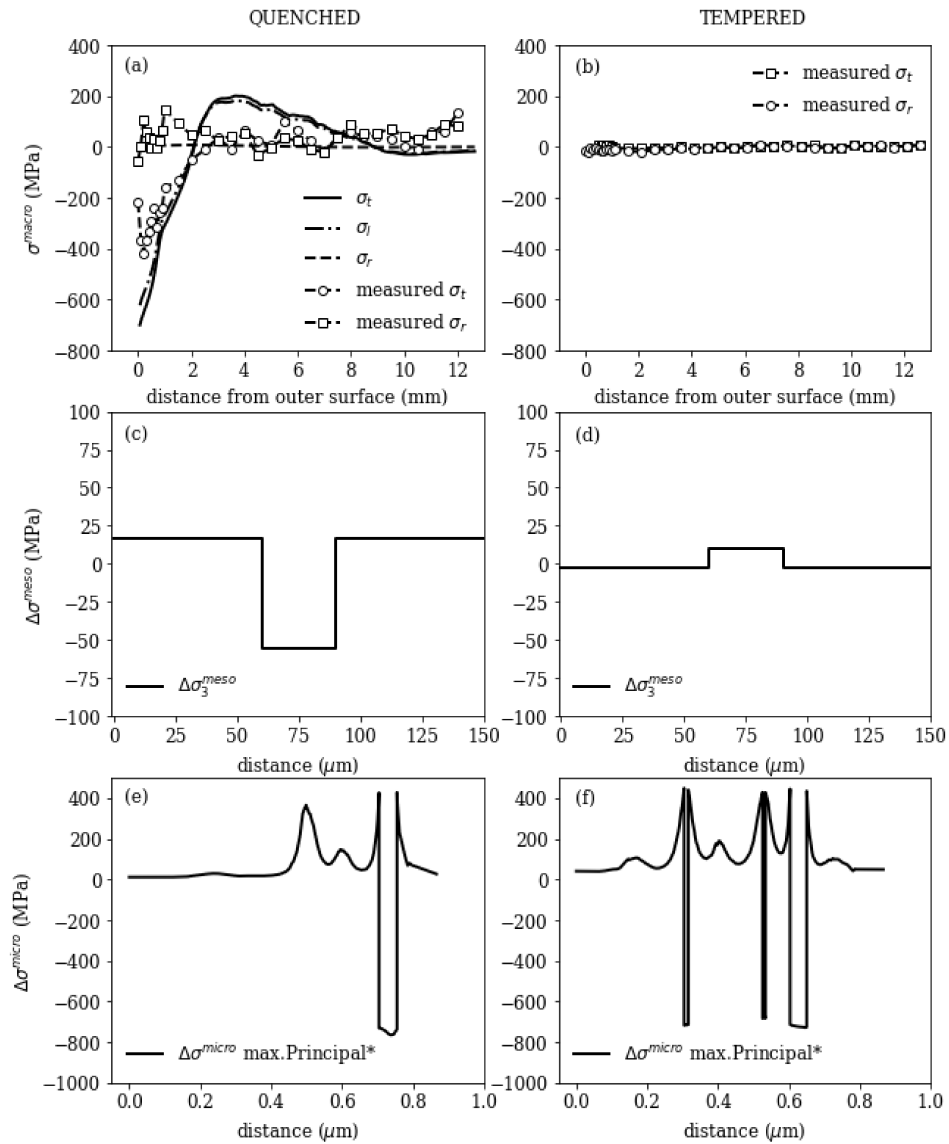


**Figure 4.11:** Macroscopic, mesoscopic and microscopic residual stresses for quenched (left) and tempered state (right).



Thus, considering the mesoscopic model in an unconstrained way to evaluate the effect of carbon content and composition is correct.

A mechanically unconstrained, independent mesoscopic model is employed to investigate the residual stresses in segregated areas and depleted areas as function of carbon content. For cooling rates provoking only martensite, the residual stresses saturate after a certain difference in  $M_s$  in the segregation line and depleted region. When bainite is formed in the segregated area, the residual stresses decrease again after reaching a maximum value.

Mesoscopic and microscopic residual stresses, are investigated using both a representative volume element (RVE) and an averaging approach. With the RVE, the maximum principal thermo-elastic residual stresses for cubical models containing different volume fraction of inclusions, are investigated. The most frequent stress correlates with the calculated thermo-elastic average matrix stress and ranges from 10 to 70 MPa. A selection of inclusions is ranked by the average matrix stress, which they cause for a given arbitrary volume fraction. It turns out, that BN shows the highest relative residual stress formation potential, followed by  $\text{Mo}_2\text{C}$ , TiC, NbC and VC.

# Bibliography

- [1] I. I. Kudish and K. W. Burris. Modern state of experimentation and modeling in contact fatigue phenomenon: Part I—contact fatigue. Normal and tangential contact and residual stresses. Nonmetallic inclusions and lubricant contamination. Crack initiation and crack propagation. Surface an. *Tribology Transactions*, 43(2):187–196, 2000. ISSN 1547397X. doi: 10.1080/10402000008982328.
- [2] E. Dabah, T. Kannengiesser, D. Eliezer, and T. Boellinghaus. Hydrogen interaction with residual stresses in steel studied by synchrotron X-ray diffraction. *Materials Science Forum*, 772:91–95, 2014. ISSN 02555476. doi: 10.4028/www.scientific.net/MSF.772.91.
- [3] P. J. Bouchard and P. J. Withers. The appropriateness of residual stress length scales in structural integrity. *Journal of Neutron Research*, 12(1-3):81–91, 2004. ISSN 14772655. doi: 10.1080/10238160410001734504.
- [4] F. G. Rammerstorfer, A. F. Plankensteiner, F. D. Fischer, and T. Antretter. Hierarchical models for simulating the mechanical behavior of heterogeneous materials : an approach to high speed tool steel 1. 259:73–84, 1999.
- [5] D. Golanski, K. Terada, and N. Kikuchi. Macro and micro scale modeling of thermal residual stresses in metal matrix composite surface layers by the homogenization method. 19:188–202, 1997.
- [6] X. X. Zhang, B. L. Xiao, H. Andrä, and Z. Y. Ma. Multiscale modeling of macroscopic and microscopic residual stresses in metal matrix composites using 3D realistic digital microstructure models. 137:18–32, 2016. doi: 10.1016/j.compstruct.2015.10.045.
- [7] S. Brunbauer, G. Winter, T. Antretter, P. Staron, and W. Ecker. Residual stress and microstructure evolution in steel tubes for different cooling conditions – Simulation and verification. *Materials Science and Engineering A*, 747:73–79, 2019. ISSN 09215093. doi: 10.1016/j.msea.2019.01.037. URL <https://doi.org/10.1016/j.msea.2019.01.037>.

- [8] S. Leitner, G. Winter, J. Klarner, T. Antretter, and W. Ecker. Model-Based Residual Stress Design in Multiphase Seamless Steel Tubes. *Materials*, 13(2):439, jan 2020. ISSN 1996-1944. doi: 10.3390/ma13020439. URL <https://www.mdpi.com/1996-1944/13/2/439>.
- [9] P. J. Withers and H. K.D.H. Bhadeshia. Residual stress part 1 - Measurement techniques. *Materials Science and Technology*, 17(4):355–365, 2001. ISSN 02670836. doi: 10.1179/026708301101509980.
- [10] T. Siwecki, T. Koziel, W. B. Hutchinson, and P. Hansson. Effect of Micro-Segregation on Phase Transformation and Residual Stress. *Materials Science Forum*, 539-543:4596–4601, mar 2007. ISSN 1662-9752. doi: 10.4028/www.scientific.net/MSF.539-543.4596. URL <http://www.tms.org/Superalloys/10.7449/2004/Superalloys{ }2004{ }537{ }543.pdf><https://www.scientific.net/MSF.539-543.4596>.
- [11] J. Douin, P. Donnadieu, and F. Houdellier. Elastic strain around needle-shaped particles embedded in Al matrix. *Acta Materialia*, 58(17):5782–5788, 2010. ISSN 13596454. doi: 10.1016/j.actamat.2010.06.053. URL <http://dx.doi.org/10.1016/j.actamat.2010.06.053>.
- [12] C. Hsueh and P. F. Becher. Residual thermal stresses in ceramic composites. Part I: with ellipsoidal inclusions. *Materials Science and Engineering: A*, 212(1):22–28, jul 1996. ISSN 09215093. doi: 10.1016/0921-5093(96)10176-3. URL <https://linkinghub.elsevier.com/retrieve/pii/0921509396101763>.
- [13] Dassault Systems. Abaqus standard. URL <https://www.3ds.com/products-services/simulia/products/abaqus/abaqusstandard/>.
- [14] S. M.C. Van Bohemen. Bainite and martensite start temperature calculated with exponential carbon dependence. *Materials Science and Technology*, 28(4):487–495, 2012. ISSN 02670836. doi: 10.1179/1743284711Y.0000000097.
- [15] J. M. Moyer and G. S. Ansell. The volume expansion accompanying the martensite transformation in iron-carbon alloys. *Metallurgical Transactions A*, 6(9):1785–1791, sep 1975. ISSN 0360-2133. doi: 10.1007/BF02642308. URL <http://link.springer.com/10.1007/BF02642308>.
- [16] M. Souissi and H. Numakura. Elastic properties of Fe-C and Fe-N martensites. *ISIJ International*, 55(7):1512–1521, 2015. ISSN 09151559. doi: 10.2355/isijinternational.55.1512.

- [17] Sente Software Ltd. Jmatpro. URL <https://www.sentesoftware.co.uk/jmatpro>.
- [18] H. J. Frost and M. F. Ashby. Deformation-Mechanism Maps for Pure Iron, Two Austenitic Stainless Steels, and a Low-Alloy Ferritic Steel. *Fundamental Aspects of Structural Alloy Design*, pages 27–65, 1977. doi: 10.1007/978-1-4684-2421-8\_2.
- [19] S. Zamberger, T. Wojcik, J. Klarner, G. Klösch, H. Schifferl, and E. Kozeschnik. Computational and experimental analysis of carbonitride precipitation in tempered martensite. *Steel Research International*, 84(1):20–30, 2013. ISSN 16113683. doi: 10.1002/srin.201200047.
- [20] R. Reeber, R. and K. Wang. Lattice Parameters and Thermal Expansion of Important Semiconductors and Their Substrates. *Mat. Res. Soc. Symp. Proc. Vol. 614*, Materials Research Society, 614:1–12, 2000.
- [21] N. Soga and O. L. Anderson. High-Temperature Elastic Properties of Polycrystalline MgO and Al<sub>2</sub>O<sub>3</sub>. *Journal of the American Ceramic Society*, 49(7):355–359, 1966. ISSN 15512916. doi: 10.1111/j.1151-2916.1966.tb13283.x.
- [22] D. R. Hummer, P. J. Heaney, and J. E. Post. Thermal expansion of anatase and rutile between 300 and 575 K using synchrotron powder X-ray diffraction. *Powder Diffraction*, 22(4):352–357, 2007. ISSN 0885-7156. doi: 10.1154/1.2790965.
- [23] E. Shojaei and M. R. Mohammadzadeh. First-principles elastic and thermal properties of TiO<sub>2</sub>: A phonon approach. *Journal of Physics Condensed Matter*, 22(1), 2010. ISSN 09538984. doi: 10.1088/0953-8984/22/1/015401.
- [24] J. Kim and S. Kang. Elastic and thermo-physical properties of TiC, TiN, and their intermediate composition alloys using ab initio calculations. *Journal of Alloys and Compounds*, 528:20–27, 2012. ISSN 09258388. doi: 10.1016/j.jallcom.2012.02.124. URL <http://dx.doi.org/10.1016/j.jallcom.2012.02.124>.
- [25] W. Wolf, R. Podlucky, T. Antretter, and F. D. Fischer. First-principles study of elastic and thermal properties of refractory carbides and nitrides. *Philosophical Magazine B: Physics of Condensed Matter; Statistical Mechanics, Electronic, Optical and Magnetic Properties*, 79(6): 839–858, 1999. ISSN 13642812. doi: 10.1080/13642819908214844.
- [26] V. Krasnenko and M. G. Brik. First-principles calculations of hydrostatic pressure effects on the structural, elastic and thermodynamic properties of cubic monocarbides XC (X = Ti, V, Cr, Nb, Mo,

- Hf). *Solid State Sciences*, 14(10):1431–1444, 2012. ISSN 12932558. doi: 10.1016/j.solidstatesciences.2012.08.007. URL <http://dx.doi.org/10.1016/j.solidstatesciences.2012.08.007>.
- [27] B. Lönnberg. Thermal expansion studies on the subcarbides of group V and VI transition metals. *Journal of The Less-Common Metals*, 120(1):135–146, 1986. ISSN 00225088. doi: 10.1016/0022-5088(86)90635-1. URL <http://www.sciencedirect.com/science/article/pii/0022508886906351>.
- [28] I. G. Wood, L. Vočadlo, K. S. Knight, David P. Dobson, W. G. Marshall, G. David Price, and John Brodholt. Thermal expansion and crystal structure of cementite, Fe<sub>3</sub>C, between 4 and 600 K determined by time-of-flight neutron powder diffraction. *Journal of Applied Crystallography*, 37(1):82–90, 2004. ISSN 00218898. doi: 10.1107/S0021889803024695.
- [29] M. Nikolussi, S. L. Shang, T. Gressmann, A. Leineweber, E. J. Mittemeijer, Y. Wang, and Z. K. Liu. Extreme elastic anisotropy of cementite, Fe<sub>3</sub>C: First-principles calculations and experimental evidence. *Scripta Materialia*, 59(8):814–817, 2008. ISSN 13596462. doi: 10.1016/j.scriptamat.2008.06.015.
- [30] X. Y. Chong, Y. H. Jiang, R. Zhou, and J. Feng. Multialloying effect on thermophysical properties of Cr<sub>7</sub>C<sub>3</sub>-type carbides. *Journal of the American Ceramic Society*, 100(4):1588–1597, 2017. ISSN 15512916. doi: 10.1111/jace.14694.
- [31] Y. Liu, Y. Jiang, and R. Zhou. First-principles study on stability and mechanical properties of Cr<sub>7</sub>C<sub>3</sub>. *Xiyou Jinshu Cailiao Yu Gongcheng/Rare Metal Materials and Engineering*, 43(12):2903–2907, 2014. ISSN 1002185X. doi: 10.1016/s1875-5372(15)60030-3. URL [http://dx.doi.org/10.1016/s1875-5372\(15\)60030-3](http://dx.doi.org/10.1016/s1875-5372(15)60030-3).
- [32] D. S. Williams. Elastic stiffness and thermal expansion coefficient of boron nitride films. *Journal of Applied Physics*, 57(6):2340–2342, 1985. ISSN 00218979. doi: 10.1063/1.334341.
- [33] M. Grimsditch, E. S. Zouboulis, and A. Polian. Elastic constants of boron nitride. *Journal of Applied Physics*, 76(2):832–834, 1994. ISSN 00218979. doi: 10.1063/1.357757.
- [34] S. Brunbauer, J. Klarner, R. Sonnleitner, W. Ecker, and G. Winter. Steel concepts and manufacturing processes for optimized performance properties of seamless steel tubulars. *NACE International, 2nd Conference and Expo Genoa 2018*, 2018.

## Chapter 5

### Publication 4

*Numerical analysis of shape, orientation and interface properties of  $\text{Mo}_2\text{C}$  precipitates in iron*

Unpublished manuscript.

## Numerical analysis of shape, orientation and interface properties of Mo<sub>2</sub>C precipitates in iron

### Authors

Silvia Leitner<sup>1</sup>, Daniel Scheiber<sup>1\*</sup>, Thomas Dengg<sup>1</sup>, Jürgen Spitaler<sup>1</sup>,  
Thomas Antretter<sup>2</sup>, Werner Ecker<sup>1</sup>

<sup>1</sup>Materials Center Leoben Forschung GmbH, Roseggerstraße 12,  
Leoben, 8700, Austria

<sup>2</sup>Institute of Mechanics, Montanuniversität Leoben, Franz Josef Strasse  
18,  
Leoben, 8700, Austria

\*corresponding author: daniel.scheiber@mcl.at

submitted, accepted, published

### *Highlights*

- shape and aspect ratio prediction of Mo<sub>2</sub>C precipitates from first principles and finite element method
- anisotropic Mo<sub>2</sub>C-Fe interface information from first principles
- quantitative total energy balance for coherent state, considering thermal effects

### *Keywords*

Precipitate; Interface; DFT; Finite Element method; Mo<sub>2</sub>C; Morphology; Energy; Elasticity; ...

## 5.1 Abstract

Precipitation is a key factor in material design and engineering, as it can alter or deteriorate many material properties. To explore its full capabilities, detailed understanding of precipitate formation, structure and interaction with the matrix is essential. While currently most theoretical studies focus on micro to macro-scale treatment of precipitation, gaining insight into atomic interaction of matrix and precipitate is essential for knowledge driven material design. With the increasing computational power, atomic-scale investigation of local details of the precipitates' interface is within reach. Combining this approach with the finite element method allows investigating the reasons for precipitate shape, orientation, their interface properties and residual stresses.

In the current study, we exemplarily study the  $\text{Mo}_2\text{C}$  precipitate, a carbide commonly used for secondary hardening in steels, and its interface to the Fe matrix using ab-initio density functional theory.  $\text{Mo}_2\text{C}$  is reported to form needles nucleated at dislocations and oriented with their prolate axis in  $\langle 100_{bcc} \rangle$  directions. The known orientation relationship determines the possible coherent and incoherent interfaces, of which three configurations are chosen. By applying the stress-balancing method and the gamma-surface approach, the ground state structures of the interfaces are determined at the tip and for two orientations at the long side of the needle. Quantifying the interface energies for different orientations in coherent and incoherent state shows, that the needle tip in fact shows a higher interface energy than selected interfaces on the long side.

The anisotropic interface energy integrated over the precipitate's surface is compared with numerical finite element simulations accessing the mechanical strain energy of the volumetric lattice expansion during formation. Based on the computed interface energies and strain energy contribution, the specific needle-shaped structure of the precipitate can be explained. A simplified elastic approach is compared with a case that also considers creep.

Considering only the interface anisotropy yields a predicted aspect ratio of 1.6. Considering interface energy and purely elastic strain energy disregarding creep contributions, the aspect ratio of minimum energy would be 5. Considering the effect of creep in the matrix, reveals that the mechanical contribution becomes negligible and the interface energy dominates.

For a selected interface, the full elastic properties are determined and compared to the Grimsditch-Nizzoli approach, where we find good agreement. Our study shows how a combination of the ab-initio and the finite element method may be used to characterize and understand the micro-mechanical effects of precipitates.



## 5.2 Introduction

Considerable effort has been dedicated to understanding the mechanisms of precipitate formation, structure, and their interaction with the matrix, as for Mo<sub>2</sub>C carbides. The precipitate shape, size and positions are of great interest due to their impact on the overall mechanical properties. During formation, shape, size and growth rates of precipitates are determined by the volumetric free energy, the interface energy and the strain energy. These energy contributions depend on the interaction between matrix and precipitate. Coherency, size and interface energies also affect the interaction of precipitates with dislocations and therefore their strengthening contribution. It is necessary to understand these processes to use precipitation as a key factor to design material properties.

The Mo<sub>2</sub>C carbide obeys the Pitsch-Schrader orientation relationship with the surrounding Fe matrix, which describes an alignment of a hexagonal close packed (hcp) with a body centered cubic (bcc) crystal structure [1, 2, 3]. In this respect it is worth noting that Mo<sub>2</sub>C exhibits a hcp structure only above 1600 K and below that temperature the crystal structure is orthorhombic (pseudo-hexagonal)  $\alpha$ -Mo<sub>2</sub>C and belongs to space group 60 Pbcn [4]. Shi [5] reported that small systematic deviations up to 5.5° from the Pitsch-Schrader relationship can exist and that near the needle tip Mo seems to be substituted by Fe, while in the center of the particle the carbide is essentially Fe-free. For our calculations we assume for the sake of simplicity pure Mo<sub>2</sub>C in the precipitate and pure Fe in the matrix.

A characteristic feature of Mo<sub>2</sub>C carbides is their shape, i.e. they are needle like with the prolate axis in  $\langle 100 \rangle$  direction of the Fe matrix [1, 2, 5]. These studies focusing on precipitation kinetics and orientation use TEM SANS and gain insight into the resulting growth rates, size distributions and aspect ratios but cannot get insight as to why a certain orientation is preferred. The reason for the observed orientation relationship and shape of the carbides has not been discussed yet in literature.

Insights to mechanisms from atomistic modeling gives a better understanding in addition to experimental work and has been successfully applied in many cases; Janisch et al. [6] showed how precipitation may lead to grain boundary embrittlement in Mo. Fors et al. [7, 8] studied the precipitate stability of various carbides and nitrides in Fe and Sawada et al. [9] investigated the transition from coherent to semi-coherent Nb-C precipitates using first principles. A recent work by DiStefano et al. [10] focused on H trapping at TiC precipitates, which could explain the large spread of trapping energies observed in experiments. These findings from atomistic scale are vital for an accurate description of precipitates and are hardly accessible by other methods.

The experimentally observed aspect ratios for Mo<sub>2</sub> carbide in Fe range from 2 to 4, reported by [2] for tempering up to 100 h at 510°C. The length-

ening was investigated by Hall [11] at 600°C for tempering up to 24 h and reported precipitate lengths of 80 nm with an aspect ratio of 7. Yamasaki and Bhadeshia [3] modeled the precipitation of Mo<sub>2</sub>C in iron and found beginning Oswald ripening at an average length of 70-80 nm. Based on these observations we calculate the energy balance for a Mo<sub>2</sub>C precipitate in Fe at a temperature of 600°C with a fixed volume of 5500 nm<sup>3</sup> (which corresponds to a length of 80 nm and an aspect ratio of 7).

We couple atomistic scale first principle methods with macroscopic scale finite element (FE) methods to get a quantitative energy balance for Mo<sub>2</sub>C embedded in a bcc iron matrix at 600°C and a realistic inclusion volume. We do not consider the precipitate growth kinetics, but the energy balance of a coherent and incoherent precipitate for different orientations and aspect ratios at constant volume to investigate why certain cases are favored. To this end, volume expansion of Mo<sub>2</sub>C, temperature dependence of elastic constants for Fe and Mo<sub>2</sub>C, and interface energies are computed using first principles and then serve as input for finite element (FE) simulations of the precipitate in a matrix by means of a continuum mechanical approach. We find energetic reasons for the specific orientation relationship as well as for the preferred needle like shape of the precipitate by combining of the interface and mechanical aspects.

### 5.3 Computational Details and Methodology

In the following section we present the methods for calculating the thermal, elastic and interface properties of Mo<sub>2</sub>C and Fe and the strain energy contributions. It is assumed that for an early precipitation state the Mo<sub>2</sub>C-Fe interface is coherent, which is in agreement with experimental data. To this end, three distinct positions of the ellipsoid's surface are selected. Then we calculate the interface energies, work of separation and elastic interface properties using Density-functional theory (DFT). The interface energies are calculated for an incoherent interface and compared to the coherent case.

Subsequently, we use a FE model to calculate the strain energy contributions for different orientations and aspect ratios at constant volume. The formation of a precipitate is accompanied by a considerable volumetric lattice expansion. For the macroscopic strain energy we take the volumetric lattice expansion, i.e. the 'stress free eigenstrain', which the inhomogeneity is subjected to, according to Allen and coworkers [2]. To determine the strain energy contribution in the total energy balance the results of a simplified elastic model are compared with a model considering creep, which is likely to occur at the given precipitate formation temperature.

Combining interface energy contribution from first principles and the strain energy contribution from finite element analysis yields the total energy balance which is evaluated at different aspect ratios and orientations in order

to determine the energetically most favorable configurations.

### 5.3.1 DFT simulations

The ab-initio simulations in this study were performed using density functional theory (DFT) as implemented in the Vienna Ab-initio Simulation Package (VASP) [12, 13, 14, 15] with projector augmented wave functions (PAWs). For the xc functional, the implementation by Perdew, Burke, and Ernzerhof (PBE) [16, 17] was employed. The potentials for the elements were taken from the VASP recommendations, i.e. C was treated with four, Fe with eight, and Mo with twelve electrons in the valence. The temperatures of interest for this study are always below the Curie point of Fe and, therefore, Fe was considered in its ferromagnetic state. The energy cut-off for the interface and surface calculations was 400 eV and k-point density for all cells was set as close as possible to 36 points  $\times$   $\text{\AA}$ .

Phonons are calculated using the small displacements method where the computational framework for pre- and post-processing is provided by the *phonopy* [18] package. Here, a supercell size of  $3 \times 2 \times 2$  in a, b and c directions was used, respectively. For the Brillouin zone integration, a  $40 \times 40 \times 40$   $q$ -point mesh was used.

### Elastic constants

In order to obtain the elastic constants, the so called energy approach was used as implemented in the python package ThermElpy [19, 20], which serves as a toolkit for pre- and post-processing of DFT data. The toolkit automatically analyzes a given crystal structure in terms of its symmetries and identifies appropriate symmetry-inequivalent deformation types. For each of these deformation types, 21 distorted structures are generated in the range of -5% to 5% Lagrangian strain and their total energy is calculated using VASP. The elastic constants are then obtained by fitting the total energy-strain curves using polynomials and taking the second derivatives with respect to strain. Using Voigt notation, this reads:

$$C_{ij} = \frac{1}{V} \left. \frac{\partial^2 E}{\partial \eta_i \partial \eta_j} \right|_{\eta=0}, \quad (5.1)$$

where  $\eta_i$  denotes the Lagrangian strain in Cartesian direction  $i$ . Special care is taken also to choose the best fitting polynomial and data range using descriptors like the cross validation score [19, 20].

### Thermal expansion

The coefficient of thermal expansion (CTE) is calculated using the quasi-harmonic approximation [21]. Starting from the 0K equilibrium volume, the

cell is expanded and atomic positions and cell shape are relaxed. Then, for each volume the free energy as a function of temperature is determined from the inner energy and the vibrational free energy. The equilibrium volume for each temperature is determined by calculating the minimum of the free energy vs. volume for that temperature from 0 to 1000K. The volumetric CTE is then calculated using finite differences according to

$$\alpha_V = \frac{1}{V_0} \frac{\Delta V}{\Delta T}. \quad (5.2)$$

### Temperature dependence of elastic constants

To calculate the temperature dependence of elastic constants, first the volume thermal expansion of the solid  $V(T)$  is obtained as described in Section 5.3.1. Then, elastic constants are computed for a range of different volumes  $V$ . The volume dependent elastic constants are then fitted using a polynomial of third order to get a smooth function  $C_{ij}(V)$ . Finally, the elastic constants for a given temperature are obtained by taking the elastic constants for the equilibrium volume of this temperature, i.e.  $C_{ij}(T) = C_{ij}(V(T))$ .

### Calculation of interface properties

As a prerequisite for the interface simulations, the surface energies of Fe and Mo<sub>2</sub>C are computed. We consider Mo-rich conditions in this study. The surface energy of Mo<sub>2</sub>C is computed using

$$\gamma_{Mo_2C} = (E_{Mo_2C} - \mu_{Mo_2C}N_{Mo_2C} - \mu_{Mo}(2N_C - N_{Mo}))/2A. \quad (5.3)$$

where  $E_{Mo_2C}$  denotes the total energy of a cell containing a Mo<sub>2</sub>C slab with area  $A$ . It is important that the termination<sup>1</sup> on both sides of the slab is the same. The chemical potentials  $\mu_{Mo_2C}$  and  $\mu_{Mo}$  are obtained from the total energy per structural unit of the corresponding ground state structures and are given per structural unit, i.e. per atom for Mo, and for a unit of two Mo atoms and one C atom in the case of Mo<sub>2</sub>C.  $N_x$  denotes the number of structural units for  $x$  in the cell. The structures used for the simulation of Mo<sub>2</sub>C are shown in section 5.6, Fig. 5.14.

For Mo<sub>2</sub>C, the computation of surface energies is more complicated as for Fe because it is not always possible to construct stoichiometric slabs with the same surface termination on both sides of the slab. The equation for the surface energy of Fe simplifies to

$$\gamma_{Fe} = (E_{Fe} - \mu_{Fe}N_{Fe})/2A. \quad (5.4)$$

---

<sup>1</sup>Termination denotes the atomic configuration at the interfaces and free surfaces.

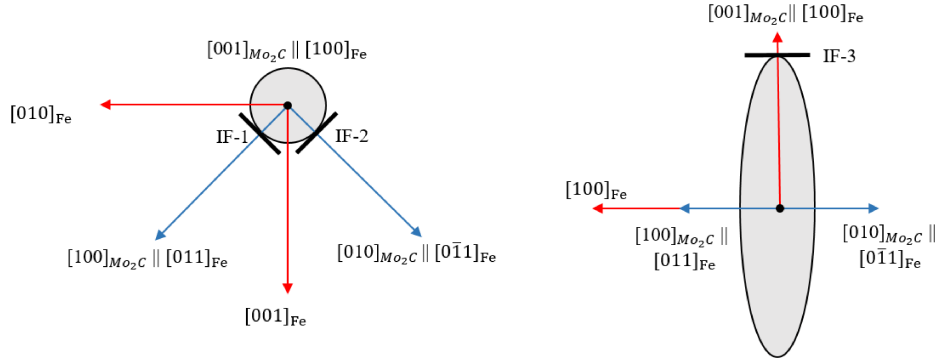


**Figure 5.1:** Modelled interfaces IF-1, IF-2 and IF-3.

**Table 5.1:** The Fe and Mo<sub>2</sub>C slabs constituting the interfaces given by a x b x c, where a and b span the interface plane and c is normal to the interface.

	Mo <sub>2</sub> C	Fe	# of atoms
	$l_1 \times l_2 \times l_3$	$l_1 \times l_2 \times l_3$	
Interface 1	[001]x[020]x[500]	[200]x[0-33]x[066]	264
Interface 2	[001]x[100]x[030]	[200]x[011]x[0-55]	76
Interface 3	[100]x[020]x[004]	[011]x[0-33]x[800]	192

The Mo<sub>2</sub>C precipitates obey the Pitsch-Schrader orientation relationship [1, 2, 3], which describes an alignment between a bcc and a hcp material. It is clear that Fe takes the place of the bcc material. For the pseudohexagonal orthorhombic Mo<sub>2</sub>C we have adapted the relationship such that [100]<sub>Fe</sub> is parallel to [001]<sub>Mo<sub>2</sub>C</sub>, [011]<sub>Fe</sub> is parallel to [100]<sub>Mo<sub>2</sub>C</sub>, and [01-1]<sub>Fe</sub> is parallel to [010]<sub>Mo<sub>2</sub>C</sub>, see also Fig. 5.1.

What still needs to be determined for the interface construction is the interface plane orientation. We chose three different orientations to characterize the Mo<sub>2</sub>C-Fe interface normal to all three Cartesian axes such that they are parallel to the planes terminating the unit cell of Mo<sub>2</sub>C. See Tab. 5.1 for the orientations and the corresponding dimensions.

The equilibrium strain state of an interface is a result of the elastic properties of the two adjoined slabs, which are encoded in the respective elastic constants. By applying the stress balancing methodology [22], which uses the elastic tensors from Section 5.4.1, the strain energy of the two slabs is minimized and the ideal cell is found. In Table 5.5 the strains resulting from the chosen dimensions are listed.

An interface is represented here by its energy, i.e. the energy needed to form the interface. The work of [23] shows how interface energy can determine the shape of particles. For an interface between a Fe slab and

and a Mo<sub>2</sub>C slab with vacuum on top, the interface energy is given by

$$\gamma_I = (E_I - \mu_{Fe}^s N_{Fe} - \mu_{Mo_2C}^s N_{Mo_2C} - \mu_{Mo}(2N_C - N_{Mo}))/A - \gamma_{Fe}^s - \gamma_{Mo_2C}^s. \quad (5.5)$$

In this equation,  $E_I$  denotes the total energy of the interface cell with interface area  $A$ . In analogy to the surface energy (Eq. 5.3), the chemical potentials  $\mu_{Fe}^s$ ,  $\mu_{Mo_2C}^s$ , and  $\mu_{Mo}^s$  are obtained from the corresponding ground state structures and are given per structural unit. Due to the vacuum on top and bottom of the interface structure, the cell (i.e. the combination of Mo<sub>2</sub>C and Fe lattice) with the carbide-matrix interface also contains two free surfaces: a Fe surface and a Mo<sub>2</sub>C surface, and the corresponding energies ( $\gamma_{Fe}^s$  and  $\gamma_{Mo_2C}^s$ ) have to be subtracted. The chemical potentials and the surface energies are obtained from cells strained by the same amount as the interface cell (denoted by the superscript  $s$ ). Thus, the elastic energies of the strained cell cancels out and the interface energy only remains.

Another characteristic of an interface is the work of separation, which quantifies the work needed to separate a given interface. It is defined as

$$W_{sep} = \gamma_{Fe} + \gamma_{Mo_2C} - \gamma_I. \quad (5.6)$$

The surface energies  $\gamma_{Fe}$  and  $\gamma_{Mo_2C}$  correspond to the surface energies of the surfaces created when separating the interface.

### 5.3.2 Energy contributions

This section addresses the comparison of mechanical and interface energy contributions caused by a Mo<sub>2</sub>C precipitate embedded in a Fe matrix during isothermal formation. For the mechanical energy contributions we use a continuum approach. The lattice expansion, which an inclusion volume is subjected to when forming Mo<sub>2</sub>C, is taken from Allen [2] and is denoted  $\epsilon^{vol}$ , i.e. the assumed "stress free eigenstrain". The hexagonal structure proposed by [2] was adapted accordingly to our orthorhombic notation.

$$\epsilon^{vol} = \begin{bmatrix} 0.003484 & 0.0 & 0.0 \\ & 0.229 & 0.0 \\ & sym. & 0.1136 \end{bmatrix} \quad (5.7)$$

This eigenstrain is applied to the Mo<sub>2</sub>C inhomogeneity embedded in the Fe matrix and resulting the strain energies are calculated for different aspect ratios and orientations. Due to the considerable magnitude of the eigenstrain, a purely elastic analysis will overestimate stresses and a case considering creep is calculated at formation temperature. At 600°C matrix creep is activated in the matrix and dissipates strain energy. An elastic approximation must thus be seen as simplification.

When plastic dissipation appears in either matrix or inhomogeneity an energy minimization is not adequate anymore and other extremizing principles may be used, as pointed out by [24]<sup>2</sup>.

But since we consider only a monotonic loading path and no unloading, creep can be mimicked by a non-linear, rate dependent elasticity and thus we may minimize the total energy  $E_t$  as the sum of

$$E_t = E_{IF} + E_{el} + E_{cr}, \quad (5.8)$$

where  $E_{el}$  denotes the elastic,  $E_{cr}$  the creep (later summarize as strain energy contribution  $E_{mech}$ ) and  $E_{IF}$  is the interface energy contribution.

The interface energy contribution  $E_{IF}$  is calculated by numerical integration over the ellipsoid's surface for different orientations

$$E_{IF} = \int_0^{2\pi} \int_0^{\pi} |\mathbf{x}_n^{IF}| d\varphi d\theta. \quad (5.9)$$

Here

$$\mathbf{x}_n^{IF} = \mathbf{R}\mathbf{\Gamma}\mathbf{R}^{-1}\mathbf{x}_n \quad (5.10)$$

with  $\mathbf{R}$  as the rotation tensor of the ellipsoid's main axis with respect to the bcc principal axis, and  $\mathbf{x}_n$  being the normal vector to the ellipsoid's surface in spherical coordinates and

$$\mathbf{\Gamma} = \begin{bmatrix} \gamma_1 & 0.0 & 0.0 \\ & \gamma_2 & 0.0 \\ sym. & & \gamma_3 \end{bmatrix}$$

This assumes a continuous gradient of the interface energy over the surface. In reality there may be small fluctuations, though.

The FE model uses the calculated anisotropic moduli from first principles as input in order to compute the relative strain energies. The inhomogeneity is embedded within a cube of significantly larger size (cube side length=100, inhomogeneity length of about 5 (depending on the aspect ratio) and a mesh with quadratic, tetrahedral C3D10 elements. The mesh size is 10 on the the cube's surface and refined up to 0.1 near the inhomogeneity, after a convergence analysis.

Two different models are used: *model 1* with fix aspect ratio and different orientations and *model 2* with variable aspect ratio and fixed orientation of the inhomogeneity's principal axis.

With model 1 the mechanical strain energy contribution with respect to different aspect ratios was determined for aspect ratios ranging from 0.1 to

---

<sup>2</sup>Other authors [25] also used minimization to find an energetically favored shape and orientation. Here we explain additionally why minimization may be used.

20 at angles of  $\phi = 90^\circ$  and  $\theta = 0^\circ$ . The rotation angles are defined as shown in Fig. 5.2. The angle  $\theta$  is the angle between  $[00\bar{1}]_{bcc}$  direction and  $\varphi$  between the  $(100)_{bcc}$  plane and the long axis. Here the effect of aspect ratio and shape on energy minimization is investigated.

In model 2 the aspect ratio is fixed at 5 and the ellipsoid is rotated by  $\phi$  and  $\theta$ . The crystallographic Pitsch-Schrader orientation relationship remains fixed. With model 2 the effect of orientation on energy minimization is studied.

In both cases the expansion  $\varepsilon^{vol}$  is applied to the inhomogeneity.

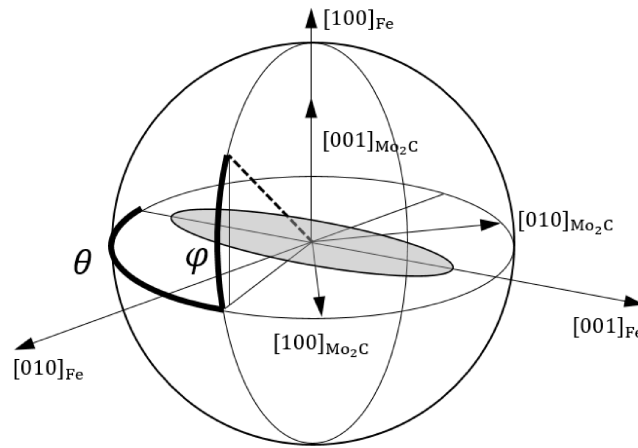


**Figure 5.2:** Angles  $\varphi$  and  $\theta$  for the orientation of the precipitate's long axis.

The Pitsch-Schrader orientation relationship as shown in Fig. 5.1 and Fig. 5.2 is preserved. The orientation of the long axis is varied to evaluate the effect of elastic anisotropy on the strain energy. To make the results quantitatively comparable at the formation temperature and in comparison with the interface energy, the elastic constants are used at  $600^\circ\text{C}$ . The interface energies are, however, calculated at  $0\text{K}$ .

At the given precipitate formation temperatures high temperature creep mechanisms are active and should thus also be accounted for in the energy balance. To account for this, a set of load dependent creep rates of pure bcc iron at a typical formation temperature of  $600^\circ$  taken from [26] is used and implemented using a power-law creep model in ABAQUS [27].

## 5.4 Results

### 5.4.1 Thermo-elastic properties of bulk Fe and $\text{Mo}_2\text{C}$

In the following section we give ab-initio results for the temperature dependence of elastic constants for the bulk systems. In the first part, the



results are shown for the elastic properties of ferromagnetic bcc Fe in its  $\alpha$ -phase. The second part focuses on the thermal properties and elastic constants of orthorhombic Mo<sub>2</sub>C, i.e., the  $\zeta$ -phase. All elastic constants are obtained using the energy approach as described in Section 5.3.1. Phonons are calculated within the quasiharmonic approximation (QHA) as described in Section 5.3.1. The temperature dependent elastic properties are calculated in order to use realistic values for a quantitative elastic strain energy contribution.

## Fe

The elastic constants of bcc Fe have been extensively studied both experimentally as well as by theoretical calculations [28, 29, 30]. To give a consistent picture of the elastic properties of the system Mo<sub>2</sub>C-Fe, we compute the elastic constants of bcc Fe in its ferromagnetic state. The results for the three independent components of the elastic matrix of bcc Fe at T=0K are shown in Table 5.2. A comparison to a previous theoretical work by Caspersen et al. [28] also given in the table shows good agreement with our results. Compared to the results by de Jong et al [31], C11 shows a larger deviation and is closer to experiment. This discrepancy is to be expected due to the difference in the computed equilibrium lattice parameter.

For calculating the temperature dependent elastic constants the temperature dependence of the lattice parameter is needed. An ab initio calculation of the thermal properties of Fe is rather cumbersome. Therefore, we take the thermal lattice expansion from experiment [32]. Calculation of elastic constants at different lattice parameters allows for the prediction of the temperature dependent elastic constants in a quasi-harmonic manner. The resulting temperature dependence of elastic constants of ferromagnetic bcc Fe is shown in Fig. 5.3 in comparison to experimental data. Generally, an overestimation of elastic constants can be seen which is to be expected as a consequence of the overestimation of bonding originating from the exchange-correlation functional used in our DFT calculations. The temperature dependence of the shear elastic constant  $C'$  is shown in Fig. 5.3 (a). Here, our results show a stronger temperature dependence than experiments. Partly, this difference can be attributed to the fact that elastic constants are determined experimentally using the ultrasonic technique which results in adiabatic values whereas the calculated values should be interpreted as being isothermal. The temperature dependence of the diagonal shear component  $C_{44}$  is shown in Fig. 5.3 (b). For the  $C_{44}$  component there is no difference between the adiabatic and isothermal conditions and the temperature dependence also quantitatively follows the trend observed in the experiment. Also the temperature dependence of the bulk modulus shown in Fig. 5.3 (c) is in good agreement with the experimental data. Finally, it should be noted that we study bcc Fe in its ferromagnetic state and disregard changes

**Table 5.2:** The calculated elastic constants of bcc Fe in comparison to other theoretical [28, 31] work and experiment [33]. (lattice parameter  $a$  in Å,  $C_{ij}$  in GPa)

	this work	Ref. [28]	Ref. [31]	experimental Ref. [33]
$a$	2.832	2.838	2.848	2.87
$C_{11}$	280	271	247	243
$C_{12}$	144	145	150	138
$C_{44}$	96	101	97	121

in elastic anisotropy due to magnetic disorder which are reported to have large influence above the Curie temperature  $T_C$  [30]. For our calculation this has little influence on the resulting elastic constants because we are below Curie temperature ( $T_C = 1043K$ ).

### Mo<sub>2</sub>C

The elastic matrix of the orthorhombic  $\zeta$ -phase of Mo<sub>2</sub>C has nine independent components. A comparison of the matrix of elastic constants obtained using the procedure described in Section 5.3.1 with values from a previous theoretical work by Connétable et al. [35] is given in Table 5.3, showing excellent agreement. To obtain the thermal expansion as well as the volumetric CTE, phonons are explicitly calculated as described in Section 5.3.1. Fig. 5.6 (b) shows the volumetric CTE as a function of temperature, compared to experiments. Here it can be seen that the averaged, i.e., volumetric CTE is in good agreement with the experiment. In order to obtain the temperature dependence of elastic constants, the volume expansion is determined in the quasiharmonic approximation. The elastic constants are calculated for structures with the equilibrium volume at different temperatures as described in Section 5.3.1. The resulting temperature dependence of the nine independent components of the elastic matrix are given in Fig. 5.4 (a), (b) and (c). The temperature dependence of the macroscopic elastic moduli, bulk modulus  $B$ , Young's modulus  $E$  and shear modulus  $G$  are obtained by Voigt averaging and compared to experimental values in Fig. 5.5. It can be seen that changes of elastic moduli due to temperature changes correspond well with the experimental trend. The overestimation of the absolute value of the bulk modulus is to be expected and can be attributed to the exchange-correlation functional used, which is known to overestimate bonding.

#### 5.4.2 Mo<sub>2</sub>C-Fe Interface

The theoretical surface energies for different Fe and Mo<sub>2</sub>C surfaces are presented in 5.4. The surface energies for Fe are in good agreement with literature data, and are lower than for Mo<sub>2</sub>C. This is not surprising as Fe is softer,

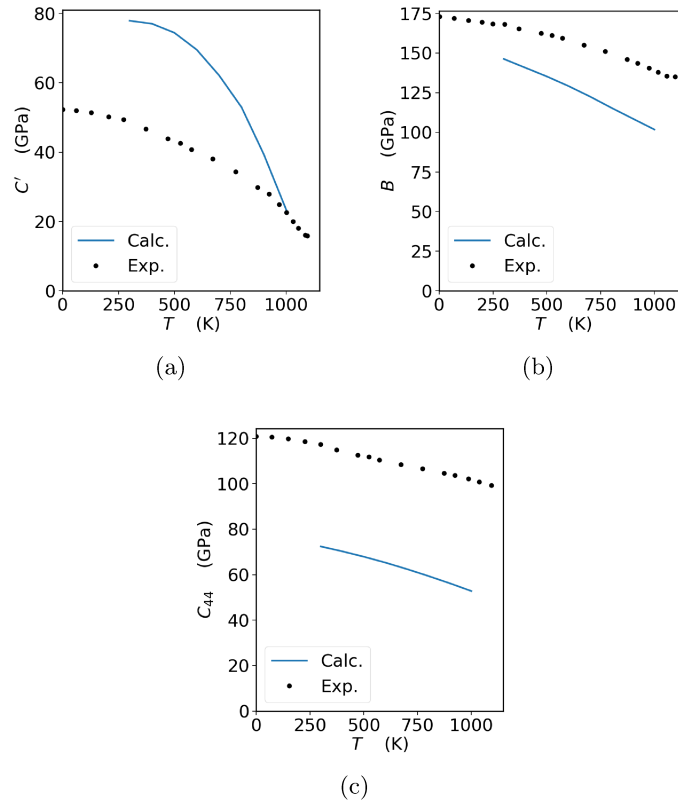


**Figure 5.3:** Temperature dependence of the elastic moduli  $C'$ ,  $B$  and  $C_{44}$  of bcc Fe. Panel (a) shows the normal components, panel (b) shows the diagonal shear components and panel (c) shows the off diagonal shear components of the elastic matrix. Solid blue lines show DFT results from this work, black circles show experimental data from Dever[34]

**Table 5.3:** The calculated elastic constants for orthorhombic Mo<sub>2</sub>C in comparison to literature data [31, 35]. (lattice parameter  $a, b, c$  in Å,  $C_{ij}$  in GPa)

	this work	Ref. [35] DFT	Ref. [31] DFT	Ref. [36] exp.
$a$	4.763	4.758	4.754	4.735
$b$	5.240	5.242	5.241	5.210
$c$	6.066	6.079	6.076	6.025
$C_{11}$	421	454	453	
$C_{22}$	489	487	489	
$C_{33}$	491	490	488	
$C_{12}$	240	224	216	
$C_{13}$	227	212	226	
$C_{23}$	137	166	169	
$C_{44}$	143	146	139	
$C_{55}$	180	184	167	
$C_{66}$	172	171	179	

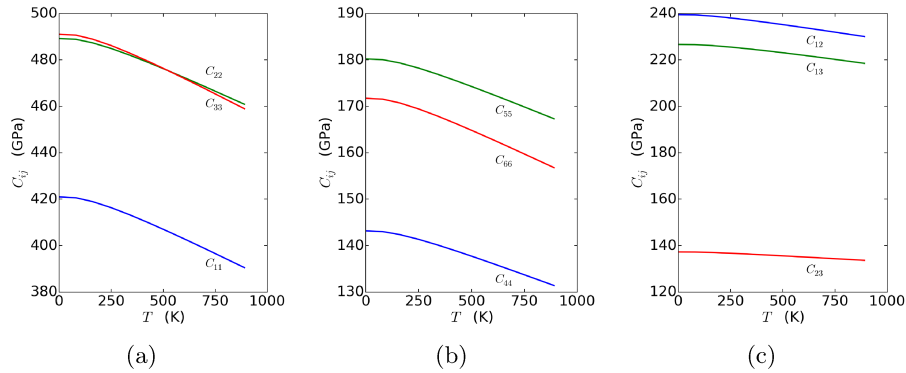


**Figure 5.4:** Temperature dependence of the components of the elastic matrix. (a) normal components  $C_{11}$ ,  $C_{22}$  and  $C_{33}$ , (b) diagonal shear components  $C_{44}$ ,  $C_{55}$ , and  $C_{66}$  and (c) off diagonal shear components  $C_{12}$ ,  $C_{13}$ , and  $C_{23}$  of the elastic matrix.

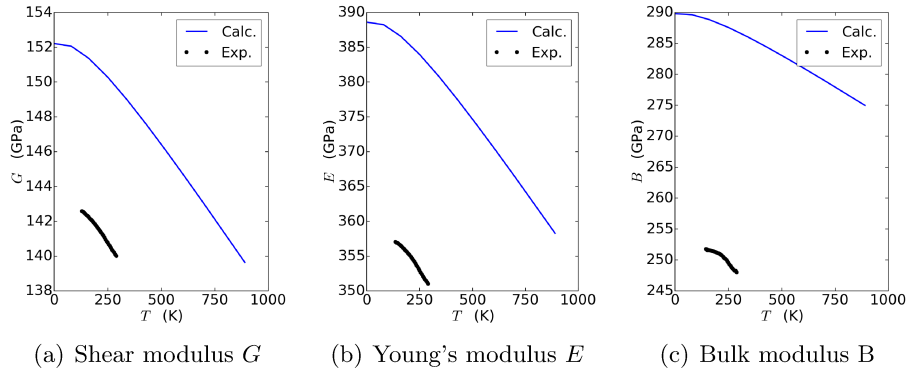


**Figure 5.5:** Polycrystalline moduli of Mo<sub>2</sub>C as a function of temperature. Blue solid lines show theoretical results from this work, black dots show experimental values from Chankurtaran et al. [37].

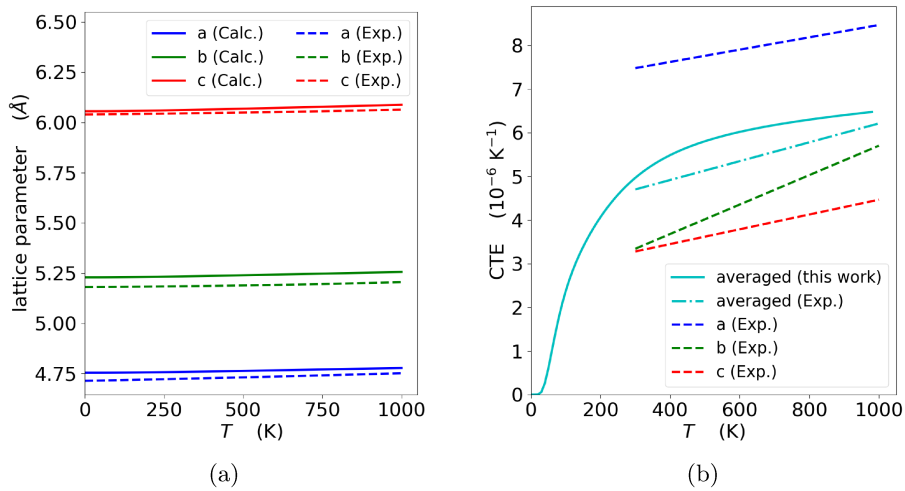


**Figure 5.6:** (a) Lattice parameters and (b) averaged CTE,  $\bar{\alpha}$ , of Mo<sub>2</sub>C as a function of temperature. Solid lines show theoretical results from this work, dashed lines show experimental values from Lönnberg et al.[4].

**Table 5.4:** Surface energies computed for Fe and Mo<sub>2</sub>C given in J/m<sup>2</sup>.

system	termination	surface	$\gamma$	literature
Fe		(100) <sub>Fe</sub>	2.50	2.55[38], 2.53[39]
Fe		(110) <sub>Fe</sub>	2.42	2.47[38], 2.46[39]
Mo <sub>2</sub> C	T1	(100)	2.95	
Mo <sub>2</sub> C	T2	(100)	3.27	
Mo <sub>2</sub> C	T1	(010)	3.18	
Mo <sub>2</sub> C	T2	(010)	2.98	
Mo <sub>2</sub> C	T1	(001)	3.18	
Mo <sub>2</sub> C	T2	(001)	3.12	
Mo <sub>2</sub> C	T3	(001)	3.27	

which means that it has weaker bonds and therefore, it is easier to break bonds and to create a surface. Comparing the surface energies for different Mo<sub>2</sub>C terminations, we observe a slight preference to terminate surfaces with Mo rather than C, yet in general, the investigated surfaces only show a comparably weak anisotropy.

For terminating the Mo<sub>2</sub>C slab at the interface with Fe we have the same possibilities as for the free surfaces, as mentioned in section 5.3.1. This means two different terminations for interface 1 and 2 and three different terminations for interface 3 between Mo<sub>2</sub>C and Fe. When joining two slabs, different translations of the slabs with respect to each other are possible. The sum of these translation states make up the  $\gamma$ -surface of the interface [38, 7]. The lowest energy on this  $\gamma$ -surface corresponds to the energetically most favorable interface. For every interface termination the  $\gamma$ -surface is computed to identify the ground state structure. To save computational effort, only the symmetrically unique part of the  $\gamma$ -surface was computed. We also used slightly smaller slabs normal to the interface plane than given in Table 5.1. However, as we are only interested in relative changes of the interface energy for the  $\gamma$ -surface, this should not affect the results. The  $\gamma$ -surfaces are shown in Fig. 5.7. The plots show that there is a small variation in the interface energy (below 0.25 J/m<sup>2</sup>) for both terminations of interface 1, for interface 2 with termination *T2*, and interface 3 with termination *T2*. This variation is more pronounced for interface 2 with termination *T1* and interface 3 with termination *T3*. However, for termination *T1* for interface 3 the variation is exceptionally large.

The minimum of the  $\gamma$ -surface corresponds to the ground state of the interface for a chosen termination. In Fig. 5.15 the ground state structures are shown. Visible effects of the relaxations are only observable for the atom layers closest to the interface. For interface 3 with termination *T1*, major reconstruction of the Fe atoms at the interface takes place: Fe atoms in the interface complete the Mo hexagons of the Mo<sub>2</sub>C slab and the remaining Fe

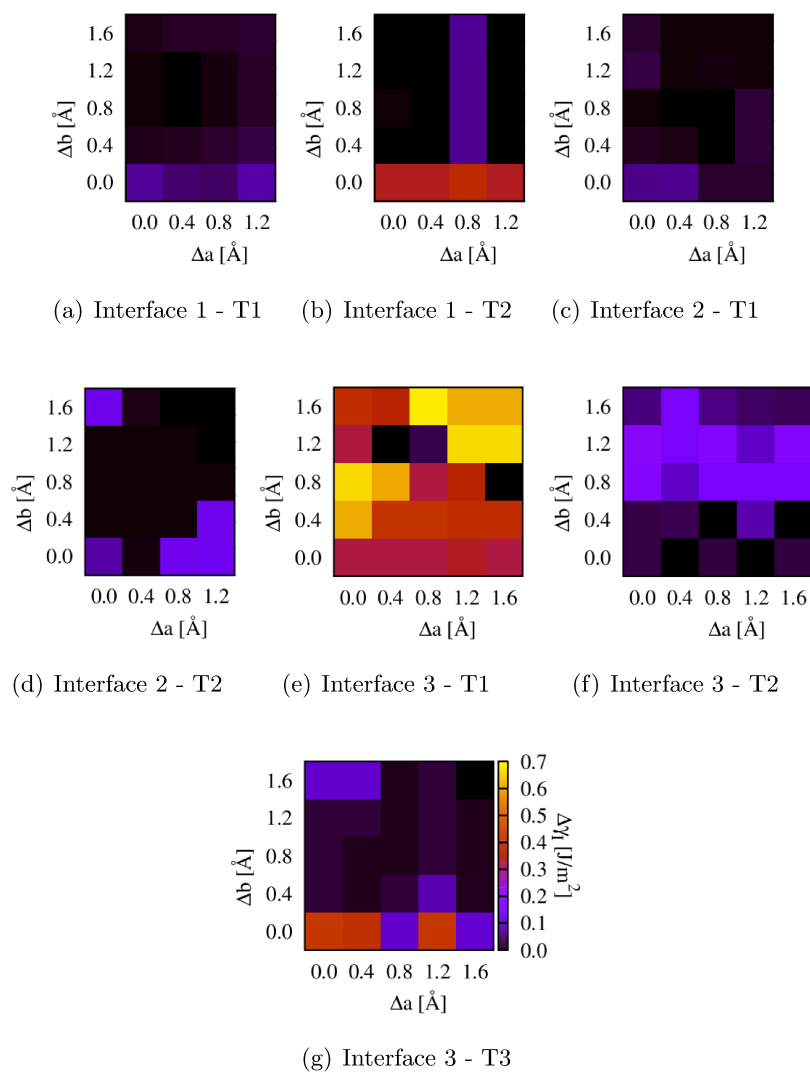


**Figure 5.7:** The  $\gamma$ -surfaces for the different terminations of the selected interfaces.

**Table 5.5:** The dimensions of the original Fe and Mo<sub>2</sub>C slabs as given in Table 5.1 as well as the interface dimensions obtained from the stress balancing method [22] in Å with the corresponding strains.

	Interface 1		Interface 2		Interface 3	
	$l_1^1$	$l_2^1$	$l_1^2$	$l_2^2$	$l_1^3$	$l_2^3$
Mo <sub>2</sub> C	5.22	12.12	5.22	4.74	4.74	12.12
Fe	5.66	12.01	5.66	4.00	4.00	12.01
Interface	5.37	12.15	5.40	4.36	4.37	12.23
$\epsilon$ Mo <sub>2</sub> C [%]	2.79	0.25	3.33	-8.72	8.57	0.91
$\epsilon$ Fe [%]	-5.40	1.15	-4.81	8.26	-8.36	1.83

atoms reorder. Also for terminations T2 and T3 the relaxations of the Fe atoms at interface appear to be of larger magnitude.

The interface energies for these interfaces are computed using Eq. 5.5 and are given in Table 5.6. The interface energies are lowest for interface 1 and highest for interface 3 ranging from 0.99 to 1.54 J/m<sup>2</sup>. In general, we observe a linear correlation of the constituting unstrained surface energies with the interface energy where high surface energies lead to high interface energies. The interface energy of an incoherent interface ( $\gamma_I^{incoh}$ ) is approximated by the mean over the  $\gamma$ -surface, as in an incoherent interface every translation of the  $\gamma$ -surface will appear [7]. For interface 1 and 2 the gamma-surface is relatively small and therefore the contribution from translations to the incoherent interface energy is rather small ( $\approx$  0.1 J/m<sup>2</sup>). The situation is different for interface 3, where this contribution is generally much more pronounced: It is of the same size as the interface energy for all terminations, and reaches 1.58 J/m<sup>2</sup> for T1.

The work of separation for separating the strained interface to strained surfaces ( $W_{sep}^s$ ) ranges from 2.75 J/m<sup>2</sup> for interface 3 with termination T3 to 4.16 J/m<sup>2</sup> for interface 1 with termination T1. If we assume that upon separation, the Fe and Mo<sub>2</sub>C slab will relax from the strained state back to equilibrium ( $W_{sep}$ ), the variation is much lower with values ranging from 4.19 to 4.44 J/m<sup>2</sup>.

By optimizing the shape of a precipitate at constant volume with the objective to minimize the total interface energy with the matrix, the equilibrium shape of the precipitate is obtained [40]. For this minimization the *pymatgen* python library [41] is employed. Based on the minimal interface energies (bold values for  $\gamma_I$  in Table 5.6) the equilibrium shape of the precipitates is predicted to be more or less cubic, which does not reflect the experimentally observed needle like shape. However, if we take into consideration the incoherent interface energy and in addition that for a 'rounded' precipitate, all terminations will appear on the interface. Then we obtain an averaged interface energy of 1.17 J/m<sup>2</sup> for interface 1, 1.34 J/m<sup>2</sup> for inter-



**Table 5.6:** The interface energies for coherent ( $\gamma_I$ ) and incoherent interfaces ( $\gamma_I^{incoh}$ ) for the interfaces shown in Fig. 5.15 with the corresponding strained surface energies and the work of separation obtained from strained and unstrained surface energies,  $W_{sep}^s$  and  $W_{sep}$ , respectively. For every interface the lowest interface energy is given in bold numbers and the values are in J/m<sup>2</sup>.

	$\gamma_I$	$\gamma_I^{incoh}$	$\gamma_{Fe}^s$	$\gamma_{Mo_2C}^s$	$W_{sep}^s$	$\gamma_{Fe}$	$\gamma_{Mo_2C}$	$W_{sep}$
Interface 1 - T1	<b>0.99</b>	1.01	2.24	2.90	4.16	2.42	2.95	4.38
Interface 1 - T2	1.25	1.33	2.24	3.04	4.03	2.42	3.27	4.44
Interface 2 - T1	1.41	1.43	2.27	2.74	3.60	2.42	3.18	4.19
Interface 2 - T2	<b>1.21</b>	1.24	2.27	2.59	3.64	2.42	2.98	4.19
Interface 3 - T1	1.35	2.93	1.81	2.51	2.97	2.50	3.18	4.33
Interface 3 - T2	<b>1.33</b>	1.42	1.81	2.38	2.85	2.50	3.12	4.29
Interface 3 - T3	1.54	1.62	1.81	2.48	2.75	2.50	3.27	4.23

face 2 and 1.99 J/m<sup>2</sup> for interface 3. This leads to a cuboid with two short edges and one longer edge with an anisotropy of 1.6. Which is much smaller than the experimental anisotropy value of about 5 this is a much smaller value. This deviation already indicates that the interface energy alone is not enough to explain the needle shape, as further discussed below.

In order to determine the impact of the Mo<sub>2</sub>C-Fe interface on the elastic properties of the composite we also compute the elastic tensor of the interface region using DFT for interface 2. To decrease computational effort, the cell size is decreased in z direction from [030] for Mo<sub>2</sub>C to [020] and for Fe from [0 $\bar{5}$ 5] to [0 $\bar{3}$ 3] such that the cell contains 48 atoms instead of 76 atoms in a setup without vacuum. As for Mo<sub>2</sub>C, we have nine independent elastic constants corresponding to nine independent deformations. Using *ThermElpy*, the structures with displacements are set up, the energy is evaluated using VASP and the analysis is again performed using total *ThermElpy*. The elastic tensor for the interface is given in Table 5.7. The elastic constants of the composite are between the corresponding bulk values of Fe and Mo<sub>2</sub>C with the exception of the  $C_{23}$  which is larger than for the bulk components. It corresponds to a shear along [001] Mo<sub>2</sub>C and [100] Fe direction, which for the interface is stiffer due to strong bonding across the interface.

A much simpler way to obtain elastic constants of an interface is given by the Grimsditch-Nizzoli approach [42, 43] based on linear elasticity, which was originally formulated for superlattices but has already been applied also for interface surroundings [44]. In Table 5.7, the  $C_{ij}$  for all interfaces from Grimsditch-Nizzoli are given. The comparison for interface 2 between the GN values and the DFT values shows that GN gives already a very good approximation, see also Fig. 5.8 for a graphical representation of the

**Table 5.7:** The elastic constants for interface 2 evaluated using DFT (I2 - DFT) as well as the elastic constants for all interfaces computed with the Grimsditch-Nizzoli approach [42, 43].

	I2 - DFT	I2 - GN	I1 - GN	I3 - GN
$C_{11}$	384	384	378	359
$C_{12}$	169	192	133	172
$C_{13}$	146	159	163	141
$C_{22}$	368	357	391	399
$C_{23}$	172	141	185	179
$C_{33}$	376	379	356	356
$C_{44}$	107	99	99	115
$C_{55}$	119	115	123	123
$C_{66}$	131	134	120	124

correlation. The largest deviation is again found for  $C_{23}$ . The fact that the deviations from the Grimsditch-Nizzoli elastic constants are generally small indicates that the contribution from the interface to elasticity is rather small.

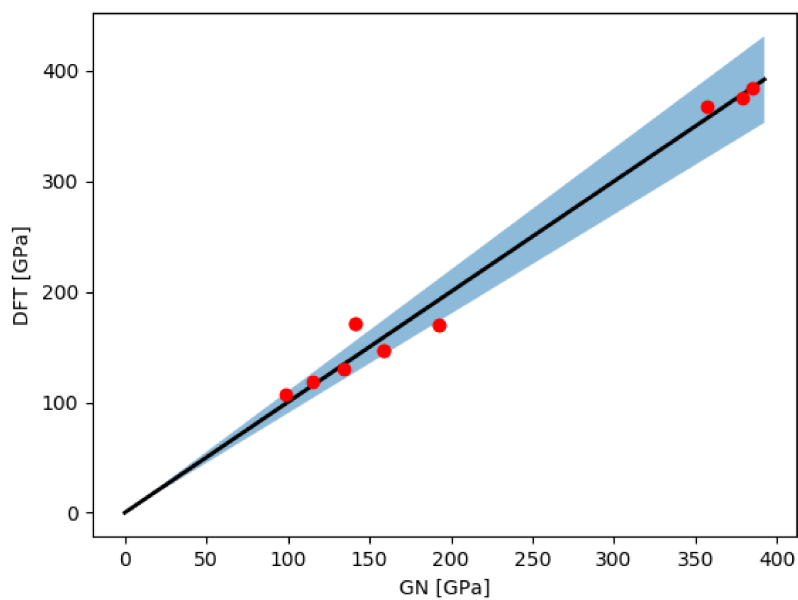
### 5.4.3 Balance of interface and strain energy

Fig. 5.9 shows the integrated incoherent interface energy with respect to precipitate orientation. For an out-of-(100)<sub>bcc</sub>-plane rotation, see Fig. 5.2,  $\varphi=90^\circ$  the interface energy is at a constant minimum. This orientation corresponds to the experimentally observed Pitsch-Schrader orientation, when compared with Fig. 5.1. The minimum interface energy is 1.3 J/m<sup>2</sup> for this orientation.

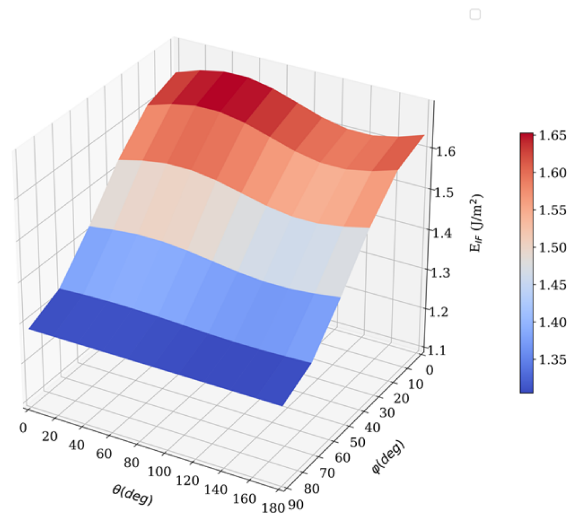
When comparing the coherent and incoherent energy contribution integrated over the inclusion surface with varying aspect ratio, see Fig. 5.10, the aspect ratio of minimum interface energy changes from 1.2 to 1.6. This is smaller than the experimentally observed values, but confirms the general trend that the interface anisotropy favors an elongated precipitate shape.

Fig. 5.11 shows the total energy contribution, as the sum of elastic and creep dissipated energy, for different orientations of a prolate inhomogeneity of aspect ratio 5. The energy surface as a function of  $\varphi$  and  $\theta$  also yields a minimum at  $\varphi=90^\circ$ . This means that both interface and total strain energy yield a minimum for the experimentally observed Pitsch-Schrader orientation. With increasing aspect ratio the effect of varying total energy with orientation becomes more pronounced, while it flattens when the aspect ratio approaches 1.0 and the strain energy becomes independent of orientation.

Comparing the absolute values for interface energy and mechanical strain energy for an inclusion of 5500 nm<sup>3</sup> (which corresponds to a length of 80 nm and an aspect ratio of 7) we find the total energy dominated by the interface energy.



**Figure 5.8:** Elastic constants for interface 1 from DFT plotted against values obtained from the method described by Grimsditch and Nizzoli (GN) [42, 43] with 10% deviation marked.



**Figure 5.9:** Incoherent interface energy for the precipitate’s long axis rotated in different orientations (aspect ratio of 5).

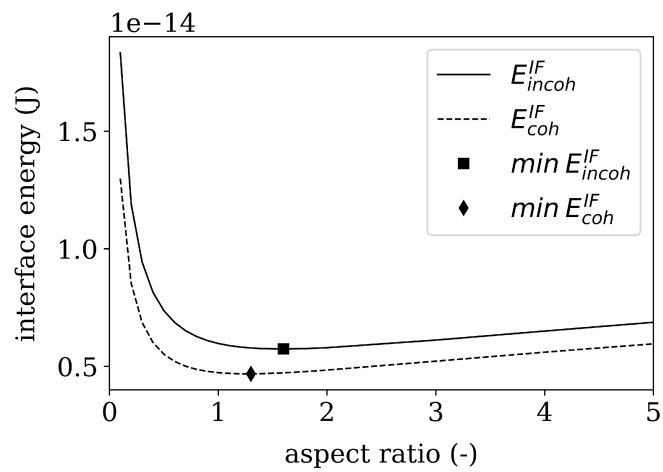


**Figure 5.10:** Absolute interface energy for coherent and incoherent interface with Pitsch-Schrader orientation.

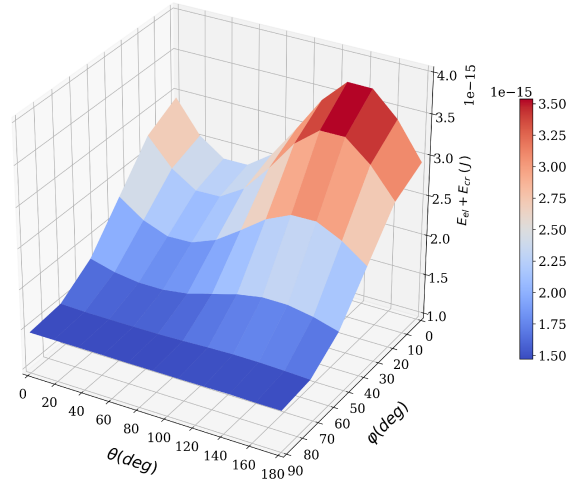


**Figure 5.11:** Strain energy  $E_{mech} = E_{el} + E_{cr}$  for different orientations due to lattice expansion for an aspect ratio of 5.

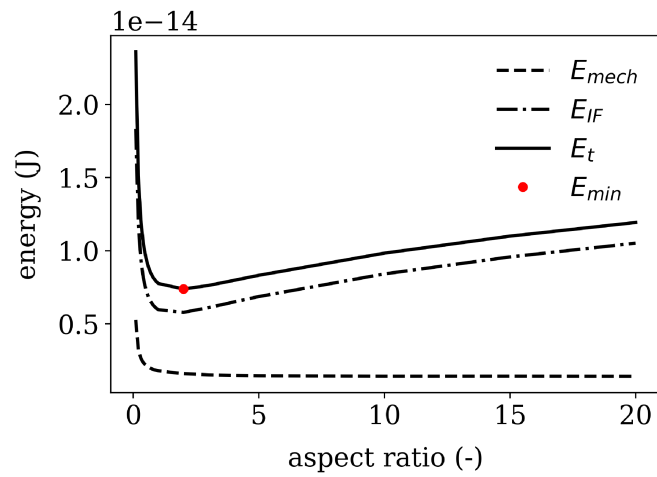


**Figure 5.12:** Absolute strain energy plus creep dissipation ( $E_{mech}=E_{el} + E_{cr}$ ) compared with incoherent interface energy  $E_{IF}$  as a function of aspect ratio for  $\varphi = 90^\circ$ .

The strain energy contribution, including creep and elastic strain energy, is one order of magnitude lower than the interface energy Fig. 5.12. Thus the expected aspect ratio is close to the incoherent, purely interface-dominated case. When a purely elastic mechanical contribution is considered, the mechanical energy is two orders of magnitude higher than the interface energy and would thus dominate the energy balance. This case is, however, considered unrealistic at the considered precipitate formation temperature of 600°.

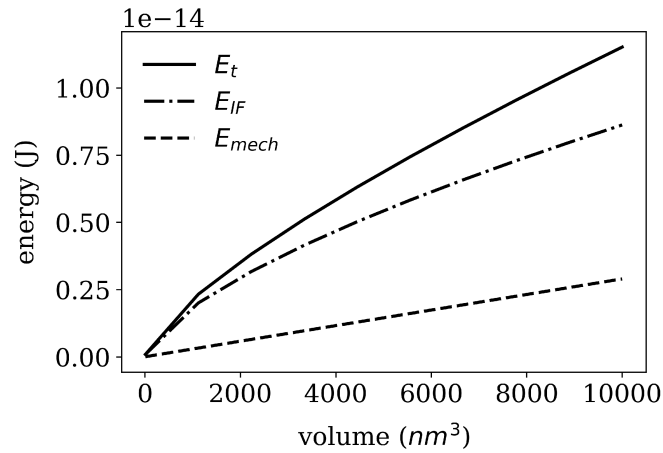


**Figure 5.13:** Comparison of total energy  $E_t$ , as the sum of interface energy  $E_{IF}$  and strain energy  $E_{mech}$  for different precipitate volumes.

## 5.5 Conclusions

The quantitative comparison of anisotropic interface energies from first principles in combination with strain energy allows a more detailed energy based interpretation of  $Mo_2C$  precipitate orientation and shape.

Minimizing the coherent and incoherent interface energies of a precipitate with constant volume and ellipsoidal shape yields an aspect ratio of 1.2 and 1.6 respectively. The interface 3 at the needle tip is the most susceptible to become incoherent. This was found by calculating the interface energies for coherent and incoherent states with different terminations. If the difference between the interface energy at the needles' tip and the two interfaces on its' long axis becomes more pronounced, the favored shape shifts to higher aspect ratios. For an aspect ratio of 10 to be optimal, the interface energy at the tip must be around 3 times larger than the interface energy along the long side.

The aspect ratio is dominated by the interface contribution and slightly affected by the strain energy contribution. In a quantitative comparison

at 600°C we show that the interface energy dominates when creep is taken into account and is one order of magnitude higher than the strain energy contribution. The opposite is true, when creep is neglected. Then the mechanical contribution would dominate.

Both, the calculated interface energies and the strain energies yield a minimum value at the experimentally observed orientation. The elastic constants of the Mo<sub>2</sub>C and Fe composite calculated by means of first principles confirm the findings of the Grimsditch-Nizzoli approach, which is based on linear rule of mixture.

## 5.6 Appendix

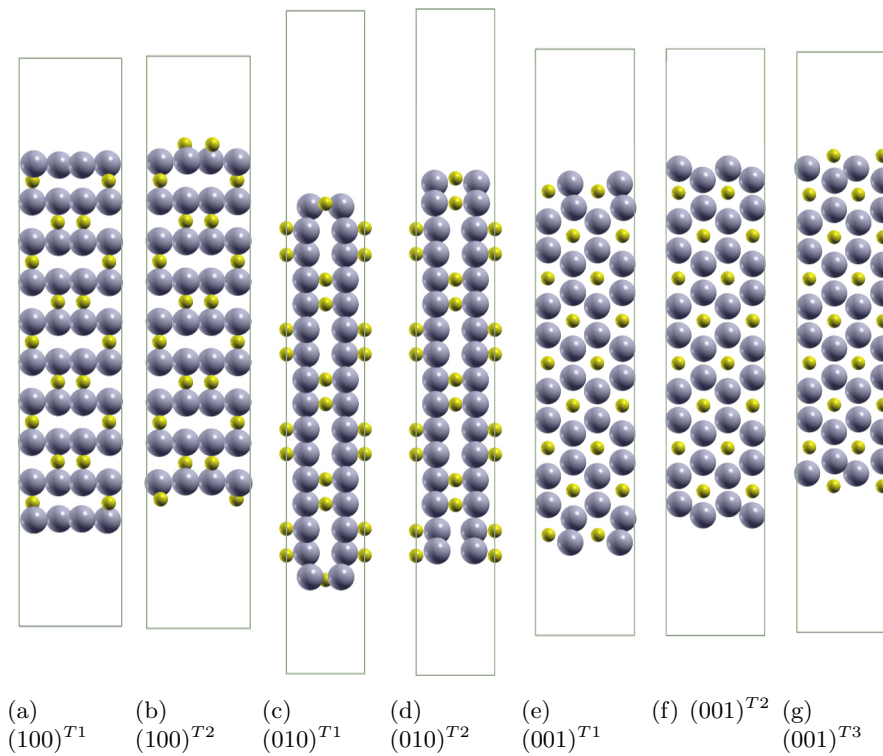


**Figure 5.14:** Structures for various terminations of Mo<sub>2</sub>C surfaces where the green line denotes the simulation cell. yellow: carbon, grey: Mo

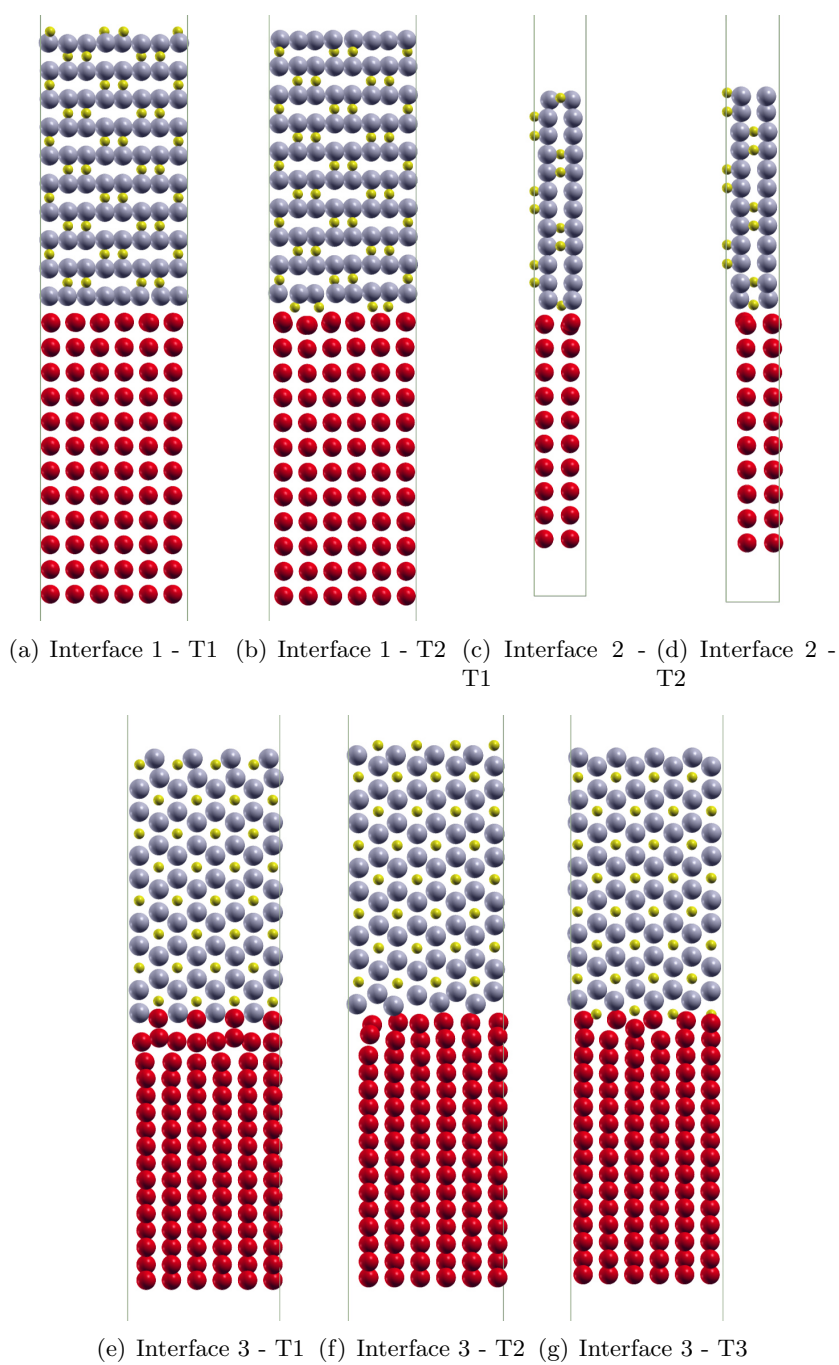


**Figure 5.15:** The ground state structures for the different terminations of the chosen interfaces. yellow: carbon, grey: Mo, red: Fe



# Bibliography

- [1] D. J. Dyson, S. R. Keown, D. Raynor, and J. A. Whiteman. The orientation relationship and growth direction of Mo<sub>2</sub>C in ferrite. *Acta Metallurgica*, 14(7):867–875, 1966. ISSN 00016160. doi: 10.1016/0001-6160(66)90007-1.
- [2] A. J. Allen, D. Gavillet, and J. R. Weertman. SANS and TEM studies of isothermal M<sub>2</sub>C carbide precipitation in ultrahigh strength AF1410 steels. *Acta Metallurgica Et Materialia*, 41(6):1869–1884, 1993. ISSN 09567151. doi: 10.1016/0956-7151(93)90207-9.
- [3] S. Yamasaki and H. K. D. H. Bhadeshia. Modelling and characterisation of Mo<sub>2</sub>C precipitation and cementite dissolution during tempering of Fe–C–Mo martensitic steel. *Materials Science and Technology*, 19(6):723–731, 2013. ISSN 0267-0836. doi: 10.1179/026708303225002929.
- [4] B. Lönnberg. Thermal expansion studies on the subcarbides of group V and VI transition metals. *Journal of The Less-Common Metals*, 120(1):135–146, 1986. ISSN 00225088. doi: 10.1016/0022-5088(86)90635-1. URL <http://www.sciencedirect.com/science/article/pii/0022508886906351>.
- [5] Y. N. Shi and P. M. Kelly. The crystallography and morphology of Mo<sub>2</sub>C in ferrite. *Journal of Materials Science*, 37(10):2077–2085, 2002. ISSN 00222461. doi: 10.1023/A:1015289702308.
- [6] R. Janisch and C. Elsässer. Growth and mechanical properties of a MoC precipitate at a Mo grain boundary: An ab initio density functional theory study. *Physical Review B - Condensed Matter and Materials Physics*, 77(9):094118, 2008. ISSN 10980121. doi: 10.1103/PhysRevB.77.094118.
- [7] D. H. R. Fors and G. Wahnström. Theoretical study of interface structure and energetics in semicoherent Fe(001)/MX(001) systems (M=Sc, Ti, V, Cr, Zr, Nb, Hf, Ta; X=C or N). *Physical Review B - Condensed Matter and Materials Physics*, 82(19), 2010. ISSN 10980121. doi: 10.1103/PhysRevB.82.195410.

- [8] D. H.R. Fors, S. A.E. Johansson, M. V.G. Petisme, and G. Wahnström. Theoretical investigation of moderate misfit and interface energetics in the Fe/VN system. *Computational Materials Science*, 50(2):550–559, dec 2010. ISSN 09270256. doi: 10.1016/j.commatsci.2010.09.018. URL <https://www.sciencedirect.com/science/article/pii/S0927025610005227>.
- [9] H. Sawada, S. Taniguchi, K. Kawakami, and T. Ozaki. First-principles study of interface structure and energy of Fe/NbC. *Modelling and Simulation in Materials Science and Engineering*, 21(4):045012, jun 2013. ISSN 09650393. doi: 10.1088/0965-0393/21/4/045012. URL <http://stacks.iop.org/0965-0393/21/i=4/a=045012?key=crossref.7d05c218b2097c3782ab39b4ef47ccc0>.
- [10] D. Di Stefano, R. Nazarov, T. Hickel, J. Neugebauer, M. Mrovec, and C. Elsässer. First-principles investigation of hydrogen interaction with TiC precipitates in  $\alpha$ -Fe. *Physical Review B*, 93(18):1–14, 2016. ISSN 24699969. doi: 10.1103/PhysRevB.93.184108.
- [11] M. G. Hall, K. R. Kinsman, and H. I. Aaronson. Mechanism of formation of mo<sub>2</sub>c needles in an fe-c-mo alloy. *Metallurgical Transactions*, 3(5):1320–1322, May 1972. ISSN 1543-1916. doi: 10.1007/BF02642472. URL <https://doi.org/10.1007/BF02642472>.
- [12] G. Kresse and J. Hafner. *Ab initio* molecular dynamics for liquid metals, 1993. ISSN 0163-1829. URL <https://link.aps.org/doi/10.1103/PhysRevB.47.558>.
- [13] G. Kresse and J. Furthmüller. Efficiency of ab-initio total energy calculations for metals and semiconductors using a plane-wave basis set. *Computational Materials Science*, 6(1):15–50, 1996. ISSN 09270256. doi: 10.1016/0927-0256(96)00008-0.
- [14] G. Kresse and J. Furthmüller. Efficient iterative schemes for ab initio total-energy calculations using a plane-wave basis set. *Physical Review B - Condensed Matter and Materials Physics*, 54(16):11169–11186, 1996. ISSN 1550235X. doi: 10.1103/PhysRevB.54.11169. URL <http://link.aps.org/doi/10.1103/PhysRevB.54.11169>.
- [15] G. Kresse and D. Joubert. From ultrasoft pseudopotentials to the projector augmented-wave method. *Physical Review B*, 59(3):1758–1775, jan 1999. ISSN 0163-1829. doi: 10.1103/PhysRevB.59.1758. URL <https://link.aps.org/doi/10.1103/PhysRevB.59.1758>.
- [16] J. P. Perdew, K. Burke, and M. Ernzerhof. Generalized gradient approximation made simple. *Physical Review Letters*, 77(18):3865–3868, 1996. ISSN 10797114. doi:

- 10.1103/PhysRevLett.77.3865. URL <http://www.ncbi.nlm.nih.gov/pubmed/10062328>{%}5Cn<http://link.aps.org/doi/10.1103/PhysRevLett.77.3865>{%}5Cn<http://link.aps.org/abstract/PRL/v77/p3865>{%}5Cn<http://link.aps.org/doi/10.1103/PhysRevLett.77.3865>.
- [17] J. P. Perdew, M. Ernzerhof, and K. Burke. [ERRATA] Generalized Gradient Approximation Made Simple. *Physical review letters*, 78(18): 3865–3868, 1997. ISSN 1079-7114. doi: 10.1103/PhysRevLett.77.3865. URL <http://www.ncbi.nlm.nih.gov/pubmed/22502509>.
- [18] A. Togo and I. Tanaka. First principles phonon calculations in materials science. *Scripta Materialia*, 108:1–5, 2015. ISSN 13596462. doi: 10.1016/j.scriptamat.2015.07.021. URL <http://dx.doi.org/10.1016/j.scriptamat.2015.07.021>.
- [19] Thomas Dengg. *Computation of Temperature Dependent Elastic Constants Within the Framework of Density-Functional Theory*. PhD thesis, Institute of physics, Karl-Franzens-University Graz, 2017.
- [20] R. Golezorkhtabar, P. Pavone, J. Spitaler, P. Puschnig, and C. Draxl. ElaStic: A tool for calculating second-order elastic constants from first principles. *Computer Physics Communications*, 184(8):1861–1873, aug 2013. ISSN 00104655. doi: 10.1016/j.cpc.2013.03.010. URL <https://linkinghub.elsevier.com/retrieve/pii/S0010465513001070>.
- [21] B. Fultz. Vibrational thermodynamics of materials. *Progress in Materials Science*, 55(4):247–352, may 2010. ISSN 00796425. doi: 10.1016/j.pmatsci.2009.05.002. URL <https://linkinghub.elsevier.com/retrieve/pii/S0079642509000577>.
- [22] M. N. Popov, J. Spitaler, M. Mühlbacher, C. Walter, J. Keckes, C. Mitterer, and C. Draxl. TiO 2(100)/Al 2O 3(0001) interface: A first-principles study supported by experiment. *Physical Review B - Condensed Matter and Materials Physics*, 86(20):1–13, 2012. ISSN 10980121. doi: 10.1103/PhysRevB.86.205309.
- [23] D. Scheiber, W. Eßl, J. Strutzenberger, F. Goodwin, J. Spitaler, and G. Reiss. Morphology of fe2al5 particles and the interface to wc coating in the context of hot-dip galvanizing: An ab initio study. *Journal of Alloys and Compounds*, 824:153854, 2020. ISSN 0925-8388. doi: <https://doi.org/10.1016/j.jallcom.2020.153854>. URL <http://www.sciencedirect.com/science/article/pii/S0925838820302176>.

- [24] F.D. Fischer and K. Hackl. On the relation between the principle of maximum dissipation and inelastic evolution given by dissipation potentials. *Proceedings of the Royal Society A*, 464, 2008. doi: 10.1098/rspa.2007.0086.
- [25] R. K. Sharma, A. Tewari, R.N. Singh, and B.P. Kashyap. Optimum shape and orientation of  $\delta$ -hydride precipitate in  $\alpha$ -zirconium matrix for different temperatures. *Journal of Alloys and Compounds*, 742:804 – 813, 2018. ISSN 0925-8388. doi: <https://doi.org/10.1016/j.jallcom.2017.12.085>. URL <http://www.sciencedirect.com/science/article/pii/S0925838817342688>.
- [26] H. Watanabe and M. Yamada, N.and Okaji. Linear thermal expansion coefficient of silicon from 293 to 1000 K. *International Journal of Thermophysics*, 25(1):221–236, 2004. ISSN 0195928X. doi: 10.1023/B:IJOT.0000022336.83719.43.
- [27] Dassault Systems. Abaqus standard. URL <https://www.3ds.com/products-services/simulia/products/abaqus/abaqusstandard/>.
- [28] K. J. Caspersen, A. Lew, M. Ortiz, and E. A. Carter. Importance of Shear in the bcc-to-hcp Transformation in Iron. *Physical Review Letters*, 93(11):115501, sep 2004. ISSN 0031-9007. doi: 10.1103/physrevlett.93.115501. URL <https://link.aps.org/doi/10.1103/PhysRevLett.93.115501>.
- [29] X. Sha and R. E. Cohen. First-principles thermoelasticity of bcc iron under pressure. *Physical Review B - Condensed Matter and Materials Physics*, 74(21):214111, 2006. ISSN 10980121. doi: 10.1103/PhysRevB.74.214111. URL <https://link.aps.org/doi/10.1103/PhysRevB.74.214111>.
- [30] V. I. Razumovskiy, A. V. Ruban, and P. A. Korzhavyi. Effect of temperature on the elastic anisotropy of pure Fe and Fe0.9Cr0.1 random alloy. *Physical Review Letters*, 107(20):205504, nov 2011. ISSN 00319007. doi: 10.1103/PhysRevLett.107.205504. URL <https://link.aps.org/doi/10.1103/PhysRevLett.107.205504>.
- [31] M. De Jong, W. Chen, T. Angsten, A. Jain, R. Notestine, A. Gamst, M. Sluiter, C. K. Ande, S. Van Der Zwaag, J. J. Plata, C. Toher, S. Curtarolo, G. Ceder, K. A. Persson, and M. Asta. Charting the complete elastic properties of inorganic crystalline compounds. *Scientific Data*, 2:150009, 2015. ISSN 20524463. doi: 10.1038/sdata.2015.9.

- [32] I. Seki and K. Nagata. Lattice Constant of Iron and Austenite Including Its Supersaturation Phase of Carbon. *ISIJ International*, 45(12):1789–1794, 2006. ISSN 0915-1559. doi: 10.2355/isijinternational.45.1789.
- [33] G Simmons and H Wang. *Single crystal elastic constants and calculated polycrystal properties*. MIT Press, Cambridge, 1971. ISBN 3257227892.
- [34] D.J. Dever. Temperature dependence of the elastic constants in  $\alpha$ -iron single crystals: relationship to spin order and diffusion anomalies. *Journal of Applied Physics*, 43, 1972. doi: 10.1063/1.1661710. URL <http://gen.lib.rus.ec/scimag/index.php?s=10.1063/1.1661710>.
- [35] D. Connétable. First-principles study of transition metal carbides. *Materials Research Express*, 3(12):126502, 2016. doi: 10.1088/2053-1591/3/12/126502. URL <https://doi.org/10.1088/2053-1591/3/12/126502>.
- [36] T. Epicier, J. Dubois, C. Esnouf, G. Fantozzi, and P. Convert. Neutron powder diffraction studies of transition metal hemicarbides  $M_2C_1$  II. In situ high temperature study on  $W_2C_1$  and  $Mo_2C_1$ . *Acta Metallurgica*, 36(8):1903–1921, 1988. ISSN 0001-6160. doi: [https://doi.org/10.1016/0001-6160\(88\)90293-3](https://doi.org/10.1016/0001-6160(88)90293-3). URL <http://www.sciencedirect.com/science/article/pii/0001616088902933>.
- [37] M. Cankurtaran, G. A. Saunders, and K. C. Goretti. Ultrasonic study of the temperature and pressure dependences of the elastic properties of fully oxygenated  $\{YBa\}_2Cu_3O_{6.94}$ . *Superconductor Science and Technology*, 7(1):4–9, jan 1994. doi: 10.1088/0953-2048/7/1/002. URL <https://doi.org/10.1088/0953-2048/7/1/002>.
- [38] D. Scheiber, R. Pippin, P. Puschnig, and L. Romaner. Ab initio calculations of grain boundaries in bcc metals. *Modelling and Simulation in Materials Science and Engineering*, 24(3):035013, 2016. ISSN 1361651X. doi: 10.1088/0965-0393/24/3/035013.
- [39] S. Schönecker, X. Li, B. Johansson, Se K. Kwon, and L. Vitos. Thermal surface free energy and stress of iron. *Scientific Reports*, 5:14860, 2015. ISSN 20452322. doi: 10.1038/srep14860. URL <http://www.nature.com/articles/srep14860> <http://www.nature.com/srep/2015/151006/srep14860/full/srep14860.html>.

- [40] M. Christensen, G. Wahnström, S. Lay, and C. H. Allibert. Morphology of WC grains in WC-Co alloys: Theoretical determination of grain shape. *Acta Materialia*, 55(5):1515–1521, mar 2007. ISSN 13596454. doi: 10.1016/j.actamat.2006.10.013. URL <https://www.sciencedirect.com/science/article/pii/S1359645406007373>.
- [41] S. P. Ong, W. D. Richards, A. Jain, G. Hautier, M. Kocher, S. Cholia, D. Gunter, V. L. Chevrier, K. A. Persson, and G. Ceder. Python Materials Genomics (pymatgen): A robust, open-source python library for materials analysis. *Computational Materials Science*, 68: 314–319, feb 2013. ISSN 09270256. doi: 10.1016/j.commatsci.2012.10.028. URL <http://linkinghub.elsevier.com/retrieve/pii/S0927025612006295>.
- [42] M. Grimsditch. Effective elastic constants of superlattices. *Physical Review B*, 31(10):6818–6819, 1985. ISSN 01631829. doi: 10.1103/PhysRevB.31.6818.
- [43] M. Grimsditch and F. Nizzoli. Effective elastic constants of superlattices of any symmetry. *Physical Review B*, 33(8):5891–5892, 1986. ISSN 01631829. doi: 10.1103/PhysRevB.33.5891.
- [44] M. Friák, M. Všianská, D. Holec, M. Zelený, and M. Šob. Tensorial elastic properties and stability of interface states associated with 5(210) grain boundaries in (Al,Si). *Science and Technology of Advanced Materials*, 18(1):273–282, dec 2017. ISSN 18785514. doi: 10.1080/14686996.2017.1312519. URL <https://doi.org/10.1080/14686996.2017.1312519>.